OPTICAL MICRO-ELECTRO-MECHANICAL SYSTEMS FOR ADD/DROP MULTIPLEXING AND INFRARED GAS SPECTROSCOPY

A Dissertation

Presented to the Faculty of the Graduate School

of Cornell University

in Partial Fulfillment of the Requirements for the Degree of

Doctor of Philosophy

by

John Provine

January 2005

OPTICAL MICRO-ELECTRO-MECHANICAL SYSTEMS FOR ADD/DROP MULTIPLEXING AND INFRARED GAS SPECTROSCOPY

John Provine, Ph.D.

Cornell University 2005

Wide ranging efforts in development of various Micro-Electro-Mechanical (MEM) devices over the past twenty years have created a vast collection of novel devices that can be fabricated in numerous ways. As the MEMS field matures it is important to remember the systems aspect the name implies and ensure useful and complete systems are constructed utilizing these wonderful devices. This thesis focuses on two different areas of application for optical MEM systems.

The first is a system for optical telecommunications networks that enables an optical add/drop multiplexer, also frequently called a wavelength selective switch. Wavelength selective switches anticipate the need for inexpensive optical switching components with the extension of the optical domain of telecommunications to the end user through fiber to the home. The wavelength selective switch studied is based on the hybridization of a MEMS based optical switch with a particular type of planar lightwave circuit, or on-chip waveguiding device, called an Arrayed Waveguide Grating (AWG). Three separate MEMS switches were implemented into this type of system: a lateral fiber actuator, a scanning micro-mirror, and a binary micro-mirror array. The binary micro-mirror array displayed the greatest performance and is additionally advantageous because of the possibility of further integration. This implementation of a wavelength selective switch provides excel-

lent optical networking properties and performance at low power and with a small device area compared to other switch implementations. Additionally, the system is scalable as the network increases in port count and channel density.

The second system studied is an optical gas spectrometer. A scanning MEMS mirror was used with various additional optical components to create a Non-Dispersive Infra-Red (NDIR) gas detector. The MEMS mirror is used in conjunction with a Linear Variable Filter (LVF) to scan a particular range of IR radiation. By detecting the transmission spectrum within the IR radiation band, detection of gases based on their unique radiation absorption pattern can be carried out. Detection of CO_2 in concentration ranges from 400ppm to a few percent was performed. Simultaneous detection of multiple species is possible. The system offers a potentially portable and inexpensive gas spectrometer with accuracy necessary for various commercial needs.

BIOGRAPHICAL SKETCH

J Provine was born in Oklahoma, USA, in 1976, to his loving parents John and Laurel. He grew up on the family farm with his parents, older sister, three younger brothers, and maternal grandparents. The isolation and space of the farm provided ample opportunity for young J to hoot and holler and enjoy himself as well as a very large lawn that needed frequent mowing. Additionally, his home had a well stocked library and informative parents who were willing to explain anything he or they found interesting.

As J grew older, rural country life agreed less and less with him. He left home at 16 to attend boarding school at the Oklahoma School of Science and Mathematics, from which he graduated simultaneous to completing his high school studies at Oklahoma Bible Academy.

In 1994, J enrolled at Rice University, which proved to be a beautiful and wonderful institute of higher learning and broad-minded education. In 1999, he graduated with a BA in Physics, a BS and Masters in Electrical Engineering, a well-rounded education, and a wonderful collection of friends and mentors.

After a brief summer working for Texas Instruments, J left the south for Cornell University in Ithaca, NY. Originally enrolling in the Applied and Engineering Physics program, he later migrated down the road to Electrical Engineering and joined Dr. Norman Tien's group. Professor Tien moved his group to the University of California, where J lived as he completed his research and enjoyed the lack of snow, while maintaining his valued status as a Cornell student.

Through out his travels, J has slowly built his beloved music and book collections while adding new friends and enjoying the universal availability of good movies and basketball.

To my parents, Dr. John and Laurel Provine,

Who taught all my earliest and best lessons.

ACKNOWLEDGEMENTS

I am very pleased to be able to devote this section of my thesis to those people who have aided me in so many ways to complete this work. Firstly, I thank my advisor, Professor Norman Tien, deeply for the chance to explore and work in his research group. Professor Tien allows his students great creative freedom to learn and research on their own, which strengthens their understanding and abilities in the end through the various day to day struggles that inevitably arise. Additionally, he is an eternally happy and optimistic man with whom it is always a joy to speak. Secondly, I would like to thank Professor David Horsley of the University of California at Davis, who worked with me on the IR gas sensing aspect of this thesis and provided wonderful company and insight into research. Professor Horsley treated me like a colleague and was very free with his time and wisdom throughout the time we worked together.

I would also like to thank Professors Alex Gaeta and Sheila Hemami for serving on my committee from day one. They met the obvious added difficulties of serving on a committee of a student who lived a continent away for a good portion of his time at Cornell, without complaint and were helpful and positive in all of my contact with them.

I greatly enjoy the collaborative aspect of scientific research and have been fortunate to be in the company of some wonderful scientists at Cornell University, the Cornell Nanofabrication Facility and the Berkeley Sensor Actuator Center. Specifically, I would add special thanks to Jacob Sun of ANDevices for his collaborative spirit and generosity on the AWG portion of this thesis. Additionally, I would like to thank my group-mates for their help and companionship throughout my studies. Specifically, Dr. Daniel McCormick provided information and spare devices from

his fiber actuator project utilized in this thesis.

Properly full acknowledgement of the debt I owe my loving parents, John and Laurel, and the rest of my family can never be contained in words.

I would like to acknowledge the wonderful group of friends who always kept me happy and listened to my breathlessly excited tales of lab work and my breathlessly disappointed listing of set-backs with equal patience and empathy. The list of these friends is quite long, but I wish to specifically thank: Carisa Yee, Clay Scott, the roommates (Jeremiah Helm, Rory Mays, and Sandeep Ghael), Alfonso Acosta, Emeka, Craig and Margaret Votava, Kevin Dezfulian and Lidija Sekaric, Andinet Asmamaw, Jane Kim, Lian Chang, and the Party In A Box.

And all ultimate acknowledgement could never be expressed more clearly by me than it was by the apostle Paul: *I can do all things through Christ who strengthens me.* (Phillippians 4:13)

TABLE OF CONTENTS

LIST OF FIGURES

LIST OF TABLES

CHAPTER 1

INTRODUCTION

1.1 MEMS & Optical MEMS

Since being initially brought to wide attention by Richard Feynman's famous talk to the American Physical Society [1] in 1959, the possibilities of microscopic machines and information has grown well beyond what he could imagine at the time. Of course, that was just as Feynman predicted. Twenty years later, another seminal paper was published: Kurt Peterson's evaluation of the mechanical properties of silicon [2]. Since then thousands of papers reporting [3], studying [4], proselytizing [5], and even vilifying [6] [7] Micro-Electro-Mechanical Systems (MEMS) have been published.

MEMS devices are microscopic moving machines that are fabricated in much the same way and on much the same scale as integrated circuits. MEMS have been developed utilizing various III-V semiconductor compounds and polymers, although Si is still the primary material [8]. MEMS applications include data storage, micro-fluid management, radio frequency communication, accelerometers, microscopy, and many others too numerous to mention [3].

This thesis is concerned with MEMS for managing and manipulating light flow. The structural dimensions and controllable displacements of MEMS is on the same order as the wavelength of visible and infrared light. Additionally, the microfabrication techniques used can leave structures with very smooth surfaces so that reflection and diffraction of light is possible. An very fine review of many of the methods, applications, and problems of optical MEMS is found in a review by Walker and Nagel [9].

1.2 Optical Telecommunications Networks

In the last decade, the explosion of the internet drew many scientists and companies to work in the telecommunication field. Optical telecommunication networks became commercially available in 1980, and their capacity has been continuously increased until it is orders of magnitude above the original values [10]. The capacity and speed of optical networks was one of the primary forces behind the explosion of world wide internet connectivity and usage in the 1990s.

While the data rate of optical fibers has grown steadily over the past decade to meet and anticipate the needs of the online community, the switching capacity and signal traffic management has not kept pace. In 1996 a commercially available single fiber could transmit 20 Gb/s and in 2004 that figure is up to 5100 Gb/s [11]. There is an inherent scalability limit to improving switching speeds with electronic switches known as the backplane problem [12]. The primary solution is to look for ways to manage switching in the network optically, without conversion to electrical signals as much as possible.

Very soon terabit switching capacities will be required [13] in metro area networks, and current state of the art electronic switching consoles can handle at most a terabit, which means the capacity of a single fiber will fill a full console. Additionally, fiber to the home projects are gaining momentum in the US and are already entrenched in Japan, creating a demand for mass produced, cheap optical signal handling systems [14]. Because of the high volume demand, integrated planar optics will become more cost effective and attractive in future implementations.

Optical MEMS offers a great opportunity of light management to the telecommunication network. Even though the data in optical networks is transmitted by means of light signals, the management of the signals in the network is primarily

handled by electronic means. This interface between optical and electrical systems poses one of the possible future roadblocks for larger capacity and increased speed of telecommunication networks. This thesis presents a hybrid MEMS optical switch and lightwave circuit to provide a form of optical network management needed for advancement of optical telecommunication networks.

1.3 Gas Spectroscopy

When the "telecom bubble" burst around the turn of the century, a great deal of optical MEMS research that was focused toward and funded by telecommunications became solutions in search of a problem. The expertise and knowledge gained by the optical MEMS community shifted into a variety of new application fields. Environmental sensing was one of the fields that drew many researchers because of pressing interest in element detection for energy, biology, and defense concerns.

Inexpensive micro-detectors of certain gas species are desired for *in vivo* monitoring during surgery, atmospheric monitoring for energy management and contamination sensing, and safety monitoring. The second segment of this thesis presents an optical MEMS device to detect the presence and determine the concentration of various gas molecules.

More specifically, the desired system is portable and capable of detecting multiple gas species either individually or simultaneously. This system provides low cost, portable detection at commercially interesting concentration levels in many industrial settings. It is not intended to replace gas chromatographs or Fourier Transform Infrared (FTIR) spectroscopy units for high precision spectrographic measurements.

1.4 Dissertation Outline

The arrangement of the remainder of the thesis is described below.

Chapters 2 and 3 are concerned with the optical telecommunications project. Chapter 2 provides a detailed introduction to the lightwave device known as the Arrayed Waveguide Grating (AWG) and outlines how it can be combined with a MEMS optical switch in a novel way to develop a fully optical add/drop multiplexer for modern optical networks. Special detail is paid to the working of the AWG, its design principles, and importance to optical networking. Chapter 3 presents the system developed with three different types of MEMS switches. For each switch configuration, details of the switch operation, fabrication, and performance in the add/drop system are presented.

Chapters 4 and 5 are concerned with the optical gas detection project. Chapter 4 explains the principles behind the detection scheme utilized, namely Non-Dispersive Infrared gas spectroscopy. Chapter 5 details system design and operational performance. Detail concerning the various components of the sensor system is provided along with testing setup and results.

Finally, Chapter 6 summarizes the work presented in the thesis and details continued efforts that are advised for both projects.

CHAPTER 2

ARRAYED WAVEGUIDE GRATING IN AN OPTICAL ADD DROP MULTIPLEXER

Telecommunications networks are facing increasing traffic demands, a trend that will continue for some time into the future. After initially maintaining a capacity surplus compared to the volume and rate of desired information transfer, the user's desires are catching up quickly to the capacity of current networks. One way additional capacity has been enabled is through Wavelength Division Multiplexing (WDM), or its more advanced offspring Dense Wavelength Division Multiplexing (DWDM), which allows multiple information carrying signals of differing, non-overlapping wavelengths to be carried on the same optical fiber. Forty or more wavelength channels are currently supported on a single fiber in modern systems.

While the capacity of the fiber currently still far exceeds the demand on the network, switching capacities are much closer to being a limiting aspect of optical telecommunications. Commercially available optical fiber systems now carry in excess of 1Tb/s of information per fiber. However the largest electronic cross-connects only marginally surpass that rate in total throughput [15]. Additionally, since fibers are bundled together to increase throughput, it is easy to see that switching nodes with much higher capacity will need to be developed.

Today switching of telecommunication signals is achieved electronically. This is performed by demultiplexing the WDM optical signal into its separate channels, then converting these optical signals to electrical signals, doing the switching on electrical circuits, reconverting to optical signals, and multiplexing the channels back onto a single carrier fiber or waveguide. This type of system is shown in

Figure 2.1 and is typically called OEO (for optical-electrical-optical) switching.

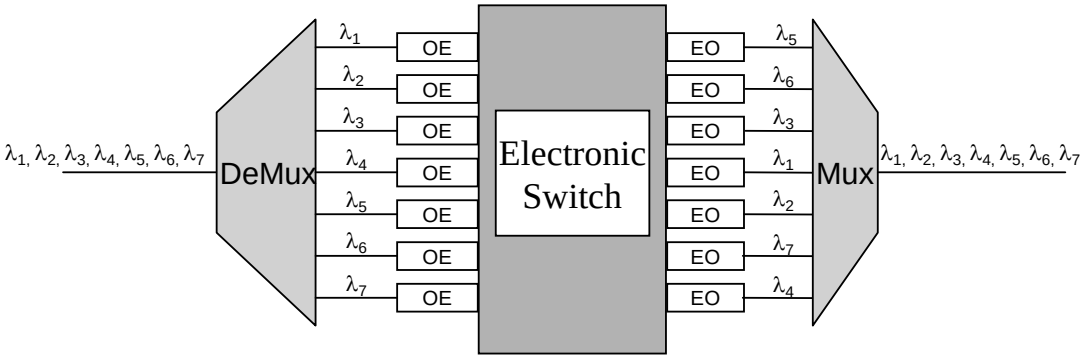

Figure 2.1: A schematic representation of an optical-electrical-optical (OEO) switch. The OE and EO elements optical-to-electrical and electrical-to-optical converters, respectively.

A key element to an optical network is a wavelength selective switch (WSS). A WSS will allow an input signal to be selectively output on one of the multiple outputs to the system [16]. Networks utilizing WSS's have been described and studied for years [17], the components to realize these devices have just begun to mature to the commercially viable level.

In particular, MEMS technology became a hot topic in the mid to late 90s because of the possibility of all-optical switching. The optical-to-electrical and electrical-to-optical conversions in OEO switching are expensive in terms of both time and power consumption [18]. This is especially true when you consider that OEO switching occurs at every node in the network and converts all on the WDM channels even though only 25% are typically handled at a given node [19] [20]. The benefit of all optical wavelength selective switches will be felt increasingly as the fiber domain pushes to the outer reaches of the telecommunications network as in the ongoing development of various "fiber to the home" plans throughout the world.

2.1 Wavelength Selective Switches

Wavelength selective switches are comprised of two sections: a mux/demux section to optically compose/decompose the WDM signal and a dynamic section to provide the selectivity of a particular wavelength channel [21].

The mux/demux section is typically either based on free-space optics, such as a diffraction grating, or a planar lightwave circuit (PLC). A PLC is a collection of optical waveguides arranged or patterned to achieve a particular functionality such as multiplexing a signal or isolating a particular wavelength from a multiplexed signal. PLC-based mus/demux elements for WSS can be Bragg grating waveguide arrays to select a particular wavelengths while passing the remaining signals, but are most frequently Arrayed Waveguide Gratings.

An Arrayed Waveguide Grating is a passive optical device that can be used both for the multiplexing and demultiplexing of optical telecommunication signals. It can simultaneously provide the precise signal handling necessary for the most modern telecommunication standards and the utility of integration on a chip. AWGs have been additionally proposed for the applications including dispersion compensation, tunable filters, and as spectrum-sliced signal sources [22]. AWGs are the preferred methods for lightwave based WSSs because of their excellent optical performance, compact size, and potential for batch fabrication.

The dynamic selectivity section has a far greater number of attempted solutions. In general, MEMS devices are the right size and speed to meet the needs of this problem; and because of their low cost from batch fabrication and compatibility with control electronics are firmly ahead of any other technology in this area. Thermo-optic MEMS switches and reflective surface MEMS actuators are the primary means of achieving the dynamic selectivity of the optical WSS.

A modern example of a free-space optics based WSS can be seen in Reference [23]. A diffraction grating is used both to multiplex and demultiplex the WDM signal while a MEMS 2-axis scanning mirror and a series of telescoping optics is used to steer the optical signals to the appropriate ports. The inherent problem with grating based WSS is both concerns about the physical size as the network size scales and that the various parts (grating, MEMS, optics, fiber, etc.) must be individually assembled [21].

Multiple WSS systems have been proposed based on AWG mux/demux. A recent example is given in Reference [24]. This example is typical in that requires multiple AWGs to achieve the system functionality. In particular, for an N-channel system, this WSS requires 2N AWGs. While AWG manufacturing has improved in the last decade, it is still sufficiently difficult and expensive to make this scaling very poor for actual network implementation. In addition, the 4 channel system shown is already on a large chip (more an 1cm on a side) and would grow with added channels. The dynamic switching is performed with thermo-optic switches, which are more energetically costly than reflective MEMS switches, but are integrable onto the same substrate with the AWG.

This research has focused on a hybrid system combining a MEMS optical switch and an AWG to achieve a fully optical add/drop multiplexer that is reconfigurable to allow any channel to be dropped from or added to the network at any node. An optical add/drop multiplexer (OADM) can be thought of as a particular type of WSS with a wavelength selected to either go to the drop output port or the pass to the network port. Figure 2.2 shows a schematic representation of an add/drop multiplexer's function. The theory of this system is presented in this chapter after a detailed introduction into the workings and design of an AWG. This system

is more elegant and simple than other suggested solutions for WSS because it relies on only a single AWG and utilizes a single MEMS switch (or switch array) to achieve the full functionality. The single AWG allows for excellent scaling to larger networks, as do the MEMS switches used.

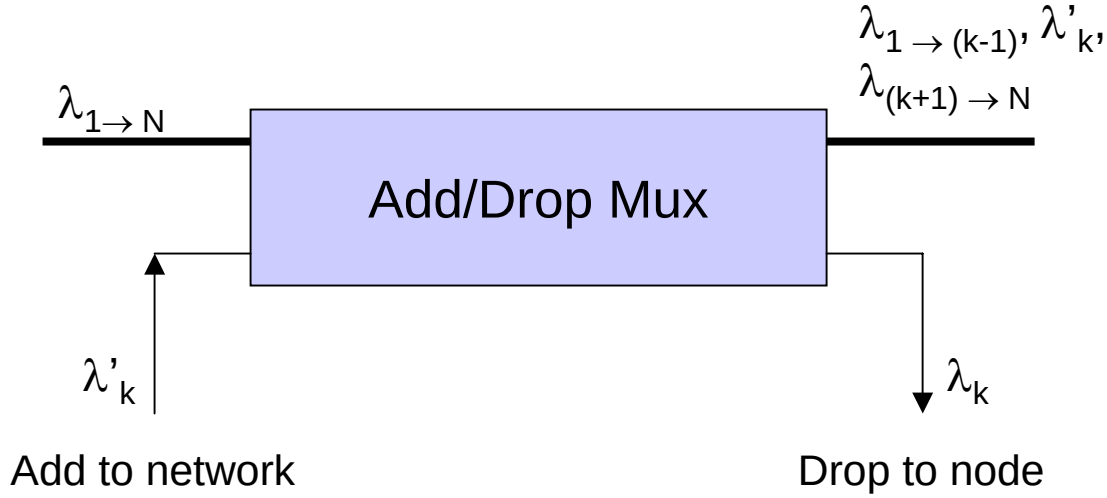

Figure 2.2: A schematic representation of an add/drop multiplexer capable of adding and/or dropping a single channel.

2.2 Physics of an Arrayed Waveguide Grating

An Arrayed Waveguide Grating[1] is a planar lightwave circuit consisting of a collection of waveguides of specific dimensions and spatial orientation designed to separate a WDM signal into its component channels. It is a reciprocal device so it can "run backwards" to combine wavelength channels together into a WDM signal

[1]The AWG was proposed nearly simultaneously and separately by three different groups leading to a war over what it would be called. For that reason the AWG (Takahashi's group) is also frequently called a PHASAR for PHASed ARray (Smit Group) or a Waveguide Grating Router (WGR) (Dragone's group).

simply by reversing the input and output sides. The AWG can be broken up into three sections: a star coupler expansion region, a phased array of waveguides, and a star coupler recombination region [25]. Each of these sections of the AWG will be discussed below with details about their performance and design. Also the way these elements fit together to form an AWG will be discussed. Finally, the use of an AWG in making a reconfigurable Optical Add/Drop Multiplexer (OADM) will be detailed.

It should be mentioned that many types of planar waveguides can be fabricated. These various types of waveguides are shown pictographically in Figure 2.3. While any of these types of waveguides can be used in constructing an AWG or the type of system discussed here, the arguments and descriptions below consider buried channel type waveguides as reference. This is due to the type of waveguides used by our collaborators on this project at ANDevices, Inc. (formerly Axon Photonics Inc.) and for the sake of cohesion. ANDevices of Fremont, CA, USA, is a planar lightwave circuit manufacturer specializing in silica-on-silicon AWGs among other products. Their role as collaborators consisted of supplying AWGs from their commercial stock.

2.2.1 Expansion Star Coupler

A schematic of a star coupler is shown in Figure 2.4. This is a useful device, developed in the late 1980s, in optical networks because it serves to distribute an input signal evenly over many output receivers [26] [27]. Integrated optical star couplers are composed of a slab waveguide region between input and output arrays of channel waveguides. The power from any of the input channel waveguides will be radiated through a slab region toward an output array of waveguides. If properly

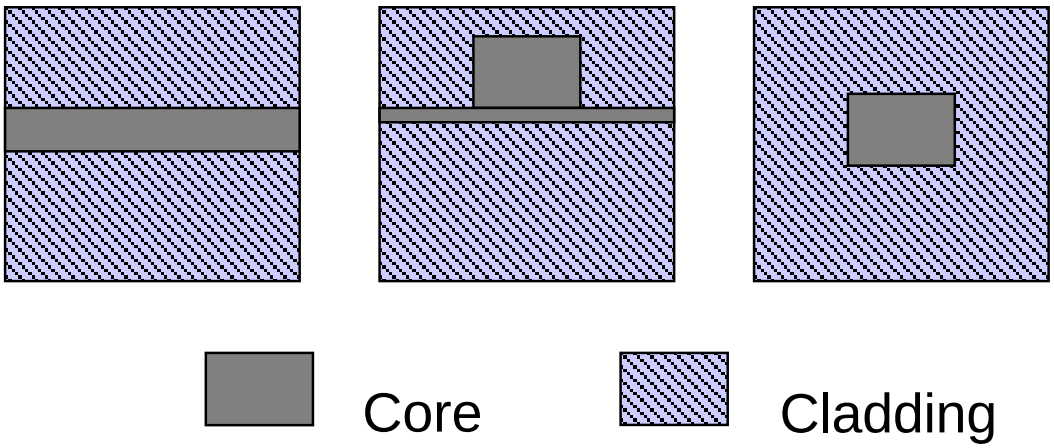

Figure 2.3: The types of waveguides. (Left) Slab waveguide. (Center) Ridge waveguide. (Right) Buried Channel waveguide.

designed the radiation pattern at the output array is uniform over a collection of N waveguides to ensure equal output power distribution.

The radiation pattern at the output side of the slab region is the Fourier transform (or Fraunhofer pattern) of the input radiation pattern. In order to produce as close as possible a uniform "box" function, the inverse Fourier transform of a "box" must be present at the input, which is to say a sinc function. Since the input will almost always be a Gaussian beam profile in a waveguide, the sinc is approximated by allowing coupling between neighboring waveguides at the input to create the necessary sidelobes [28] [29]. To ensure uniform coupling from all input waveguides to collections of output waveguides, dummy waveguides for sidelobe coupling are added to the edges of the waveguide arrays.

Currently star couplers and the subsequent AWGs that contain these couplers no longer use dummy waveguides, instead managing the non-uniformity of the output radiation pattern by other means. These other methods to insure uniform

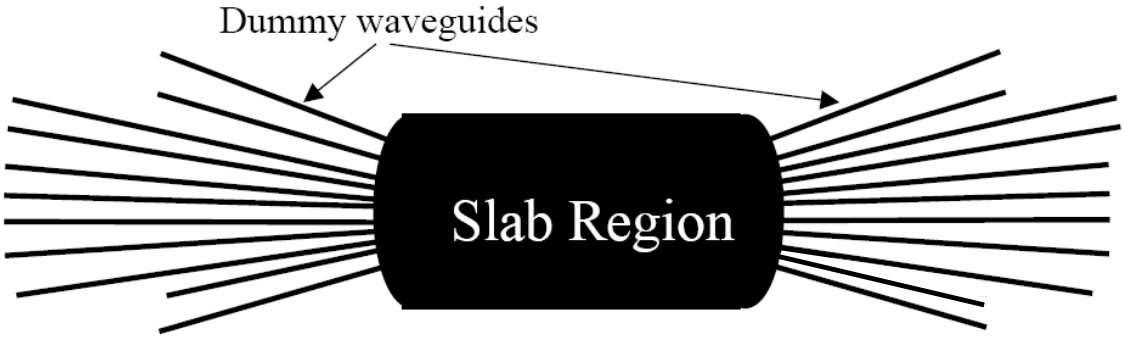

Figure 2.4: Schematic representation of a $N \times N$ star coupler with the dummy waveguides and slab region marked. The dark sections are the higher index core or guiding regions to which the propagating wave is confined.

output radiation include optimized design through simulation of the input and output array's locations to ensure near uniformity at the output array and the use of variable optical attenuators in series with the output waveguides.

Star couplers have been commercially manufactured and available for several years with greater than 256×256 couplers fabricated reliably. Star couplers have been fabricated in Si-SiO_2, GaAs-InGaAsP, polymers, and other materials. Typical loss characteristics, besides the inherent division of power between the N output waveguides is on the order of a few dB [30] due to propagation loss, loss of coupling to a fiber, and general imperfections. Figure 2.5 shows a beam propagation method simulation of a expansion star coupler.

2.2.2 Phased Array

The light from the expansion star coupler is spread uniformly over inputs to a phased array of waveguides. These waveguides are all of identical lateral dimensions, but of precisely controlled path length differences. This length difference in adjacent waveguides, ΔL should be equal to an integer number of wavelengths in

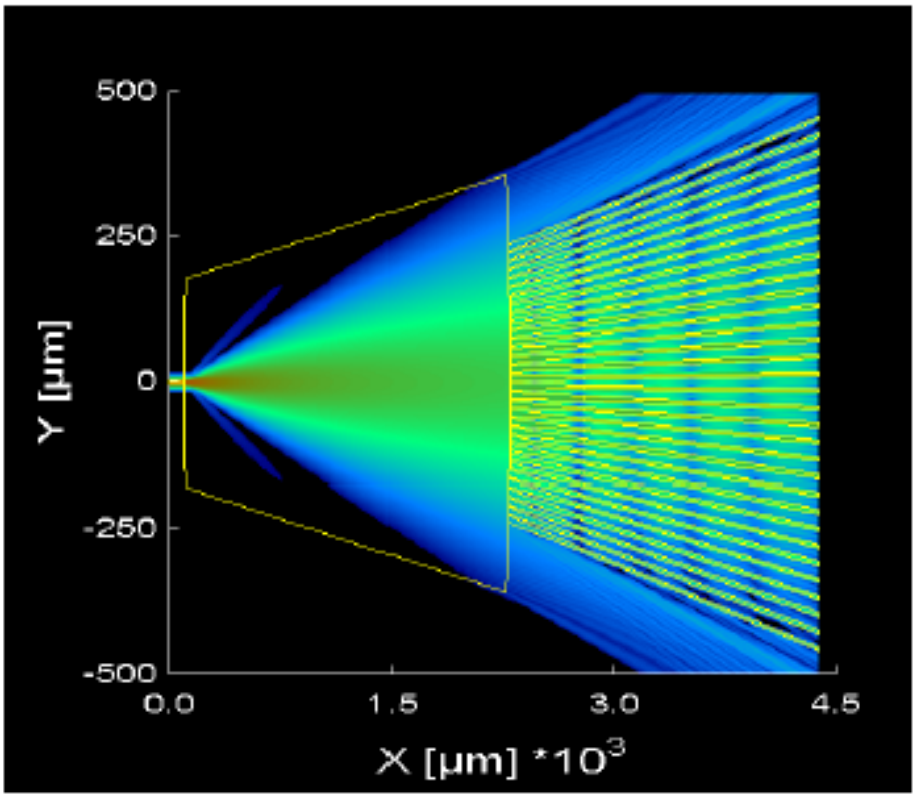

Figure 2.5: Beam Propagation Method simulation of light from coupling from a single input waveguide to an array of output waveguides. The plot shows planar dimensions of the star coupler with the field intensity given by the color (the black background is $\leq -60dB$. The simulation software OlympiOs by Alcatel was used to generate these plots [31].

the waveguide,

$$\Delta L = m\frac{\lambda_c}{N_g} = \frac{mc}{N_g f_c}, \tag{2.1}$$

where m is an integer referred to as the order of the phased array, λ_c is the central wavelength in free space and $f_c = c/\lambda_c$ is the corresponding frequency, and N_g is the effective index of the waveguide mode.

With this setup, light of the central wavelength arrives at the output of the phased array in phase at each output waveguide facet, while light of wavelengths less than or greater than the central wavelength arrives at the output facets with controlled phase differences. The light from the waveguide facets will interact with the light from the other facets creating an interference pattern in the far field. This causes the phased array to perform as a Rowland type lens [32]. The focal line of such a optical system follows a circle of radius $R_a/2$ centered at the output of phased array. Figure 2.6 shows a beam propagation method simulation of the focusing of light from the output of the phased array onto the image plane for light at the central wavelength and less than central wavelength.

2.2.3 Recombination Star Coupler

A second star coupler similar to the expansion star coupler is placed after the phased array. By placing output waveguides along the Rowland circle where the light from the phased array is focused, the light can be coupled out to output waveguides like the expansion star coupler with the input and output sides reverse. By placing output waveguides at the location where various wavelengths are focused, individual WDM wavelength channels can be confined to a particular waveguide. Figure 2.7 shows the full AWG from these components being assembled

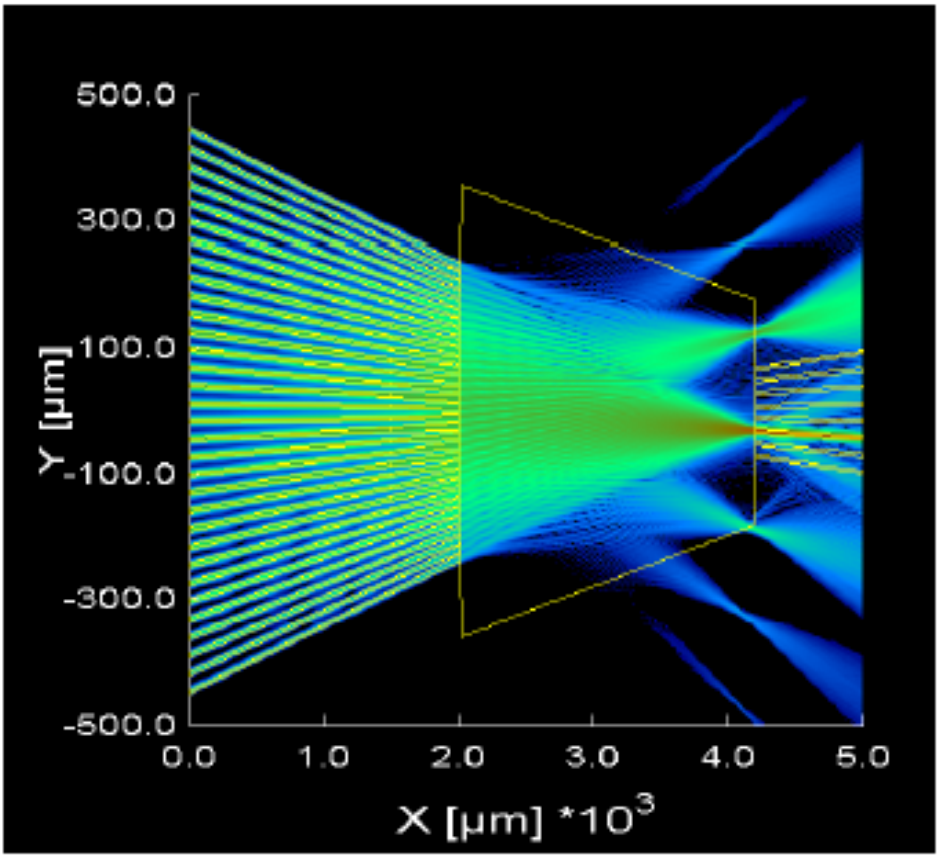

Figure 2.6: Beam Propagation Method simulation of light from emerging from the phased array light at a non-central wavelength $\lambda < \lambda_c$. Note the focus points for various orders fall along a circular curve. The simulation software OlympiOs by Alcatel was used to generate these plots.

together.

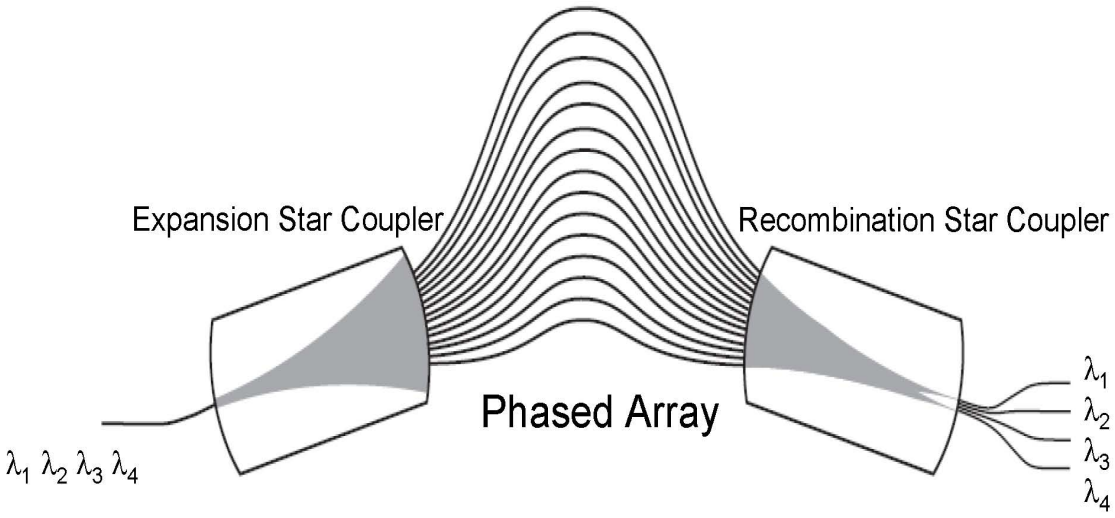

Figure 2.7: Schematic representation of an Arrayed Waveguide Grating showing the various components and representative performance.

2.2.4 N×N Cyclic Frequency AWG

To summarize, an AWG takes in a WDM signal on a single waveguide which is expanded through the expansion star coupler to evenly distribute all the various included wavelengths of light into a phased array of waveguides. This waveguide array has a well controlled difference in pathlength for various wavelengths travelling along it, causing the light exiting the phased array to have a distribution of phase among the output waveguides depending on frequency of the light. The light from the array creates an interference pattern that is focused along a Rowland circle with different wavelengths focused to different locations on that circle. By placing output waveguides at appropriate positions on the Rowland circle a recombination star coupler is created, and individual wavelengths are coupled into a particular output waveguide for a demultiplexed signal. Reciprocally, if a demulti-

plexed WDM signal is input to the waveguides at the recombination star coupler, a multiplexed WDM signal will be output on a single waveguide from the expansion star coupler.

AWGs can be designed with various special characteristics in addition to the performance described above. AWG with flat spectral response can be developed by the addition of dummy waveguides in the star couplers as discussed above or by introducing addition amounts of loss in each waveguide in the phased array. Unequal output channel spacing AWGs can be produced by simply choosing the correct places for output waveguide locations. So called Variable Bandwidth AWGs, which can act as variable bandwidth filters, can be achieved by varying the width of input and output waveguides. Additionally filtering AWGs and temperature insensitive AWGs can be manufactured. This project deals with a particular type of AWG called a Cyclic Frequency AWG [33] [34].

The cyclic frequency AWG is achieved by corresponding the location of the output waveguides to the channel spacing and number of channels in the WDM signal being handled, so that multiple modes will be focused to the same location. Precise details on appropriate design principles will be described in the following section. The resulting performance is that the channel wavelength output on a particular waveguide can be cyclically changed by adjusting which input waveguide the WDM signal is present. Thus any wavelength can be confined to any desired output waveguide to be handled as necessary in the network [35]. This performance is schematically depicted in Figure 2.8.

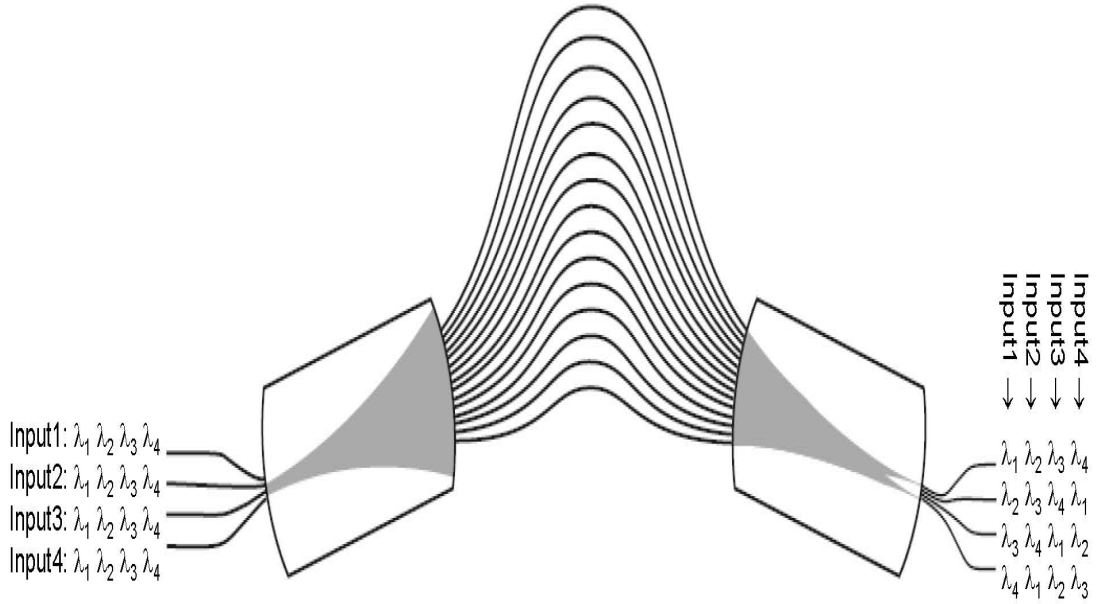

Figure 2.8: Schematic depiction illustrating the performance of an 4×4 cyclic AWG, also commonly called a wavelength router. The cyclic AWG accepts a multiplexed signal ($\lambda_1 through \lambda_4$) and outputs a demultiplexed signal with arrangement dependent on which input channel was used. For instance, with input channel 2, output channels 1 through 4 propagate λ_2, λ_3, λ_4, and λ_1 respectively.

2.3 Design of Arrayed Waveguide Grating

In this section, the design principles for a cyclic frequency AWG are presented. Special attention is paid to the process limitations from the Berkeley Microlab and the fabrication facility of ANDevices. Specific choices for optical networking design specifications such as channel number and spacing was determined by modern International Telecommunications Union (ITU) standards. Decisions such as these will be pointed out when they are made.

There are many degrees of freedom in AWG design and hence many design approaches [36] [37]. The approach that follows is based on the highly successful and early developed ones from Delft University of Technology [38] and NTT [30]. Please refer to Figure 2.9 for definition of the various layout variables.

Initially, certain network conditions are set in accordance with commercial standards. Specifically, a WDM signal with $N = 40$ channels centered at wavelength $\lambda_c = 1552$nm with channel spacing of $\Delta\lambda_{ch} = 0.8$nm is desired for the Telcordia GR-1221 qualifications.

2.3.1 Waveguide Parameters

To begin, the width of waveguides to be fabricated is set and the V-parameter (or dimensionless waveguide width) for the waveguides is selected. The V-parameter is defined as:

$$V = \frac{\pi w}{\lambda_c}\sqrt{n_{core}^2 - n_{clad}^2} \tag{2.2}$$

Both of these decisions are determined by processing capabilities and propagation mode considerations. The standard values for ANDevices designs were used, with the width at $w = 5\mu m$ and $V = 3$.

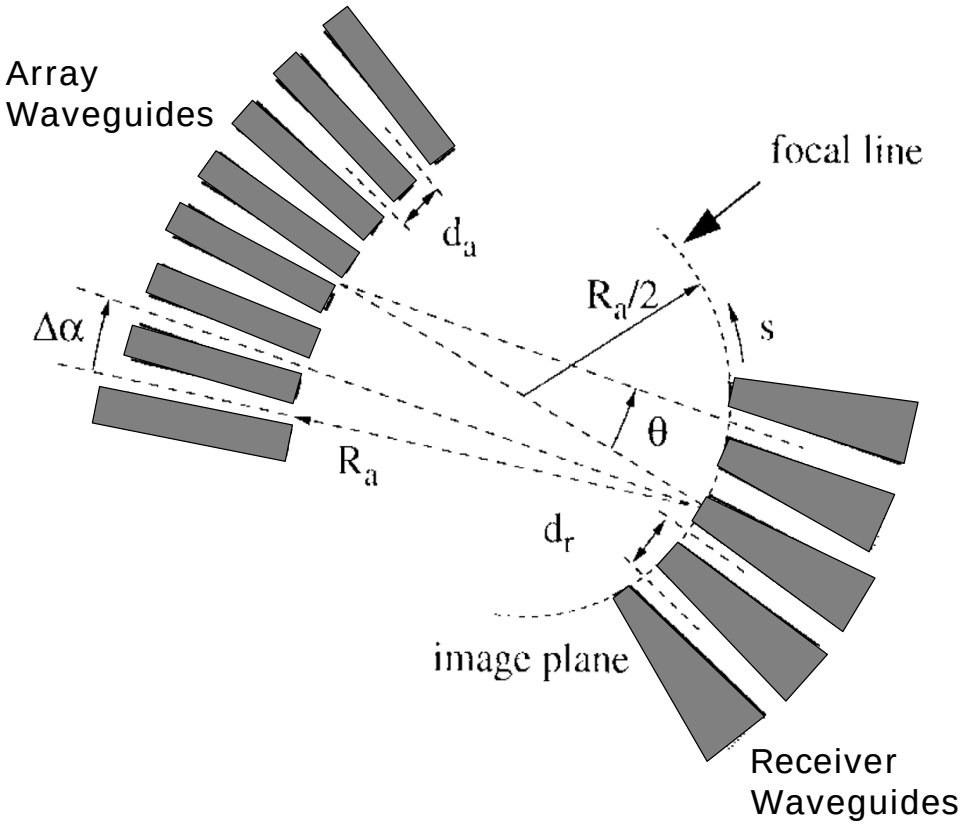

Figure 2.9: Non-scale geometry of recombination star coupler. Various device parameters are defined by this image. Note also that for design symmetry, the expansion star coupler will have identical dimensions. Based upon [38].

2.3.2 Receiver Waveguide Spacing

With these two values set, the receiver spacing d_r can be defined. By specifying a particular allowable crosstalk level, d_r can be determined graphically from standard waveguide calculations like that shown in Figure 2.10. For $V = 3$ and a maximal cross-talk of 40 dB, which is a standard level allowable in commercial telecom systems, the ratio $d_r/w = 3$. Thus $d_r = 15\mu$m.

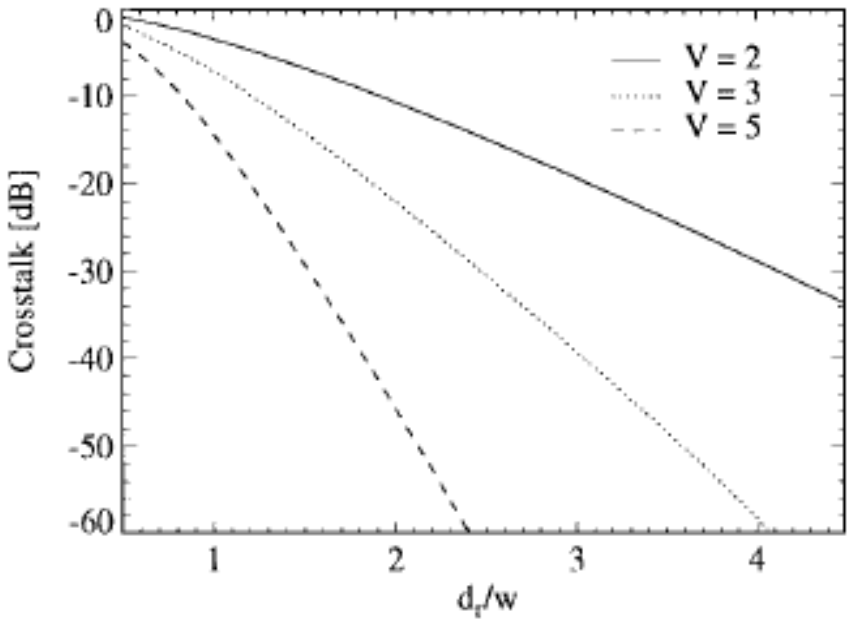

Figure 2.10: Crosstalk vs. d_r/w. This type of graph is used to determine d_r given a choice of w and V.

2.3.3 Non-uniformity Loss & and Minimal Length for Free Propagation Region

Next the length of the slab waveguide region of the star coupler, also known as the Free Propagation Region (FPR) length R_a is calculated. From Figure 2.9 it

is clear that $R_a = \frac{s_{max}}{\theta_{max}}$ where s_{max} is the position on the Rowland curve of the outermost receiver waveguide. θ_{max} is related to the loss at the outermost receiver waveguide compared to the center waveguide:

$$L_u = -10log(e^{-\frac{2\theta_{max}^2}{\theta_0^2}}) \approx 8.7 \cdot \frac{\theta_{max}^2}{\theta_0^2}. \tag{2.3}$$

θ_0 is the width of the Gaussian far field after expansion through the slab waveguide region of the star coupler and is given by:

$$\theta_0 = \frac{\lambda}{n_{slab} w_e \sqrt{2\pi}}, \tag{2.4}$$

where w_e is the effective waveguide mode effective width. The waveguide mode effective width is found empirically [38] to be

$$w_e \approx w(0.5 + \frac{1}{V - 0.6}) \tag{2.5}$$

in the given range of V used here.

Lastly, s_{max} must be calculated to have all the necessary parameters defined to determine R_a. The s axis is along the Rowland curve and is defined to have a zero point at the center of receiver waveguide array. Therefore the value of s_{max} is given by

$$s_{max} = d_r \frac{N_{ch} - 1}{2}. \tag{2.6}$$

So with the choices of $V = 3$ and $w = 5\mu$m, using Equations 2.3 through 2.6 the minimal $R_{a,min}$ can be calculated. Typical values are on the order of a few mm, although R_a is often as large as a cm or more.

2.3.4 Length Increment

After a change of 2π in the phase difference between neighboring waveguides, $\Delta\Phi$, the field will be imaged at the same position. That is to say the response field of

the phased array is periodic. This period in the frequency domain is defined as the Free Spectral Range (FSR) of the AWG.

Next the length increment between neighboring waveguides in the phased array, ΔL, is determined. To ensure a cyclic AWG, the choice of ΔL is very specific, since the frequency shift of the FSR must be equal to the number of channels multiplied by the channel spacing, $\Delta f_{FSR} = N_{ch}\Delta f_{ch}$. As defined above the FSR is given by the frequency shift for which the phase shift from the phased array is equal to 2π, or in equation form

$$\frac{2\pi\Delta f_{FSR}}{c}\tilde{N}_g\Delta L = 2\pi, \tag{2.7}$$

where $\tilde{N}_g$ is the group index of the waveguide mode,

$$\tilde{N}_g = N_g + f\frac{dN_g}{df}. \tag{2.8}$$

and N_g is the effective index of the waveguide mode.

By combining the above equations, the length increment to ensure cyclic AWG performance is

$$\Delta L = \frac{mc}{\tilde{N}_g N_{ch}\Delta f_{ch}}, \tag{2.9}$$

with m an integer known as the order of the phased array.

2.3.5 Length of Free Propagation Region

The minimal length of the free propagation region $R_{a,min}$ was determined by a limit set on non-uniform loss across the output waveguides, but the exact value can be determined by the dispersion of the array. The dispersion is defined as the displacement along the s curve per unit frequency change

$$D = \frac{ds}{df} = \frac{d_r}{\Delta f_{ch}} = R_a\frac{d\theta}{df} = \frac{\tilde{N}_g\Delta L}{f_c N_{slab}\Delta\alpha}. \tag{2.10}$$

Rearranging to solve for the divergence angle $\Delta\alpha$ (see Figure 2.9),

$$\Delta\alpha = \frac{\tilde{N}_g \Delta L \Delta f_{ch}}{f_c N d_r}. \tag{2.11}$$

R_a is determined by $\Delta\alpha$ and the waveguide separation according to

$$R_a = \frac{d_a}{\Delta\alpha}. \tag{2.12}$$

The array waveguide spacing d_a is still a free choice, but it is usually chosen to be equal to the receiver waveguide d_r spacing for fabrication uniformity. Beyond this rule of thumb, it is advantageous to keep d_a as large as possible to minimize mode coupling between the array waveguides, which can cause so called "ghost images" in the interference pattern.

2.3.6 Aperture Width

The aperture width is characterized by the angular half width θ_a of the array aperture. θ_a is determined graphically by plotting the simulated crosstalk power vs. θ_a/θ_0. For the desired crosstalk of -40dB, $\theta_a/\theta_0 \approx 2$.

2.3.7 Number of Array Waveguides

The final parameter to determine is the number of array waveguides, N_a, which is fixed by the choice of θ_a.

$$N_a = 2\frac{\theta_a R_a}{d_a} + 1 \tag{2.13}$$

Typical values for N_a for designs like this one are in the multiple hundreds.

2.4 Design of 40 Channel Cyclic AWG

For this project a 40-channel cyclic AWG centered at 1552nm wavelength was designed. It was to be fabricated by the collaborators at ANDevices. The various design parameters are outlined in Table 2.4.

Table 2.1: Parameters of designed 40-channel cyclic AWG.

Parameter	**Specification**
Number of wavelength channels	40
Central wavelength λ_c	1552nm
Channel spacing $\Delta\lambda$	.8nm
Waveguide width	5μm
V-parameter	3
Receiver waveguide spacing d_r	15μm
Non-uniformity loss L_u	3dB
Free propagation length	2.1cm
Length increment ΔL	1.5
Array aperture angular half-width θ_a	2^o
Number of Array Waveguides N_a	280

2.5 Reconfigurable Optical Add/Drop Multiplexer

Now that the creation of a cyclic AWG has been explained, the use of that element in a fully optical add/drop multiplexer can be explored [39]. Also know as a wavelength router or wavelength selective switch, OADMs have become extremely interesting since the number of add/drop elements with optical input and outputs

is set to increase exponentially with the expansion of the optical network around the world and in fiber to the home systems [40]. The losses in energy and switching speed due to OEO switching will become increasingly prohibitive to upgrading an optical network [41].

While the design and fabrication of AWGs has rapidly improved in the past decade, the number of companies producing commercially viable AWGs is still very small because small variations in process parameters can lead to changes in mode propagation in the waveguides. These variations occur both in the form of wafer to wafer inconsistencies, but also in single device difficulties since AWGs are so physically large compared to most microdevices that maintaining film thickness, stress, temperature gradient, and other parameters across the surface of the wafer can be problematic.

Figure 2.11 shows a schematic for the OADM system proposed based on single cyclic AWG and a MEMS based optical switching between inputs. As discussed earlier, using an AWG as the mux/demux component of a WSS is preferable because of its excellent optical properties (low cross-talk, low insertion loss, etc.), batch fabrication, compact size, and potential integration with other components. This design is preferable to many alternative wavelength selective switches because it only utilizes a single AWG regardless of the density of the network. Light input to the system, will be switched to a selected input waveguide, demultiplexed by the AWG with the appropriate signal going to the drop channel output wavegide. The pass channels can be reflected back through the AWG to be multiplexed for continued transmission. A circulator is used to separate the input and output signal paths. Finally, an add channel can be included to the node at the output end.

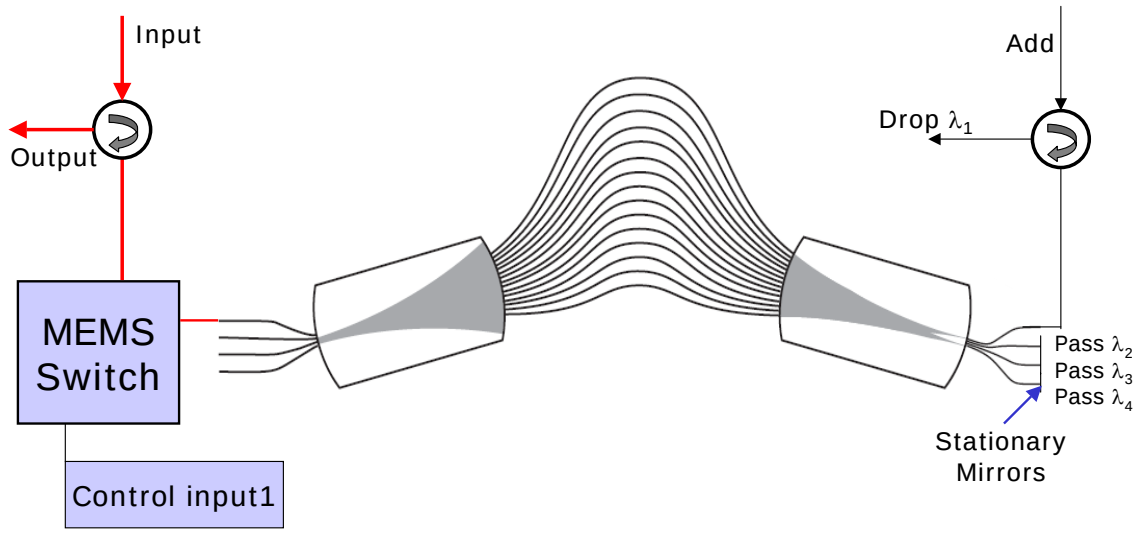

Figure 2.11: A design for an Optical Add/Drop Multiplexer with a single Arrayed Waveguide Grating and a MEMS optical switch. The AWG is used both to multiplex and demultiplex the signal. By switching the input light between input waveguides with the MEMS switch, the selected drop channel is cycled to the drop port.

The question is, “How best to switch the inputs to the AWG?” The next chapter presents three different MEMS devices for switching the input light signal and the results achieved with each one.

CHAPTER 3

OPTICAL ADD/DROP MULTIPLEXER

This chapter presents three different MEMS devices tested as possible optical switches to use in unison with an AWG to complete an OADM system (see Figure 2.11). In addition to achieving output tuning/switching at desirable power levels, the further goal is to find a design that enables scalable integration for the complete system to achieve a single package OADM.

3.1 Fiber Actuator

As is often the case as a first approach to a project, any device that could move an input light signal was considered, with availability the primary selling point. The first device used was a lateral fiber actuator previously fabricated within the group at the time for a different project. These devices are from a project on optical coherence tomography by Dr. Daniel McCormick and interest in their design beyond what is presented here can be found in References [42] and [43].

3.1.1 Theory & Design

A Scanning Electron Microscope (SEM) image of the fiber actuator is shown in Figure 3.1. Lateral electrostatic comb drives are used to move a long arm from side to side (orthogonal to its longest dimension and in the plane of the wafer). An optical fiber is attached to this long movable arm to be actuated by the device. The main design elements of such a MEMS device are the spring element and the actuator. Folded flexure springs were used and are shown in Figure 3.2. The springs are 290μm long, 2μm wide, and 35μm thick.

The device actuation is driven by numerous banks of electrostatic comb drives,

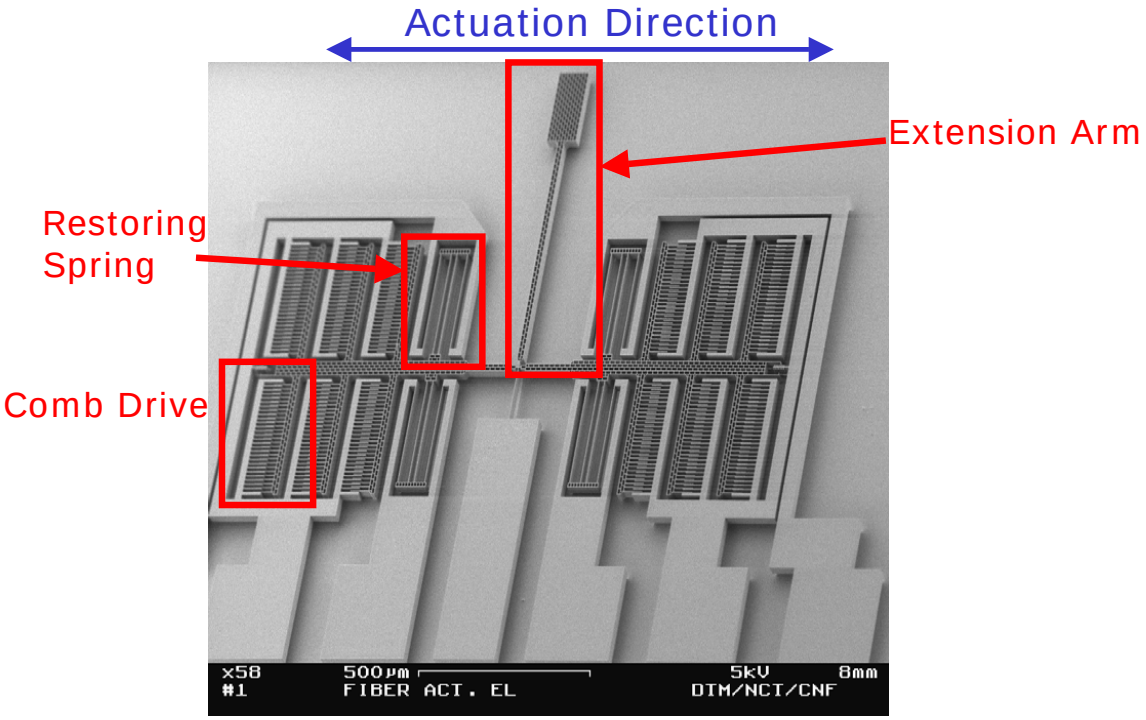

Figure 3.1: Scanning Electron Microscope image of the fiber actuator. Actuation is achieved by applying a voltage bias on the comb drive banks. Direction of actuation for the extended arm is indicated by an arrow. One of the electro-static comb drives and restoring springs are highlighted as is the extension arm that holds the fiber. Image by Dr. McCormick.

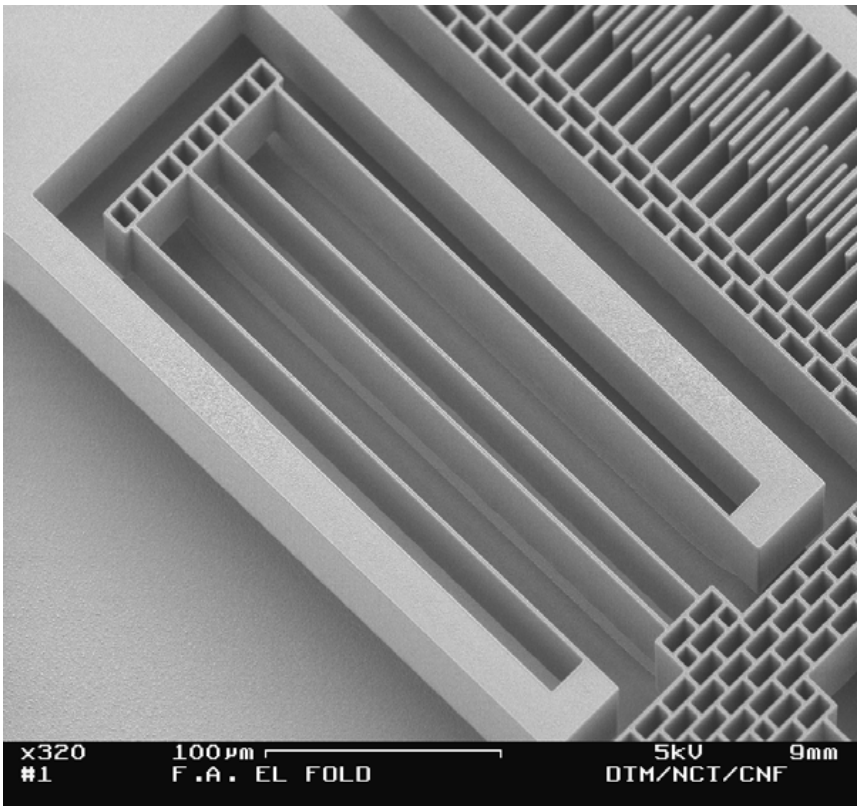

Figure 3.2: Scanning Electron Microscope image of the folded flexure restoring spring of the fiber actuator. Image by Dr. McCormick.

a close up of which is shown in Figure 3.3. A large number of comb drives were used to generate the forces necessary to move the extension arm even when an optical fiber was attached to it. The comb drives consist of inter-digitated fixed and movable fingers that are each 60μm long, 2.5μm wide, and 35μm thick with a finger to finger gap of 3.5μm and a zero bias potential overlap of 30μm. Greater detail concerning lateral actuator design characteristics can be found in Section 3.3.1.

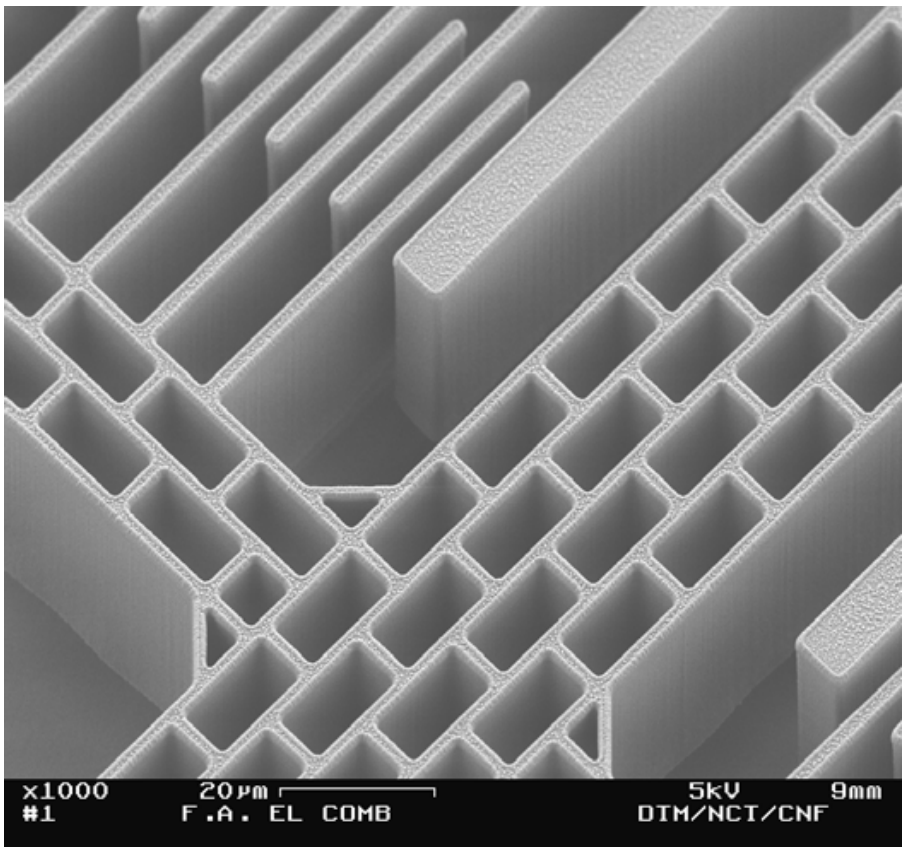

Figure 3.3: Scanning Electron Microscope image of an electrostatic comb drive for the fiber actuator. Image by Dr. McCormick.

These devices were designed to scan an optical fiber tip for use in an optical coherence tomography (OCT) system for analyzing biological tissue structure and motion. For OCT project specifications the devices were designed to operate a

resonance frequency in the range of 1-10 kHz. However, for testing as an optical switch input to the AWG, the devices were operated at DC or low frequency levels (10 Hz or less), which resulted in far less lateral motion.

The optical fiber to be moved by the actuator was a single mode, commercial, fused silica fiber with core diameter of 9μm and cladding outer diameter of 125μm. Because of the high Young's modulus of silica and the large size and weight of the fiber compared to the actuator, the fibers were thinned by a timed hydrofloric (HF) acid etch until the cladding outer diameter was approximately 15μm. The thinned fibers were visually inspected for defects, cleaved, and attached to the actuator arm by with epoxy.

The thinned fibers were found to be very leaky at the points where epoxy beaded along its length. The epoxy's optical properties allowed coupling out of the thinned fiber at these beads by destroying the condition for total internal reflection. To alleviate this problem a thin $(100 - 200nm)$ layer of titanium/tungsten metal was deposited by electron beam sputtering to the thinned fibers prior to their cleaving and attachment to the actuator arm.

3.1.2 Fabrication

These devices were fabricated by the SCREAM process [44] at the Cornell Nanofabrication Facility. The SCREAM process as maintained at CNF is outlined in detail with machine specifications in Appendix A.

3.1.3 Performance of System

Figure 3.4 shows the basic setup for the test that was performed in this experiment. The actuator scans an input fiber along the input Rowland curve of the slab

waveguide region of the expansion star coupler of an AWG.

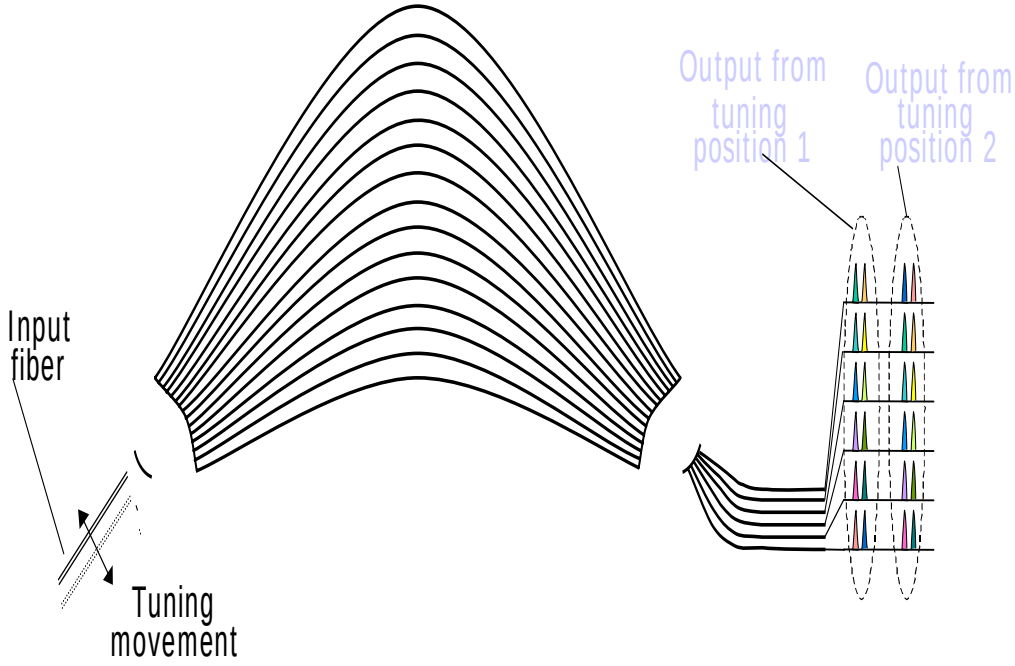

Figure 3.4: A schematic of the OADM system tested using the fiber actuator. The fiber is scanned laterally in the direction indicated.

The fabricated devices used in this experiment had a maximum measured scan angle without a fiber attached of 20^o at 2.7kHz with an applied voltage of 65V. After attaching the fiber, the same devices have a scan angle of 5^o at 7.8kHz and 80V. With a working distance of 3mm the 5^o scan angle translates to a linear scan of 340μm. For testing with the AWG, the devices were operated at DC and 10Hz signals and achieved a scan with a fiber attached of 10μm at 85V for the same working distance. At bias voltages around 90V the actuators exhibited pull in and ceased to function.

A 40-channel silica-on-silicon AWG was fabricated by ANDevices using Chemical Vapor Deposition (CVD) techniques. The AWG was tested and found to have

a central wavelength of 1547.87 nm, an average maximum loss of 6.867 dB, and a total crosstalk of approximately -31 dB between channels. The input ports were cleaved off to allow direct coupling of the input fiber into the free-propagation region, see Figure 3.5. The output ports were butt coupled to connectorized optical fibers. It should be noted that the AWG used in this test was not a cyclic device. It was an out-of-spec test device generously donated by ANDevices.

A continuous shifting of the wavelengths is observed with motion of the input fiber along the Rowland curve. An external cavity tunable laser was used as the light source, and an optical spectrum analyzer was used to detect the output signal. Figure 3.6 shows the result of manually moving the AWG along the input using a micro-positioner. A working distance of roughly 50μm was used. Approximately 15μm of movement is necessary for 0.8 nm shift of the wavelength output at a given port, which corresponds to the ITU standard 100 GHz telecom channel spacing.

Next the above experiment was repeated with the MEMS actuator being utilized to move the input fiber. A wavelength shift of approximately 0.25 nm was observed with 60 DC volts applied to the device, Figure 3.7.

3.1.4 Conclusion

The tuning performance of the AWG was shown to operate as desired under adjusting of the input light position. However, the actuator could not supply sufficient displacement to display full channel switching. The limited displacement of this type of MEMS actuator could be offset by designing of new AWGs to require smaller input waveguide separation for switching. However, additional problems with this implementation of the system exist.

Firstly, the device yield is greatly reduced by the delicate and problem-filled

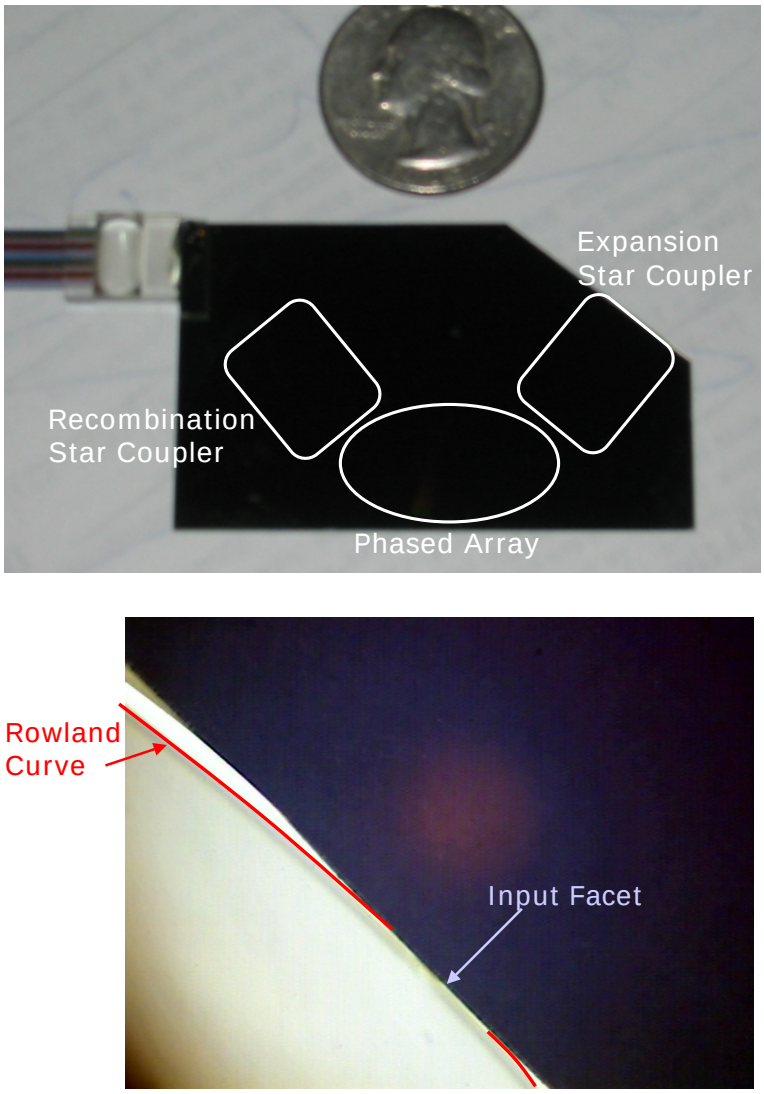

Figure 3.5: Images of the cleaved input AWG. (Top) Digital photo of the AWG cleaved at the input to the expansion star coupler. The various regions of the AWG have been denoted. (Bottom) 50x magnification of the cleaved input with the Rowland curve highlighted.

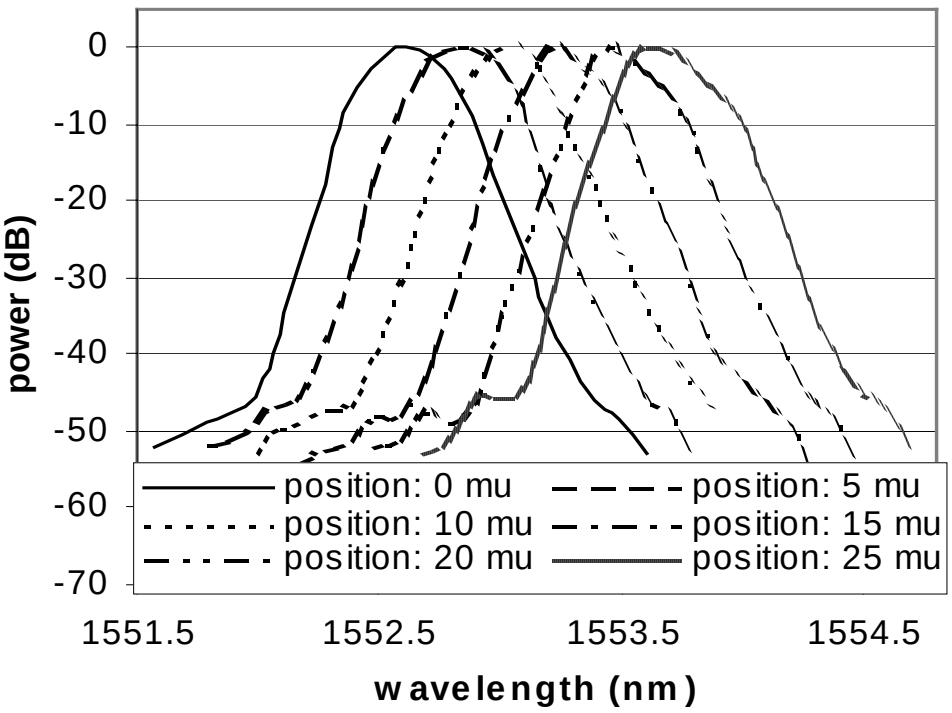

Figure 3.6: The thinned fiber input was manually moved along the cleaved input facet of the AWG. Transmission spectra at a particular output were recorded at various positions to measure tuned frequency as a function of displacement.

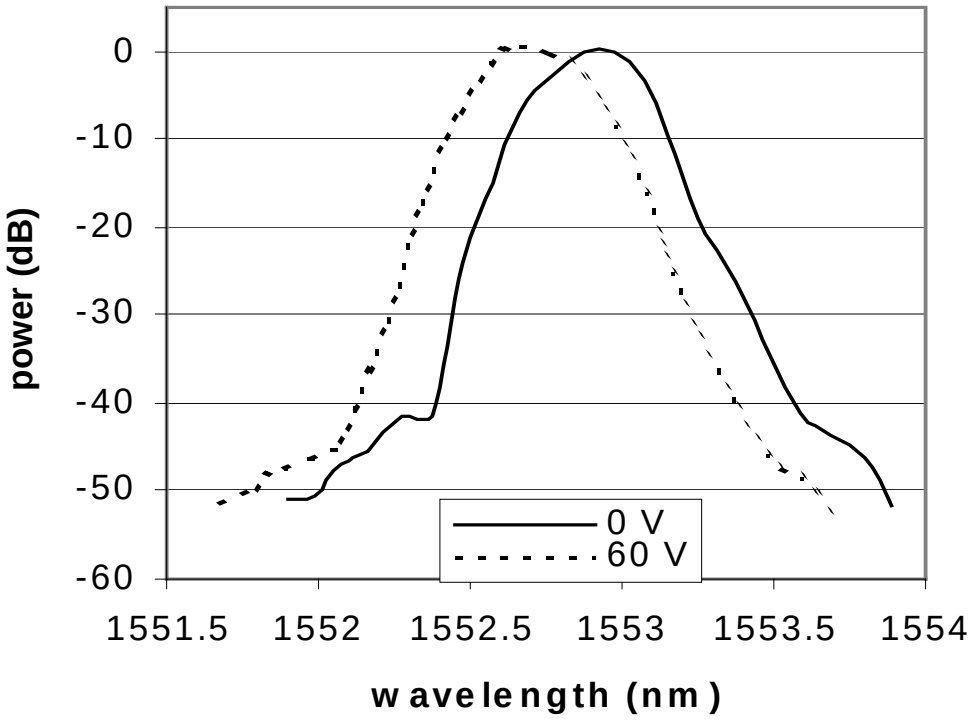

Figure 3.7: The thinned fiber input was moved along the cleaved input facet of the AWG by applying voltage bias to the comb drives of the fiber actuator. Transmission spectra at a particular output were recorded at the zero point and max-deflection positions to measure tuned frequency as a function of applied voltage.

fiber thinning and attachment processes. Secondly, a definite limit on redesigning the AWGs to compensate for the limited lateral actuation exists. Lithographic and loss considerations limit how closely the input waveguides of the expansion star coupler can be pressed together, or equivalently, how great the curvature of the Rowland curve can be. Thirdly, the problem of the diffraction of the light exiting the fiber causes the light coupling into the slab waveguide of the AWG to have a much larger beam profile. This problem can be mitigated by operating the system in an index matching fluid that is matched to the guiding core of the fiber. This type of MEMS actuators work very well in such a fluid, in some cases with better performance than in air. The size of the beam waist from diffraction can be calculated from [30]:

$$W(z) \cong \frac{\lambda z}{\pi n d} \tag{3.1}$$

where d is the fiber diameter, n is the surrounding medium's index of refraction, z is the distance traveled from the end of fiber, and λ is the wavelength of radiation. The size of the beam waist versus the distance from the end of the fiber for both background and in a matching fluid is shown in Figure 3.8. And finally, the fiber actuator is not integrable into a single package with the AWG.

For all the above reasons the fiber mover type of actuator was abandoned for this system.

3.2 Scanning Mirror Actuator

Since the significant problems with the fiber actuator were found to be limited scan of the optical beam and beam broadening after the signal left the fiber before entering the AWG, the next attempt was made with free space optics using a scanning micro-mirror [45]. Scanning mirrors are one of the great successes of

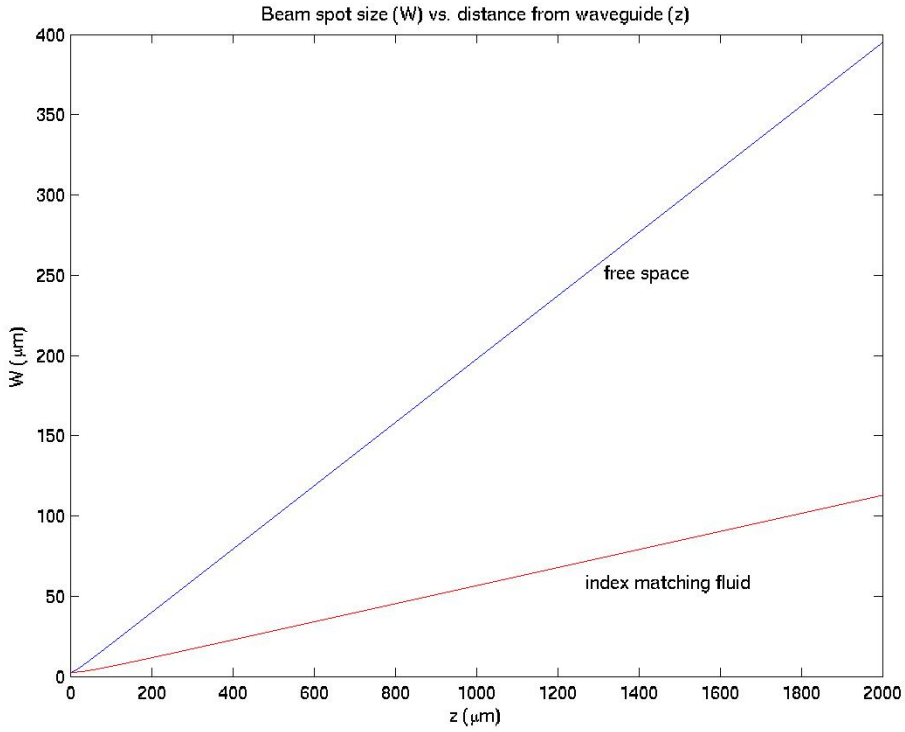

Figure 3.8: Gaussian beam waist of light with $\lambda = 1550nm$ exiting from a silica optical fiber as a function of distance from the end of the fiber. The beam waist is calculated for both interfaces in air and in index matching fluid.

the optical MEMS revolution of the late 1990s as many different scanners were created with a great range of sizes, scan angles, fabrication methods, and frequency responses [46] [47] [48] [49]. Again, the choice of actuator was made by availability of a particular mirror that met the system requirements. The particular scanning mirror was a torsional spring, vertical comb-drive actuated silicon mirror with gold coating for better electrical performance and optical reflectivity.

The scanning mirror used for this experiment was a general purpose torsional electrostatic comb-drive mirror. A schematic of a torsional electrostatic comb-drive mirror is shown in Figure 3.9. The mirror is made of two single crystal silicon layers separated by a layer of silicon dioxide that is a couple of microns thick. The mirror, moving comb teeth, and torsion hinge comprise the top silicon layer, while the fixed comb teeth are in the lower silicon layer. The torsion hinge is anchored to the lower (substrate) silicon layer. A bias potential between the fixed and movable combs creates an electrostatic force between the combs causing a torque on the mirror which makes it tilt. The mechanical strain on the torsion hinge creates the restoring force.

3.2.1 Theory & Design

The capacitance C in an elemental cell of the vertical comb drives is given by

$$C = \frac{2\epsilon_0}{g} A(\theta) \tag{3.2}$$

where ϵ_0 is the permitivity of free space, g is the gap between comb fingers, and $A(\theta)$ is the area of comb overlap as a function of tilting angle, Figure 3.10. This capacitance leads to an electrostatic force F_e between the N combs and a torque

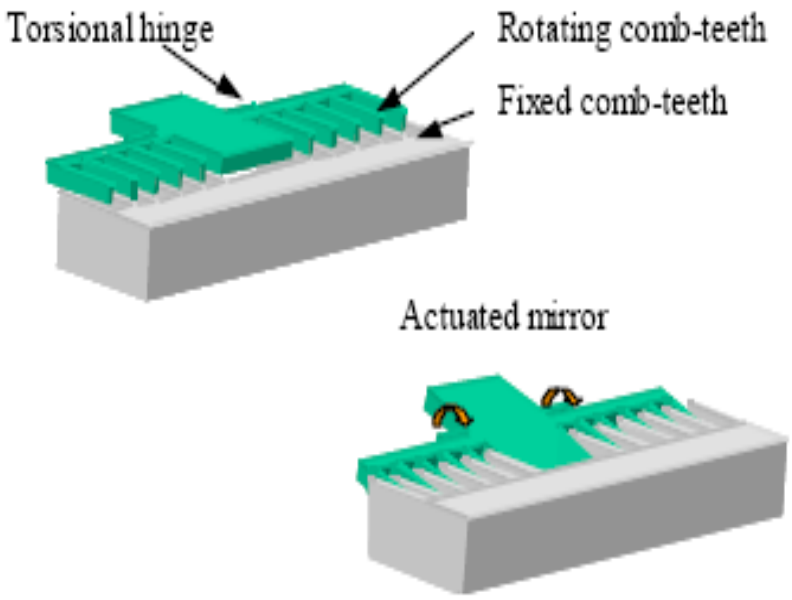

Figure 3.9: A torsional electrostatic comb drive scanning micro-mirror. The fixed comb-teeth are part of the bulk substrate, while the rotating teeth are released and anchored only through the thin torsional hinge.

on the torsional hinge T

$$F_e = \frac{N}{2}\frac{dC}{dy}V^2 \tag{3.3}$$

$$T = \frac{N}{2}\frac{dC}{d\theta}V^2. \tag{3.4}$$

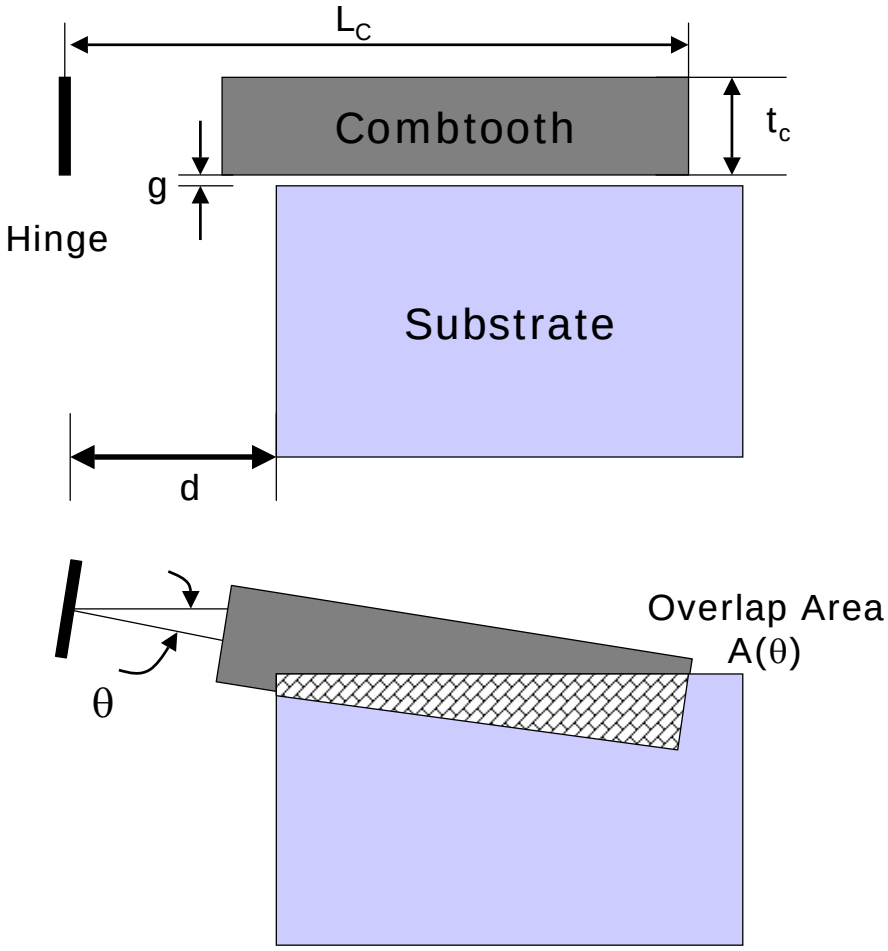

Figure 3.10: Vertical comb drive dimensional parameters in zero position and angled with a maximum torque.

The change in overlap angle θ increases from zero at the unactuated position to θ_{max} when the overlap area reaches a maximum. The torque at the maximum

position is

$$T_{max} \approx \frac{V_{max}^2 N \epsilon_0 (L_c^2 - d^2)}{2g}, \tag{3.5}$$

where fringe field effects have been ignored. The tilt angle at the maximum torque is

$$\theta_{max} = \arcsin(\frac{g_0 + t_c}{L_c}). \tag{3.6}$$

Typically, a system is designed for a particular tilt angle and Equation 3.6 is used to calculate the comb length, while the comb thickness and layer offset is set by fabrication limitations [50].

The mirror used in this experiment has a rectangular torsional hinge and roughly 200 comb pairs. The mirror face is 2.4mm×1.4mm. An image of the mirror is shown in Figure 3.11.

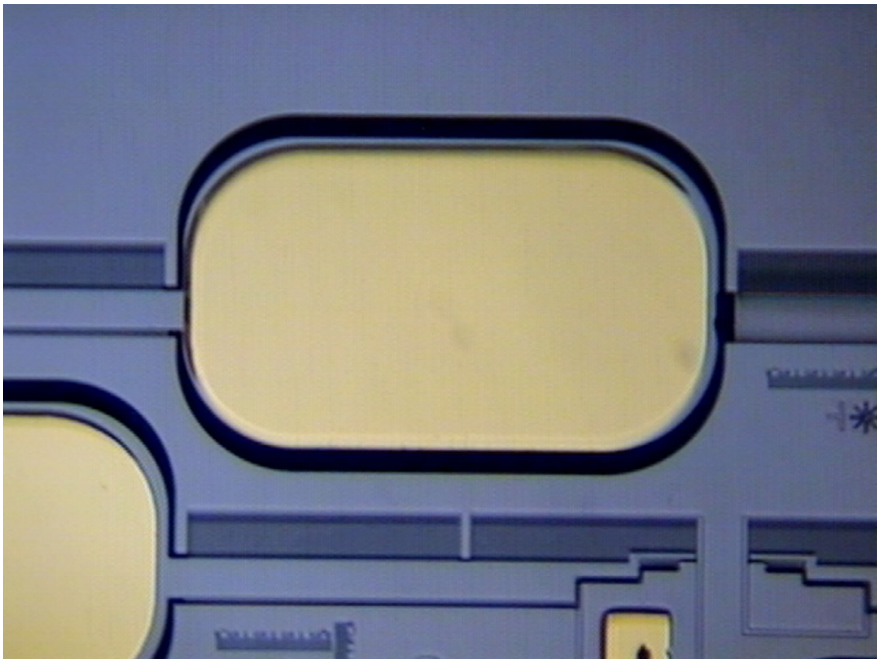

Figure 3.11: Magnified image of vertical comb drive scanning micro-mirror.

The mirror scan performance was characterized; and it achieved a mechanical

scan angle of 8^o at 160V. Figure 3.12 shows the relationship of the scan angle to the driving voltage.

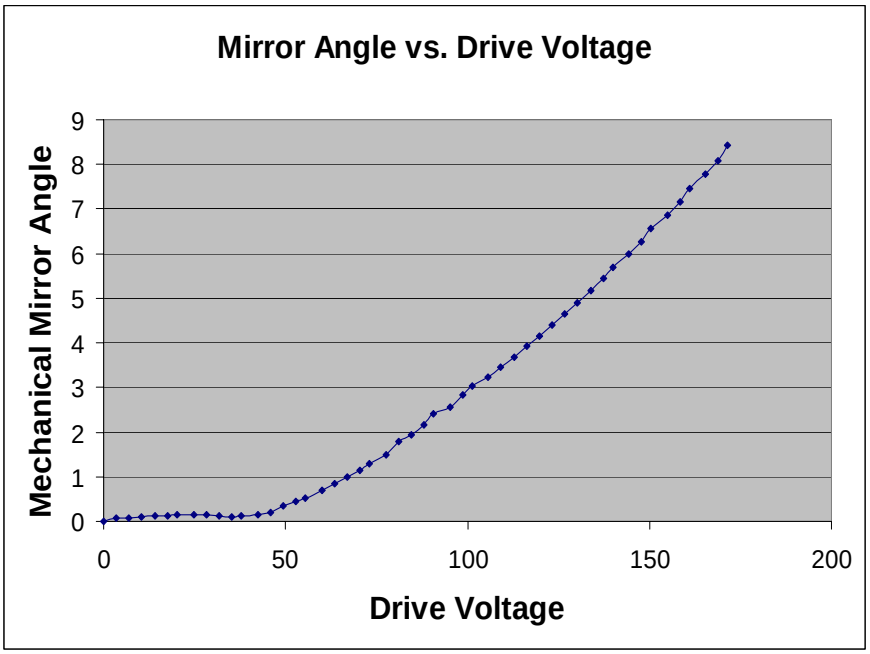

Figure 3.12: Scan angle vs. applied voltage for vertical comb drive micro-mirror.

3.2.2 Fabrication

The torsional electrostatic comb-drive mirror is fabricated by a three mask process outlined in Figure 3.13. First the wafer is oxidized to create a 2μm thick silicon dioxide layer. The pattern for fixed comb fingers is etched into the oxide and then deep (approximately 100μm) into the silicon by Deep Reactive Ion Etching (DRIE). Then a second wafer with an oxide coating layer is bonded to the first wafer. The second wafer is polished until the silicon device layer is roughly 50μm thick. Another oxidation step occurs on the bonded wafers to create a 1μm thick oxide layer.

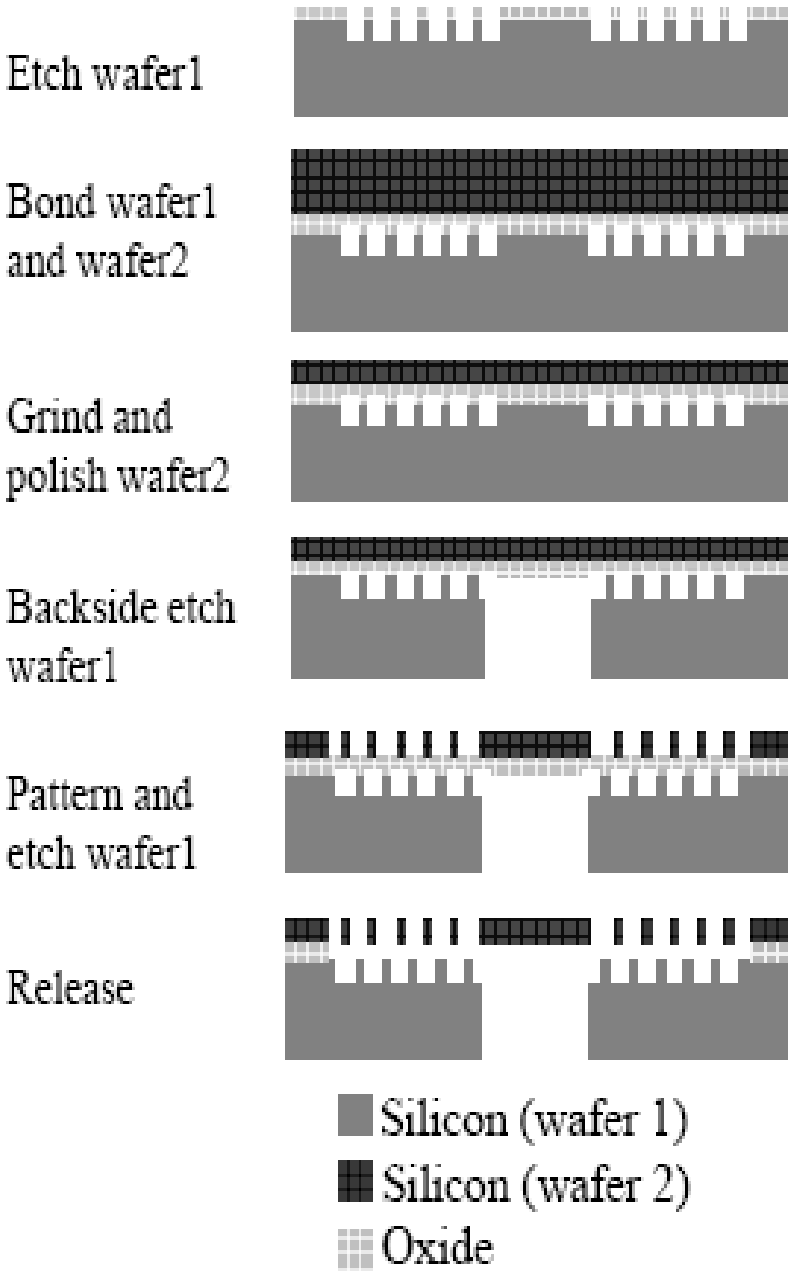

Figure 3.13: Fabrication flow for vertical comb drive scanners.

Now the upper layer is patterned with careful alignment (typical errors should be less than .5μm) to the buried, fixed comb drives, and the pattern is extended into the top oxide layer. Next a deep backside etch opens a hole to the mirror. Then another DRIE silicon etch on the front side defines the movable comb teeth. A timed chemical etch of the buried oxide layer by HF releases the mirror and movable comb-teeth. Finally the wafer is metalized with a 100nm film of gold to increase the reflectivity of the mirror to over 90%. Further specifications of this fabrication process at the Berkeley Microlab are contained in Appendix B.

3.2.3 Performance of System

Figure 3.14 shows the experiment that was performed with this system. Light is collimated onto the scanning micro-mirror which can position the reflected light onto different input waveguides to an AWG.

The scanned light was coupled into polished waveguide faces on an AWG supplied by ANDevices. The AWG was not a cyclic AWG, but had multiple inputs to compensate for any process inconsistencies by allowing multiple inputs closely spaced in the frequency domain. The input that put the device on the desired ITU grid would be used once the device was tested. An image of the device is shown in Figure 3.15. This is another out-of-spec test device similar to the one for the fiber actuator test. It is also a 40-channel silica-on-silicon AWG.

Light from a tunable solid state laser source is collimated by a Graded Index (GRIN) lens pig-tailed to a single mode fiber. The collimated spot size is 200μm. The collimated light beam is reflected off the scanning mirror and onto the polished facets of the input waveguides. The waveguides are square buried channel configurations of width 8μm and the channels are separated by a pitch of 128μm

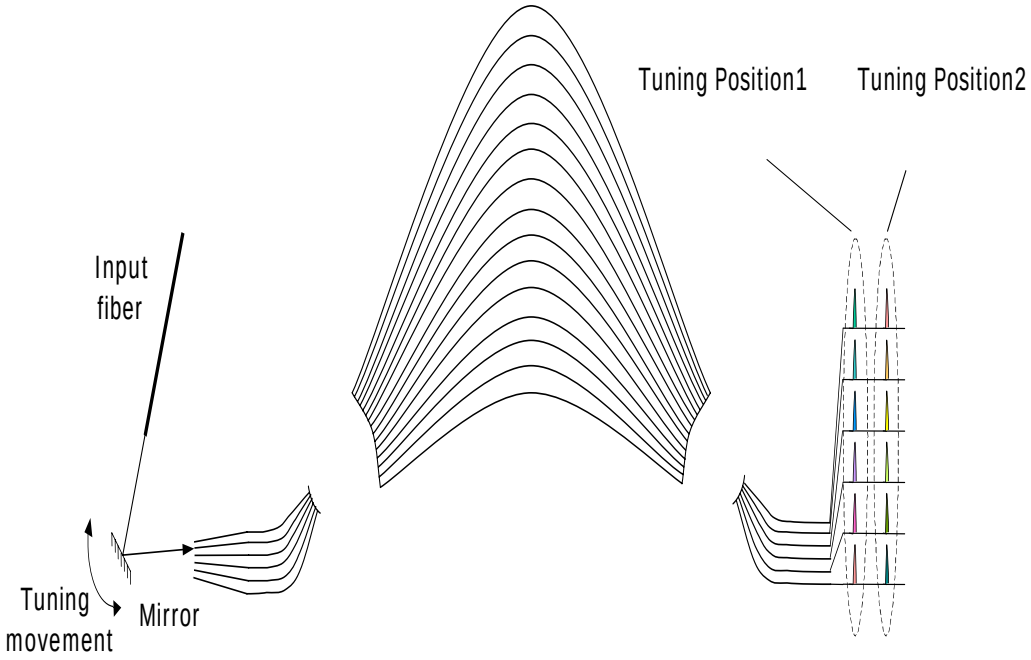

Figure 3.14: Schematic of OADM tests with scanning mirror.

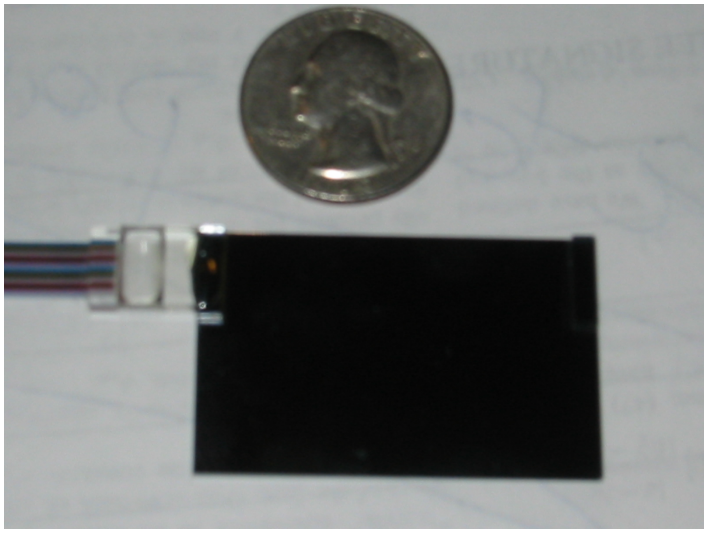

Figure 3.15: Photograph of the AWG used in the scanner experiments.

to allow for the dimensions of single mode fiber. Switching between the different input waveguides was achieved by adjusting the bias to the scanner. Figure 3.16 shows the tuned output of two output channels for a switch between the outermost input waveguides with an actuation voltage of 50V.

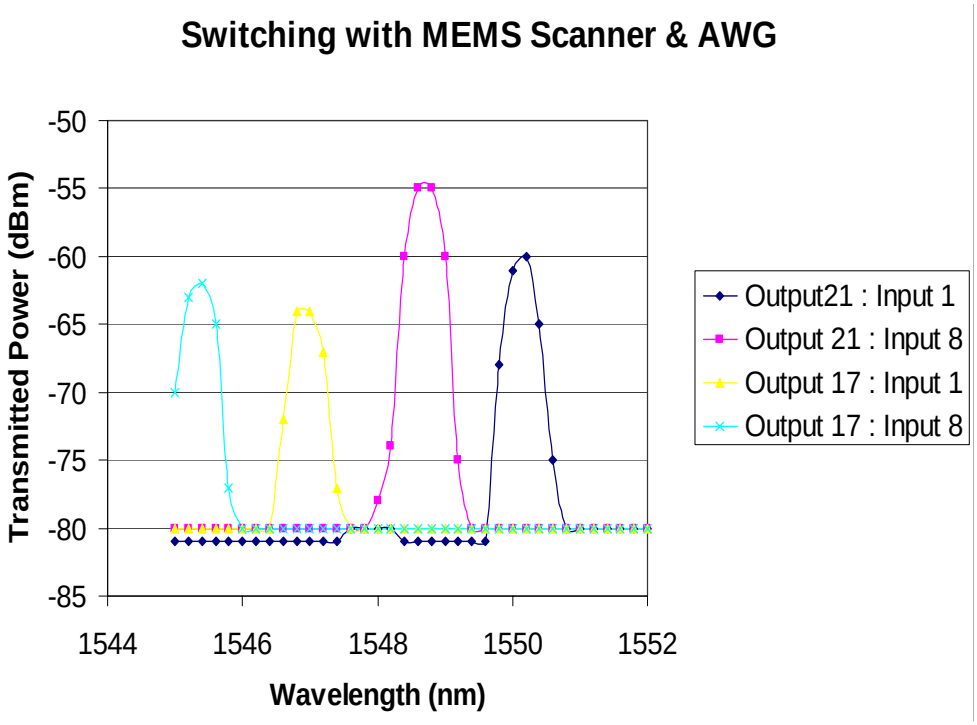

Figure 3.16: OADM system performance with scanning micro-mirror. Results of switching between the outermost input channels with measurements of the maximum output peak for two different output channels.

3.2.4 Conclusions

The scanning mirror provides more than sufficient lateral scan to achieve any necessary input displacement. However, by operating with free-space optical signals

the spot size becomes so large that little power is coupled into the waveguides and crosstalk becomes much stronger since the spot size is large enough to fall on multiple inputs at once.

Improvements could be made by specifically designing a special AWG for this application, but the inclusion of some focusing optics will be necessary to keep the system from being too lossy. Some appropriate types of optics have been proposed for other projects [51]. Focusing with aligned GRIN lenses is definitely possible, but increases the complexity of the system. Finally, integration is impossible since the scanner is on a wafer that must be arranged orthogonally to the wafer on which the AWG has been fabricated.

3.3 Binary Mirror Actuator Array

While the desired performance for the OADM was achievable in the setups previously described the collective difficulty of assembly and impossibility of higher level integration led to a search for a different type of actuator. Based on work previously done within the research group by Dr. Kunnavakkam, an array of binary, lateral mirror actuators is proposed [52] [53]. The theory, design, fabrication, and performance are all explained or reported below along with the scheme for single package integration with an AWG.

3.3.1 Theory & Design

Spring Design

For lateral actuators there are three types of spring suspension: fixed-fixed, crab leg, and folded flexure (shown in Figure 3.17). It has been shown that for large

lateral displacement actuators the best spring choice is the folded flexure [54]. Assuming no residual stresses in the springs and that the trusses are rigid, the spring constant for lateral deflection of the folded flexure is given by:

$$k_x = \frac{200EI}{3L\delta^2}, \tag{3.7}$$

where E is Young's Modulus of the material, I is the second moment of inertia, L is the length of legs, and δ is the deflection of the beam.

Lateral Comb Drive Actuators

The lateral actuator will be driven by an electrostatic comb drive, which consists of a collection of interdigitated fingers which are alternatingly fixed or movable (released). These combs are similar to the vertical comb drives described in the previous section, but instead of a vertical offset between the movable and stationary fingers they are co-planar. Figure 3.18 shows a single cell of this comb drive.

Ignoring fringing fields the capacitance between the fixed and movable comb sets is

$$C = \frac{2n\epsilon_0 h(x + x_0)}{d}, \tag{3.8}$$

where n is the number of fingers, ϵ_0 is the dielectric constant in air, h is the height of the comb fingers, x_0 is the initial comb finger overlap, y is the comb displacement, and d is the gap spacing between the fingers. From the capacitance the lateral, electromagnetic force between the movable and stationary bank of combs is

$$F = \frac{n\epsilon_0 h}{d} V^2 \tag{3.9}$$

where V is the applied actuation voltage between movable and stationary comb banks.

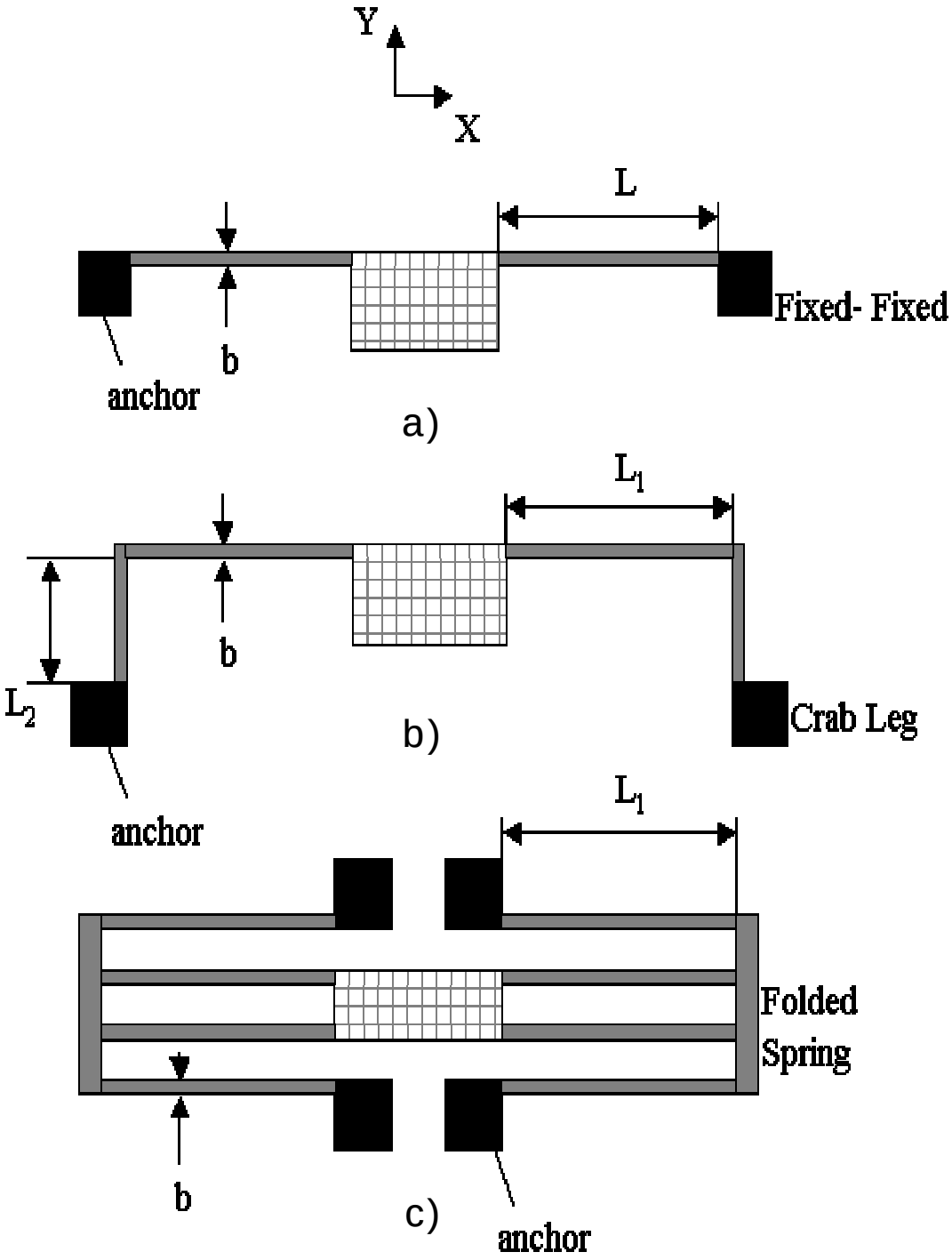

Figure 3.17: Examples of the three types of spring suspensions: a. fixed-fixed, b. crab leg, and c. folded flexure.

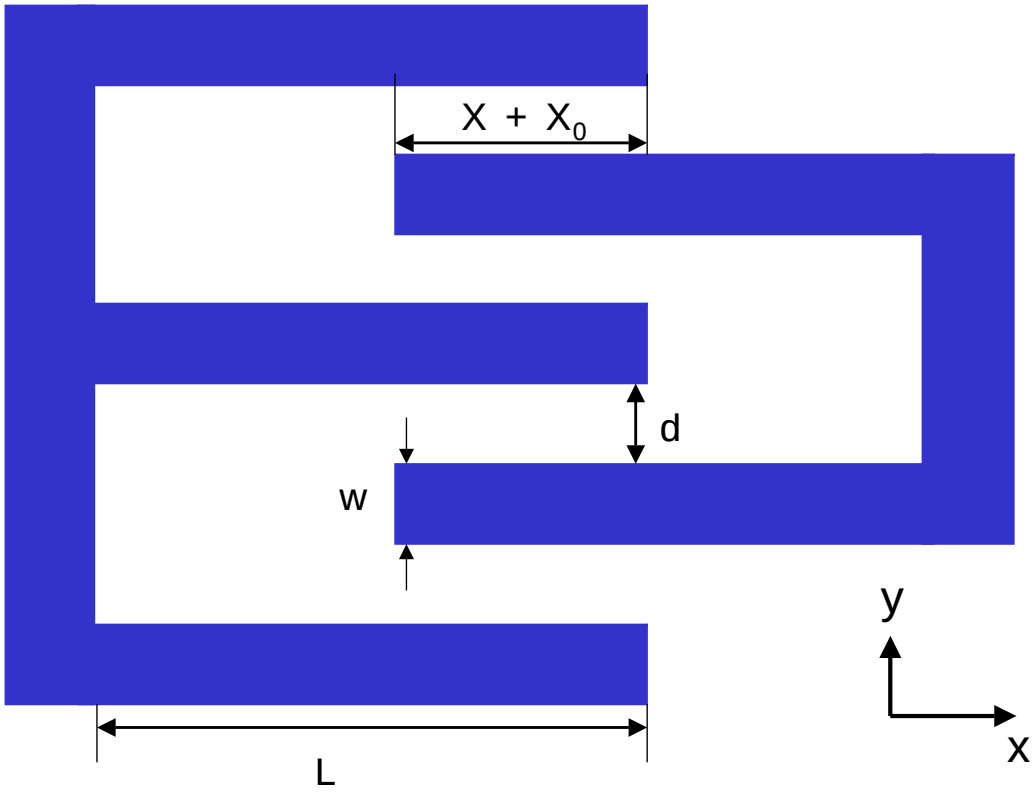

Figure 3.18: Elemental cell of lateral comb drive actuator.

Assuming operation in the range of a linear spring constant (k) this means the deflection caused by an applied voltage difference V is given by

$$x = \frac{n\epsilon_0 h}{kd} V^2. \tag{3.10}$$

In addition to the force pulling the fingers along the desired direction of motion (the x axis), there are also electrostatic forces pulling the fingers together causing a side instability. The maximum stable deflection can be shown to be [54]

$$x_{max} = d\sqrt{\frac{k_y}{2k_x}} - \frac{x_0}{2} \tag{3.11}$$

where a distinction is made between the spring constant in the direction of motion k_x and the orthogonal direction k_y. The ratio of k_y to k_x is $(L/b)^2$ so for long, thin springs the maximum deflection can be large and stable.

To achieve the reconfigurable aspect of the OADM this system is intended to be operated statically and not limited to any particular resonance frequency. Therefore information concerning the dynamic behavior of this spring and comb drive actuator system are not considered here. The resonant frequencies of the devices are on the order of a few kHz and far away from the operating frequencies.

An array of four 45^o mirrors was designed to create a 1x4 switch, Figure 3.19. The mirrors were spaced with a pitch of 128μm to correspond to the spacing of the input waveguides of the AWG from ANDevices. The vertical sidewall mirrors were designed to have a optical face that is 30μm tall in size, and the spring and actuators were designed to more the full 30μm range to move a mirror completely out of the way of its neighbors with a 30μmrange and an actuation voltage of 10V. The appropriate dimensions for the various elements are listed in Table 3.3.1.

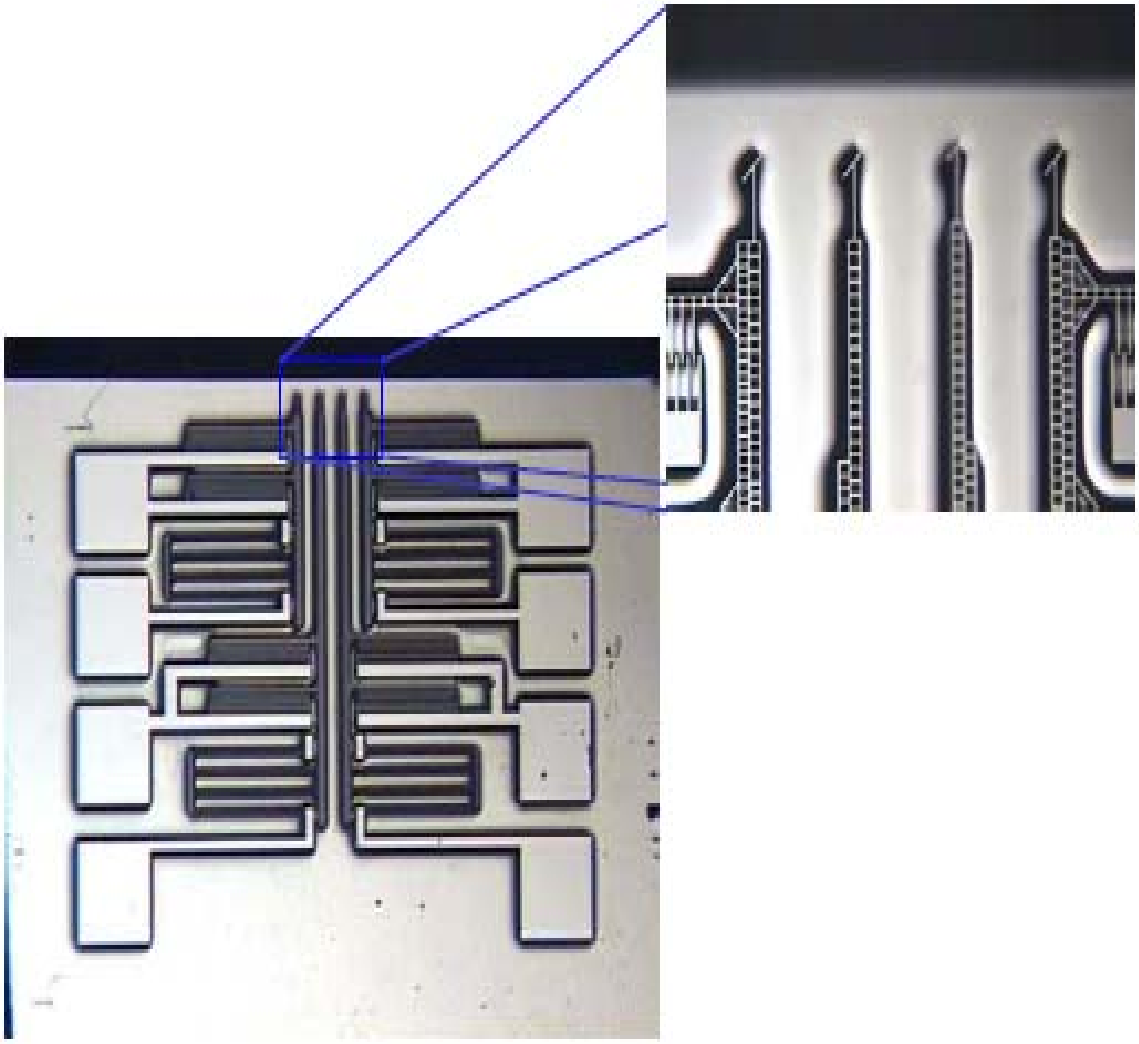

Figure 3.19: Image of fabricated 1x4 switch from binary lateral actuators. The 45^o mirror faces are shown further magnified.

Table 3.1: Dimensions of various elements of the binary actuator

Feature	**Specification**
Spring Length	683μm
Spring Width	2μm
Comb teeth	120
Length of combs	50μm
Initial comb overlap	6μm
Gap between combs	4μm
Comb teeth and spring thickness	40μm

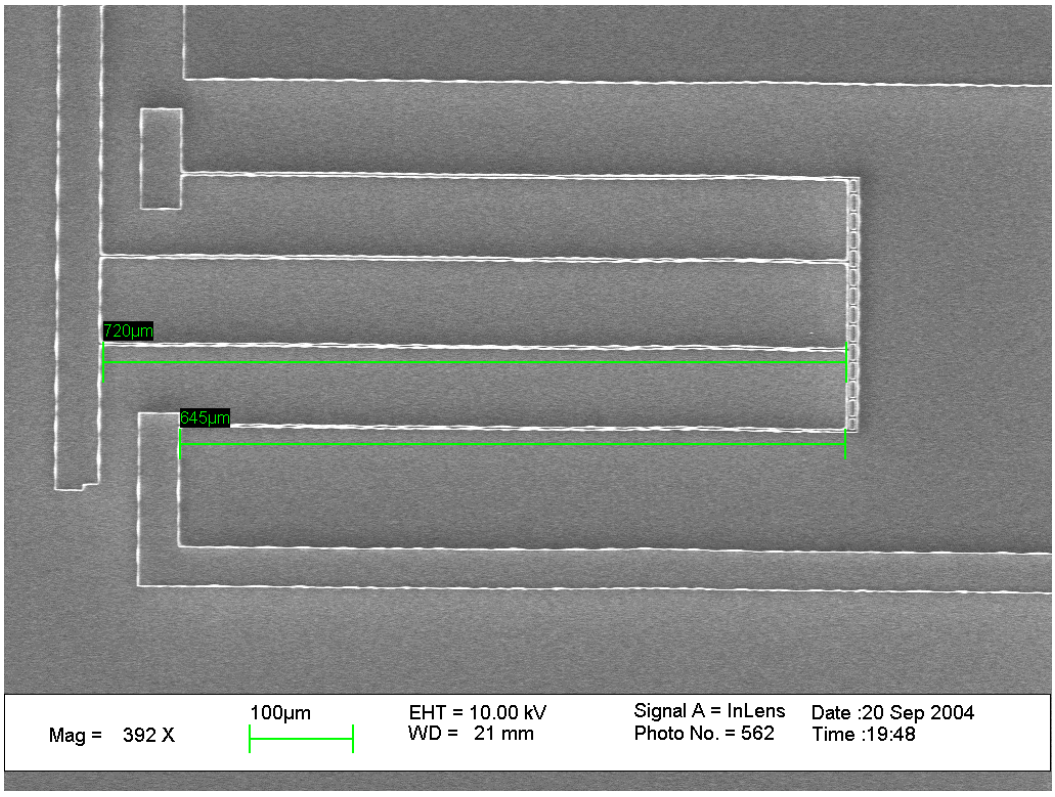

Figure 3.20: SEM of spring for mirror array.

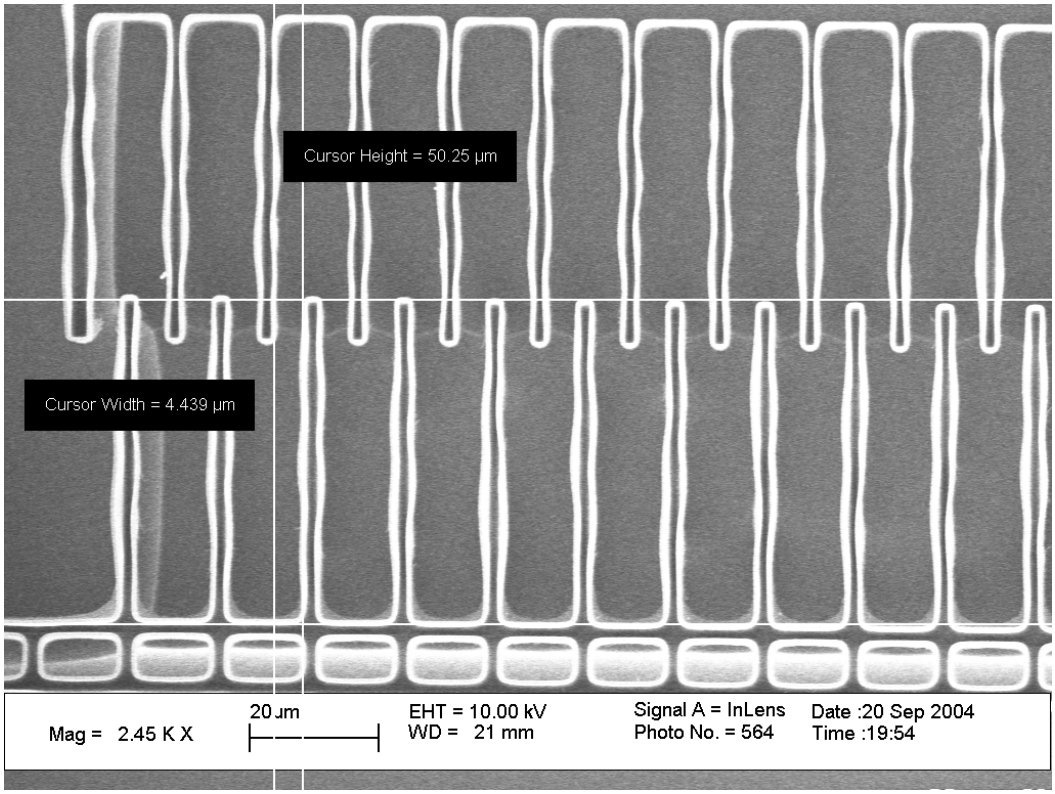

Figure 3.21: SEM of comb drive for mirror array showing finger spacing and length.

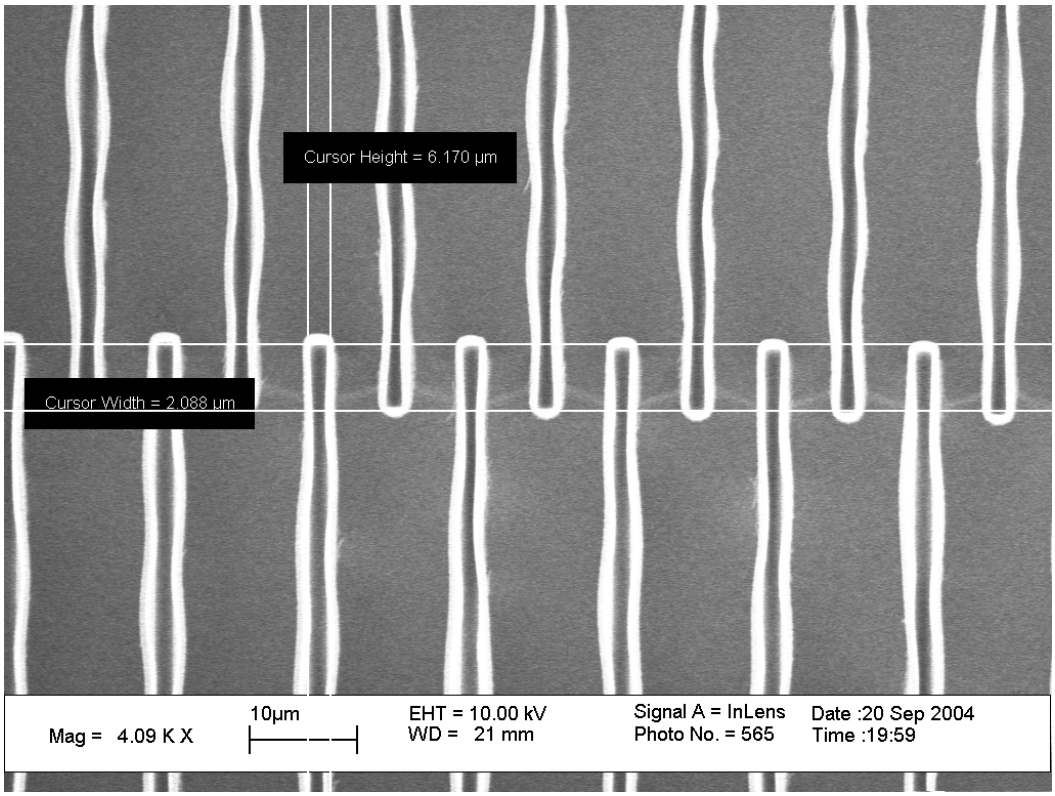

Figure 3.22: SEM of comb drive for mirror array showing finger thickness and overlap.

3.3.2 Fabrication

To ensure the comb fingers generate the desired actuation forces for this design the device layer thicknesses must be on the order of tens of microns. This cannot be easily achieved by surface micromachining techniques, thus a bulk micromachining approach was utilized. The SCREAM bulk micromachining process [55] [56] was chosen in particular because of familiarity within the research team with this procedure for making exactly these types of devices.

The Single Crystal Reactive Etch And Metalization (SCREAM) process allows a single mask fabrication technique for tall mechanical structures. Additionally, the SCREAM process does not require any wet chemical etching to release the structure which eliminates stiction problems caused by the capillary forces of the liquid phase etchant. The process is pictographically outlined in Figure 3.23. Beginning with a single crystal silicon wafer, an oxide layer is grown over the whole wafer. This oxide layer is used both to allow pattern transfer deep into the silicon and as an electrical isolation layer between the silicon and the top layer metal to be deposited later. The key is to have oxide thick enough to allow all necessary processing but not so thick as to cause damaging levels of stress to the devices.

The wafer is patterned using photolithography and the pattern is transferred first into the oxide and then into the silicon by Deep Reactive Ion Etching (DRIE). DRIE of silicon is not always particularly selective compared to the etching of photoresist so the oxide must stand up as a "hard mask" for the silicon to ensure the desired etch depth is attained.

Next a protective sidewall oxide is deposited. This ensures that electrical isolation between the metal to be deposited and the silicon substrate on the vertical sidewalls created by the deep etch. If the oxide is deposited conformally it is not

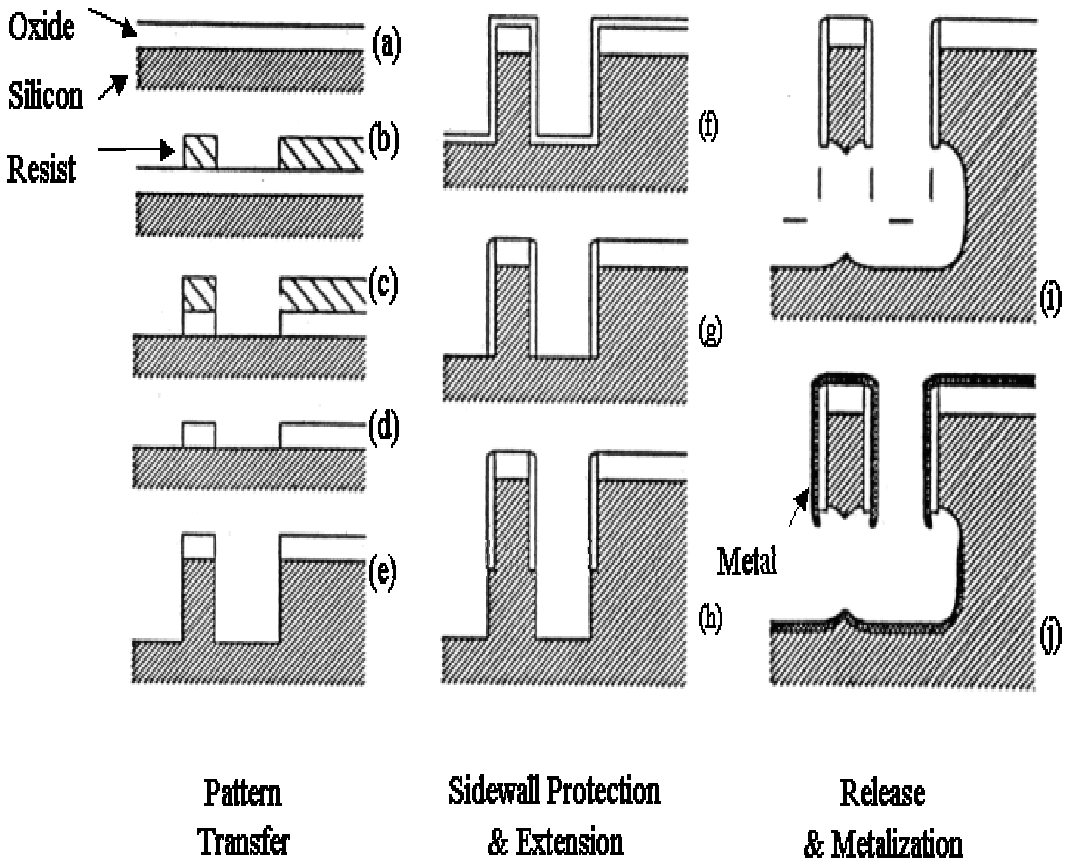

Figure 3.23: Process flow for SCREAM.

a disadvantage because having additional oxide on top of the structure or in the trenches will not limit the device. Another RIE of oxide now occurs with the intention of etching the oxide at the bottom of the trenches away. To ensure a vertical etch in which the trench bottoms and top plane of oxide are etched without significantly etching the sidewall oxide a high bias voltage for the RIE must be used.

Another silicon DRIE step extends the trenches downward exposing some bare silicon sidewalls. This step is to aid in the release of the movable structures from the substrate. The release etch is another DRIE plasma etch but should be isotropic to ensure significant lateral etching to undercut and release the thin structures.

Finally, a thin layer (approximately .1μm) of metal, typically Aluminum or Gold, is deposited for electrical contact, for the electromagnetic forces between the comb drives, and to provide a more reflective surface from the sidewalls, which will become the mirror faces for this device.

The SCREAM process was developed at Cornell University and was particularly effective within the Cornell Nanofabrication Facility because the specific tools necessary for that process where well tuned and characterized for proper performance. The binary arrays fabricated in this research project were made in the Berkeley Microlab. Thus the process needed to be tuned to the equipment available there. A detailed description of the specific tools and process conditions used is given in Appendix C.

3.3.3 Testing Performance

The binary actuator array operated at full 30μm displacement at 9V. Reflectivity from the metalized side-wall mirrors was measured at 82%.

For testing with the AWG, a commercial binary switch array was fiber coupled directly a cyclic 40-channel 100GHz spaced AWG from ANDevices. The source was a solid state tunable laser, which was fiber coupled into the binary switch array. By switching the inputs the cyclic switching of the output ports was observed, Figure 3.24. Additionally, the transmission spectra of various input ports to a particular output port was recorded to determine cross-talk levels, Figure 3.25.

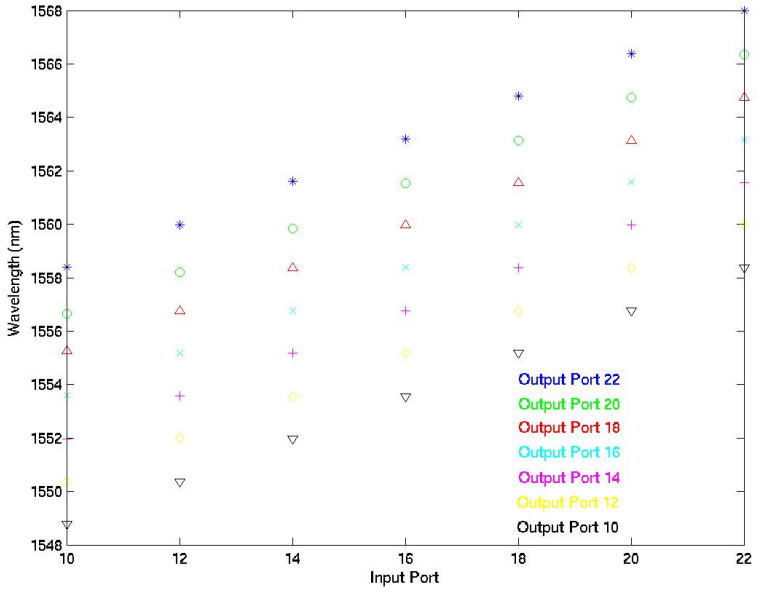

Figure 3.24: Binary Array OADM cyclic switching performance.

Clearly this device has the best success in terms of creating the performance required of an OADM. Additionally, the device designed can be integrated into a single package system with an AWG, as will be described in the next section.

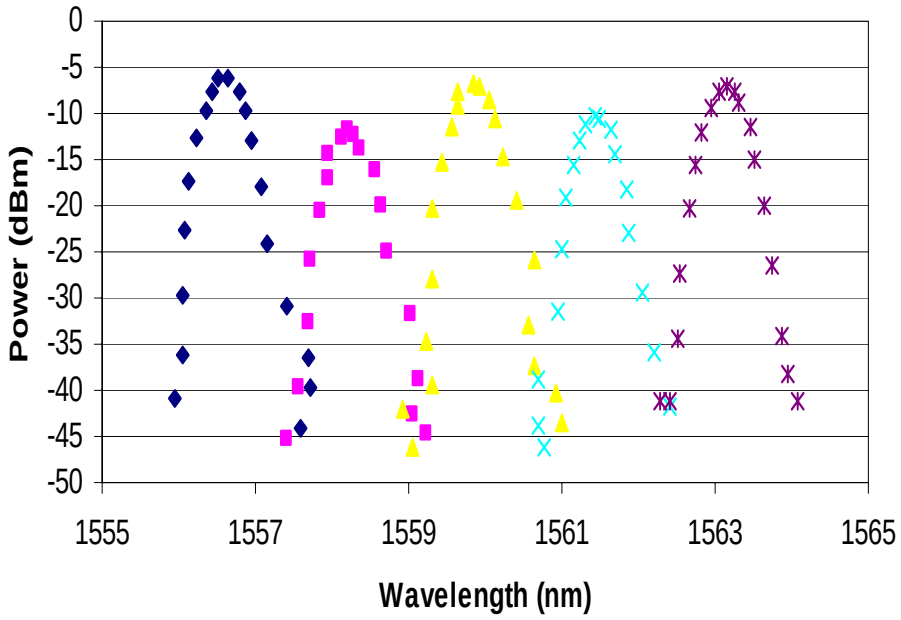

Figure 3.25: Binary Array OADM cyclic transmission spectra performance.

3.3.4 Extension to Integrated System

A hybrid design of the full OADM system can be implemented by fabricating the MEMS binary actuator array and AWG separately and then flip-chip bonding the devices together as shown in the process flow of Figure 3.26. With this method the difficulty of aligning separate chips to within a few microns (the thickness of the waveguides) can be handled by fabrication equipment that can repeatedly align devices to within a $2-3\mu$m. The height/depth dimension is even more precisely controlled by the deposition times of the CVD processes required to make the AWG and the timed etches of the MEMS devices.

The SCREAM-like, lateral actuator designed and fabricated for this project operates extremely well in optical index matching fluid. The coupling loss from a waveguide into index matching fluid reflected off a sidewall mirror back into

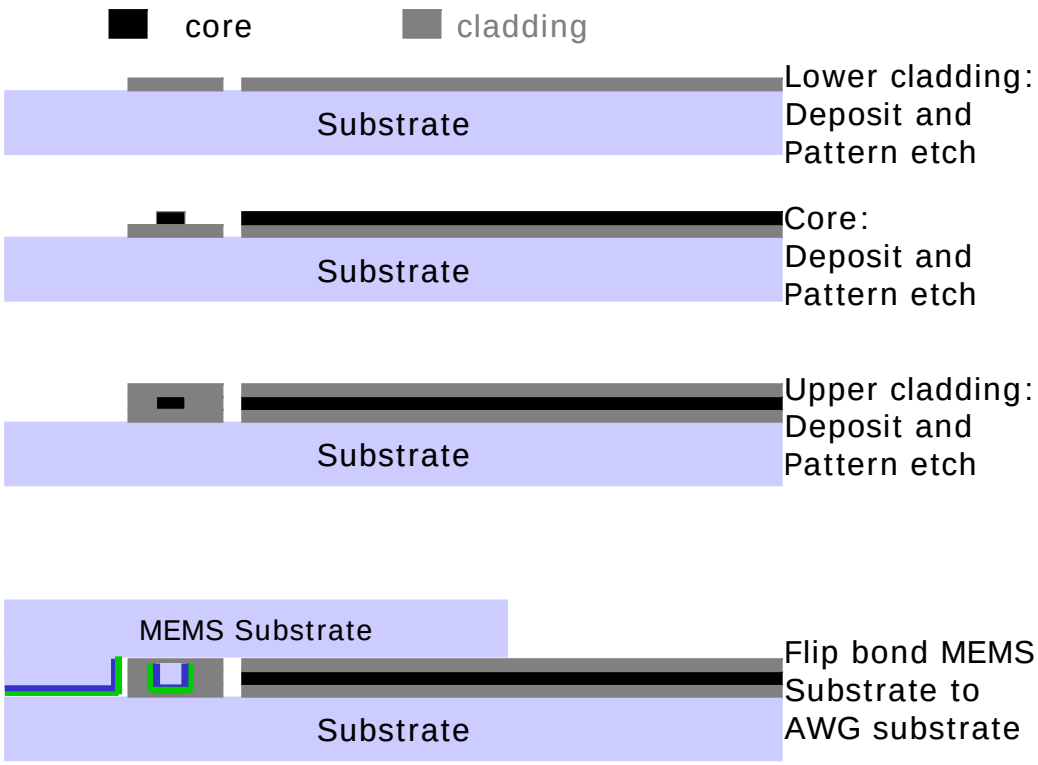

Figure 3.26: Process flow for integration of AWG and MEMS switch array for single package OADM. The AWG and MEMS switch array are fabricated separately then flip chip bonded together. A schematic of the MEMS process flow can be seen in Figure 3.23

a waveguide has been simulated to be less than .5dB. This is a consideration for scalability to more densely multiplexed systems because the n^{th} channel will experience loss of $(n-1) \times .5dB$ compared to the first channel. Compensation for these inter-channel losses will need to be managed.

3.4 Conclusions & Future Work

The integrable system shown here elegantly utilizes a single AWG to achieve full reconfigurability of an OADM with 1xN MEMS binary switch array. In this way the scalability and complexity issues of the various multi-AWG designs have been solved. The MEMS switch array has a simple and inexpensive fabrication process that can be completed separately from the AWG fabrication. By maintaining the light in waveguides as much as possible in the design power management is optimized and extraneous cross-talk is minimized. And a fully integrated, single-package, compact system is realizable.

The obvious next step is to attempt the flip-chip bonded integration of the MEMS switch array with an AWG. Unfortunately, the ugly specter of economics halted this part of the project before it was able to come to completion. The full cost of designing and fabricating an original run of AWGs is expensive and with the optical telecom bubble bursting, ANDevices was understandably reluctant to devote money and time to a research project when attempting to survive.

It was not possible to purchase a designer run of AWGs and this project was left at the design stage.

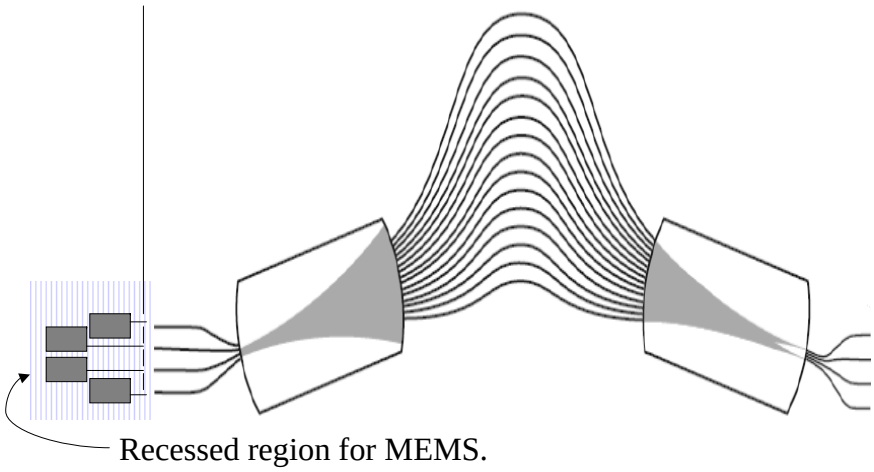

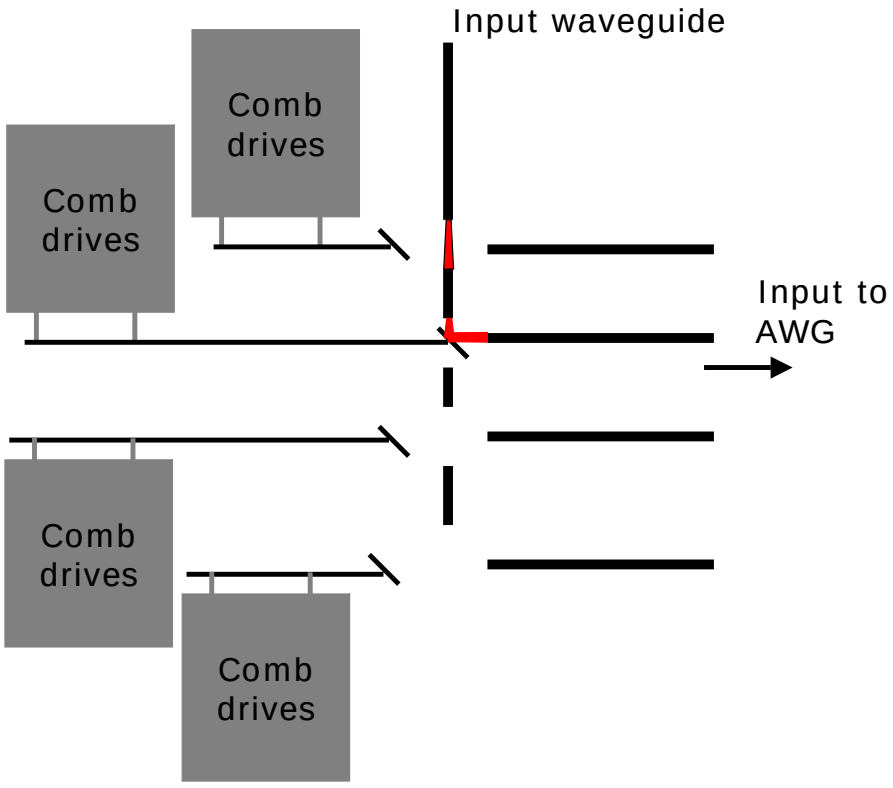

Figure 3.27: (Top) Top view of integration plan. (Bottom) Close up of MEMS switch region.

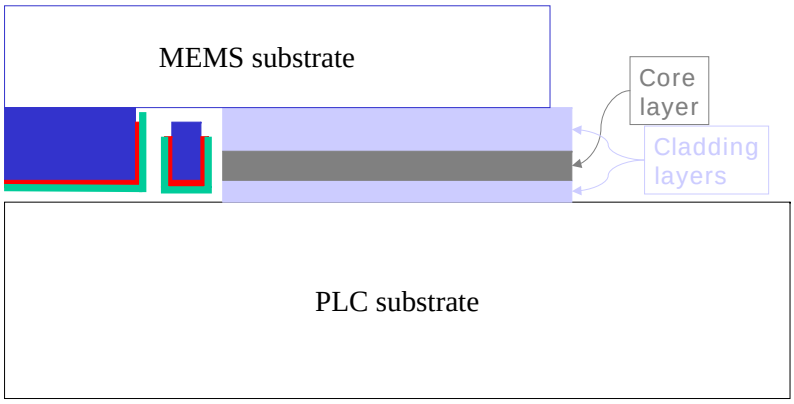

Figure 3.28: Side view of integration plan, showing the MEMS chip flipped and bonded into the pre-etched recessed region of the PLC substrate.

CHAPTER 4

THE PHYSICS OF INFRA-RED GAS DETECTION

In this chapter, a description of the physics behind infrared (IR) gas detection will be provided. To analyze the situation, the interaction of light with diatomic molecules will be studied. To get an order of magnitude calculation of the energies of modes of a simple diatomic molecule, the binding force of the molecule will be approximated by a square well. That analysis will be extended by considering the more accurate representation of the binding force as a simple harmonic oscillator, Figure 4.1. Finally, a brief description of the differences between the predictions of this simplified model and the actual behavior will be presented.

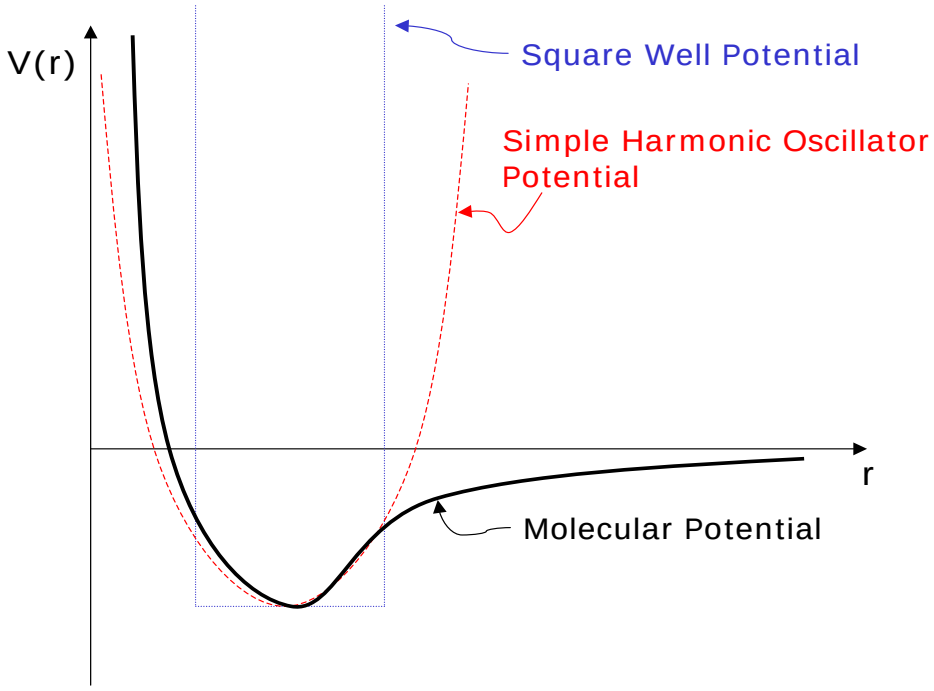

Figure 4.1: A representation of a molecular potential and the square wave and simple harmonic oscillator approximations to that potential as functions of the nucleic separation.

The strategies developed concerning diatomic molecules can be extended to polyatomic molecules. With this basic framework, it will be shown that certain very general types of molecules are absorbent in the IR range of electromagnetic radiation in repeatable and unique ways. This characteristic allows for detection and characterization of the molecules from their absorption spectra.

4.1 Diatomic Molecules

4.1.1 Diatomic Molecular Model

Consider the simple "dumbbell," or rigid-rotor, model of a diatomic molecule. The mass of the molecule is confined to the spherical nuclei of the constituent atoms. The nuclei are separated by some distance, and held together by an atomic bond, see Figure 4.2. The molecule can have vibrational modes of stretching and compressing along the axis of the bond and orthogonal rotational modes about an axis perpendicular to the bond axis through the molecules center of mass [57].

4.1.2 Rotational modes

Consider only the rotational motion of the system and treat the bond as a rigid massless bar joining the two atoms. The moment of inertia I for our dumbbell model is given by

$$I = m_1 r_1 + m_2 r_2 = \frac{m_1 m_2}{m_1 + m_2} r_0^2 = \mu r_0^2 \tag{4.1}$$

where μ is the reduced mass of the system, and r_0 is the inter-atomic distance. The energy of rotation for a diatomic molecule is given by

$$E = \frac{L^2}{2I} \tag{4.2}$$

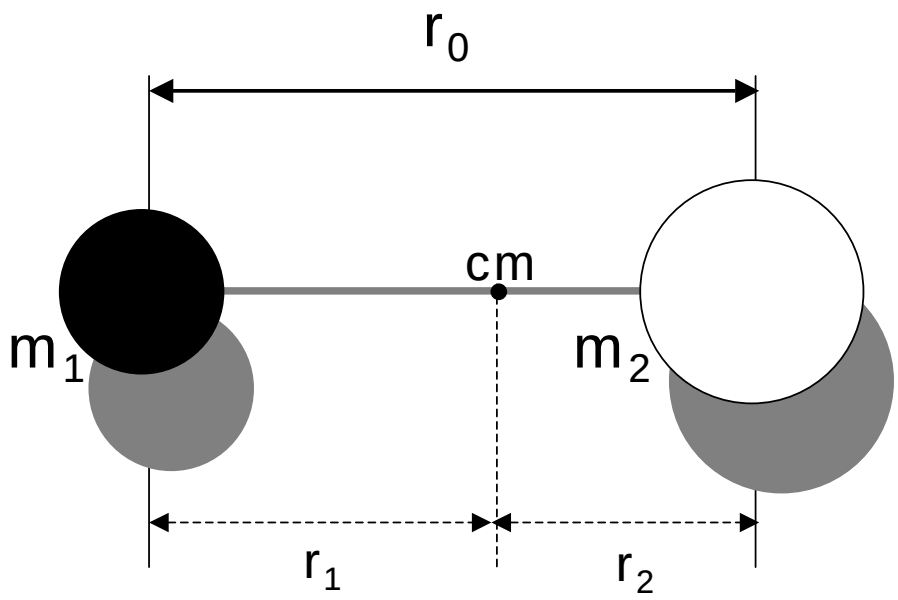

Figure 4.2: A simple, but accurate, model of the diatomic molecule as a rigid-rotor. The mass is confined to the two spherical nuclei (masses m_1 and m_2, respectively) separated by distance r_0 to approximate the bond. The center of mass of the molecule is marked by **cm** and the distance of each atom to the center of mass is r_1 and r_2, respectively.

where L is the angular momentum.

The Schrödinger equation provides the eigenvalues of L^2 for the rigid rotor model [58]:

$$L^2 = l(l+1)\hbar^2 \tag{4.3}$$

where l is a non-negative integer, and $\hbar$ is Planck's constant. This gives the eigen-energies

$$E = \frac{l(l+1)\hbar^2}{2I} = \frac{l(l+1)\hbar^2}{2\mu r_0^2}. \tag{4.4}$$

From known values of the rest mass of protons and neutrons and bond lengths for diatomic molecules, calculation of the values for the eigen-energies are on the order of $l(l+1) \times 10^{-3} eV$. This implies light wavelengths of rotational mode energies are on the order of

$$\lambda = \frac{hc}{E} = \frac{1}{l(l+1)} 1.2 \times 10^3 \mu\text{m} \tag{4.5}$$

which yields photons in the far infrared region. However, it is the transitional energy levels that contain the interesting phenomena for spectroscopy.

4.1.3 Vibrational modes

The vibrational states can be considered like a particle in a bounding potential. The solution to the actual potential shown in Figure 4.1 is difficult to solve, but some important characteristics can be learned from approximating the binding potential with easier to solve functions.

Square well potential approximation

If the binding potential is approximated with a square well potential function, then the traditional energy levels from a particle in a box is valid [59]:

$$E_n = n^2 \frac{\hbar^2 \pi^2}{2\mu r_0^2}, \tag{4.6}$$

with n an non-negative integer and $\hbar$ is Planck's constant. The first thing to notice is that this is on the same order as the rotational eigen-energies shown in Equation 4.4. Next, note that the energy levels are large compared to kT at room temperature (300^oK), so that in atmospheric or room temperature environmental systems the molecule can be assumed to be in the lowest few energies states ($n = 0$ or $n = 1$).

Simple harmonic oscillator approximation

A better approximation to the molecular binding potential is to model the system as a simple harmonic oscillator (SHO). For low energies the SHO approximation fits the actual binding potential very well. The quantum mechanical energy levels for a SHO are

$$E_n = \hbar\omega(n + \frac{1}{2}). \tag{4.7}$$

The value of ω is the classical angular frequency and would be empirically determined to provide the best fit to the actual molecular binding potential. Badger [60] and Gordy [61] provide methods for determining this fit from the electro-negativity and other compound specific parameters.

4.1.4 Vibration-rotation modes

The vibrational and rotational modes can be superimposed to form a vibration-rotation energy diagram like that shown in Figure 4.3. At room temperature the vibrational energies are much higher than kT and can be considered to be at the lowest level. At low energy, the actual energy levels fit the SHO model well, which means energy transitions of $\Delta n = \pm 1$ are possible.

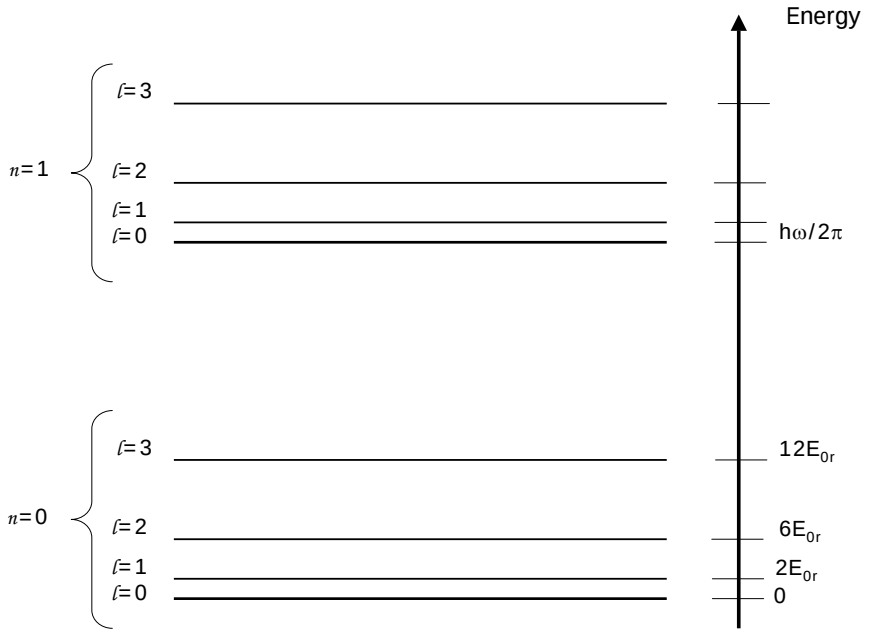

Figure 4.3: Representation of the vibrational and rotational energy states of a diatomic molecule with the the SHO approximation to the binding potential. $E_{0r} = \frac{\hbar^2}{2I}$ is the $l = 0$ rotational energy level.

Although absorption is dominated by the $n = 0 \rightarrow n = 1$ vibrational transition, the rotational energies are sufficiently less than kT to allow a distribution of rotational energy states. Electrical dipole rotational transitions obey the selection rule $\Delta l = \pm 1$ [62]. With these selection rules, the energies of transitions can be

approximated.

For $n = 0$ the vibrational-rotational energy for the l^{th} rotational state is given by

$$E_l = \frac{1}{2}\hbar\omega + l(l+1)E_{0r} \tag{4.8}$$

where $E_{0r} = \frac{\hbar^2}{2I}$ is the $l = 0$ rotational energy level. The final energy for a transition to the $(l+1)^{th}$ state is

$$E_{l+1} = \frac{3}{2}\hbar\omega + (l+1)(l+2)E_{0r}. \tag{4.9}$$

Likewise, the final energy for a transition to the $(l-1)^{th}$ state is

$$E_{l-1} = \frac{3}{2}\hbar\omega + (l-1)E_{0r}. \tag{4.10}$$

So the energy differences are

$$\Delta E_{l\to l+1} = \hbar\omega + 2(l+1)E_{0r} \qquad l = 0, 1, 2\ldots \tag{4.11}$$

$$\Delta E_{l\to l-1} = \hbar\omega - 2E_{0r} \qquad l = 1, 2, 3\ldots. \tag{4.12}$$

So the absorption spectrum features frequencies equally spaced $\frac{2E_{0r}}{\hbar}$ apart, with a gap of $\frac{4E_{0r}}{\hbar}$ at the vibrational frequency ω due to forbidden transition at that energy. While the typical vibrational-rotational frequencies are on the order of a few microns, the difference between neighboring peaks is on the order of a dozen nanometers [63].

4.1.5 Discrepancy from approximations

At energies above the lowest states, the SHO approximation for a rigid-rotor begins to deviate more significantly from the actual potential. Instead of being evenly spaced the vibrational eigen-energies, become closer and closer together. This is

because the system is more loosely bound in actuality than predicted by SHO approximation. Also the $\Delta l = \pm 1$ rule no longer remains valid.

Nonrigid Rotor Model

The rigid-rotor model as presented calls for equal spacing of the energy state when $\Delta l = \pm 1$, but empirically there is a slight compression of the energy eigenstates for the $\Delta l = +1$ transition and a broadening for the $\Delta l = -1$ transitions. This can be understood by modifying the rigid rotor model to account for physical change in the molecule during a vibrational state change. This is known as the nonrigid rotor model.

Consider a diatomic molecule that has absorbed radiation to cause a transition to a higher energy vibrational state. After absorption, the molecule vibrates with a larger amplitude and has a larger inter-nuclear distance. This means the molecule now has a larger moment of inertia (Equation 4.1). Define the rotational constant R_ω using Equation 4.4 as

$$R_\omega = \frac{\hbar^2}{2I_\omega}. \tag{4.13}$$

The energy transitions can now be re-calculated as in Equations 4.11 and 4.12.

$$\Delta E_{l\to l+1} = \hbar\omega + 2R_\omega + (3R_\omega - R_{\omega_0})l + (R_\omega - R_{\omega_0})l^2 \qquad l = 0, 1, 2\ldots \tag{4.14}$$

$$\Delta E_{l\to l-1} = \hbar\omega - (R_\omega + R_{\omega_0})l + (R_\omega - R_{\omega_0})l^2 \qquad l = 1, 2, 3\ldots. \tag{4.15}$$

Since for an increase in vibrational frequency ($\omega > \omega_0$), and the subsequent increase in moment of inertia ($I_\omega > I_{\omega_0}$) there is a decrease in the rotational constant $R_\omega < R_{\omega_0}$. This shows that for the $\Delta l = +1$ transitions the energy spacings decrease for increasing l, and for $\Delta l = -1$ transitions the energy spacings increase for increasing l.

Anharmonic Oscillator Model

While the SHO model predicts that the vibrational energy levels will be evenly spaced, measurements on real systems show that the overtone bands appear at lower energies. Additional corrective terms are added to the vibrational eigen-energies to compensate for this affect. Terms are added in increasing powers of the quantum number n and empirically fit to the data.

4.2 Dipole Moments

If a molecule is to absorb infrared radiation, the radiation must be of the correct frequency to cause a quantum leap in its vibrational and/or rotational energy. A vibrating molecule will interact with electromagnetic radiation only if an oscillating dipole moment accompanies the vibration. A change in dipole moment occurs for a molecule whenever there is a change in position of the center of charge resulting from atomic motion.

4.3 Polyatomic Molecules

IR spectroscopy can be performed for polyatomic molecules with great success just like diatomic molecules. Individual bonds in complex molecules can be detected by IR spectroscopy based on their absorption. The theory describing the energy levels and transitional absorption is similar to that described above but is increasingly more complicated as more bonds are added.

Bond bending vibrational modes such as “waggle” and “rocking” motions are possible, in addition to linear vibrations of multiple bonds. Rotational modes are more difficult to calculate because of the overall moment of inertia becoming

increasingly complicated.

4.4 IR Absorption as a Gas Detection Mechanism

The theory behind electro-magnetic absorption at characteristic wavelengths by molecules has been presented. Now an explanation of how this specific absorption pattern of IR-active compounds allows for a gas sensing system.

Not every molecule is IR-active. In addition to being poly-atomic (required for vibrational modes), the molecules must have a dipole moment. This still leaves many interesting species (CH_4, N_2O, H_2O, CO_2, CO, and others) that are IR-active. Additionally, this means that the two molecules that form the vast majority of the earth's atmosphere, N_2 and O_2, are both IR-invisible. If white IR radiation is incumbent on a gas comprised of one or more of these IR-active species, the light at wavelengths of the transitions will be absorbed. By scanning the spectrum for absorption peaks and comparing to known absorption wavelengths for gaseous species, the presence of the species can be confirmed.

4.4.1 The Beer-Lambert Law

In addition to determining the presence of a molecule, IR spectroscopy can determine the concentration of gas present by reference to the Beer-Lambert law. The Beer-Lambert law [1] states that the absorption at a particular wavelength is given by

$$A_\lambda = \frac{I}{I_0} = e^{-k_\lambda cl} \tag{4.16}$$

where I is the intensity of light of wavelength λ after passing through the gas, I_0 is the original intensity of the light before passing through the gas, c is the

[1] Less commonly known as the Beer-Bouguer Law.

gas concentration, l is the path-length of the light in the gas sample, and k_λ is the empirically determined absorption constant of the gas at the wavelength in question.

The absorption constant k_λ for a gas species is defined specifically at a single wavelength. However, in practical detection systems the radiation incident on the material always has a spread of wavelengths. Therefore, at radiation centered around the maximum absorption wavelength the actual measurement is an average around that central wavelength weighted by both the absorption spectrum of the gas and the spectral bandwidth of the source [64].

Although precise absorption spectroscopy may be performed using cryogenically-cooled long-wavelength lasers, low-cost detection for industrial applications is usually accomplished through sensors referred to as non-dispersive IR (NDIR) sensors. A typical NDIR sensor consists of a filament lamp, one or more optical interference filters, and an infrared detector elements [65]. Narrowband absorption is measured by designing each interference filter to transmit only the waveband of interest [66].

NDIR systems are comprised of an IR radiation source, an IR detector, a gas sample cell, and a wavelength filter [67]. Traditional types of wavelength filters include gratings or prisms to select a particular wavelength and resolution. Often, the gas cell itself is used as the wavelength filter. A second reference cell is used to set the transmission baseline with which the sample gas transmission will be compared.

Another method of gas species detection is based on chemical sensors [68]. However, in comparison with solid-state chemical sensors, NDIR sensors have the advantages of highly selective response to a targeted gas or vapor, immunity to contamination (since they do not require contact with the measured species), and

long service lifetimes without need for sensor calibration. The main drawback of these sensors is that they consist of multiple discrete components, resulting in high cost ($50-$100) per measurement wavelength. A system that can provide measurements for multiple wavelengths with a single set of optics, source, and detector could be advantageous.

CHAPTER 5

MEMS BASED NDIR GAS DETECTION

This chapter describes the setup and performance of an NDIR system for gas detection and concentration measurement based on the theory from Chapter 4. The system utilizes a MEMS scanning mirror and a Linear Variable Filter as the wavelength selective element. Additionally, the system can be tuned over a range of wavelengths allowing the detection of multiple species.

5.1 The System

As described in the previous chapter, NDIR detectors can provide excellent gas identification and concentration measurements. NDIR systems are composed of an IR radiation source, an IR detector, and some method of selecting out a narrow waveband for measurement. Some systems use a single wavelength source tuned to the specific frequency of the species to be detected, while others utilize a narrow pass-band detector dedicated to proper wavelength. These types of systems are limited in that to detect multiple species, multiple narrow band sources or detectors must be used quickly increasing the size, complexity, and overall cost.

Another way to ensure the detection of multiple species is to allow for a changing wavelength selector. The system presented here follows this method. It also allows for the system to be small and inexpensive compared to other multiple wavelength detectors. The trade off for the small size and low cost is a limit on resolution. Individual rotational energy levels cannot be resolved as with a gas chromatograph or Fourier Transform InfraRed (FTIR) spectroscopy unit. However, for species identification and concentration measurements in the industrial range of a few hundred ppm to a few percent such precise resolution is not neces-

sary.

Figure 5.1 shows a schematic of the system proposed for a multiple wavelength NDIR gas detector. An inexpensive 500 mW broadband IR lamp was used as the optical source. The light from the lamp was focused using a parabolic mirror (not shown) onto a torsional comb-drive micro-mirror. This is the same scanning mirror used in the OADM system previously reported (see section 3.2). The mirror is computer controlled using a high-voltage amplifier. The IR beam is then collimated with a second parabolic mirror which acts to convert the rotating scan of the MEMS mirror into a translation of the collimated optical beam. A MEMS mirror was utilized as opposed to a macroscopic actuator to allow for future miniaturization of the system. As a result, the beam is laterally translated across a linear variable filter (LVF). An LVF is a passive optical device composed of a precisely controlled thin film thickness across its length. As the film thickness changes the passband wavelength for the film changes proportionally. By positioning the optical beam at different locations on the LVF, specific narrowband IR regions can be detected. The filtered light is then collected by a third parabolic mirror and focused onto a thermopile IR detector. The detector output is then amplified and digitized with a data acquisition system.

The entire system was assembled on a bench-top optical bread-board and then covered by a home-made gas containment box, shown in Figure 5.2. The gas box is divided into two sections, the test gas region which has a volume of 9L and a background region with a volume of about 100L. The background region is flooded with fabrication grade purity (99.999%) N_2 so as not to influence the measurements in the test gas region. The gas in the test region can be changed as desired using inlet and outlet gas nozzles. The reason for the separate sections of the box is to

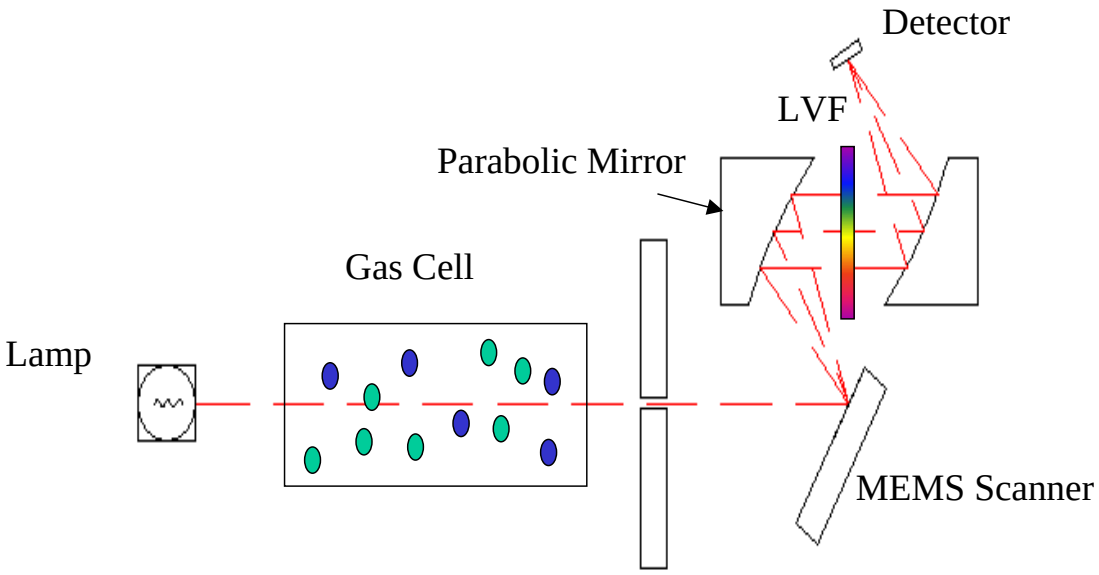

Figure 5.1: A design for an Non-Dispersive InfraRed gas sensor with a MEMS scanning mirror and an LVF.

limit the expense by requiring only small amounts of calibration gas to test the system. The two regions of the gas box have a 25mm diameter window that is IR transparent up to 10μm and is directly in the optical path.

5.2 The Components

This section will describe the elements of the system outlined in the last section in greater detail. Since the goal is the development of a low-cost multi-wavelength detector, attention will be paid to the cost of the elements and their effect on the overall size and performance of the system.

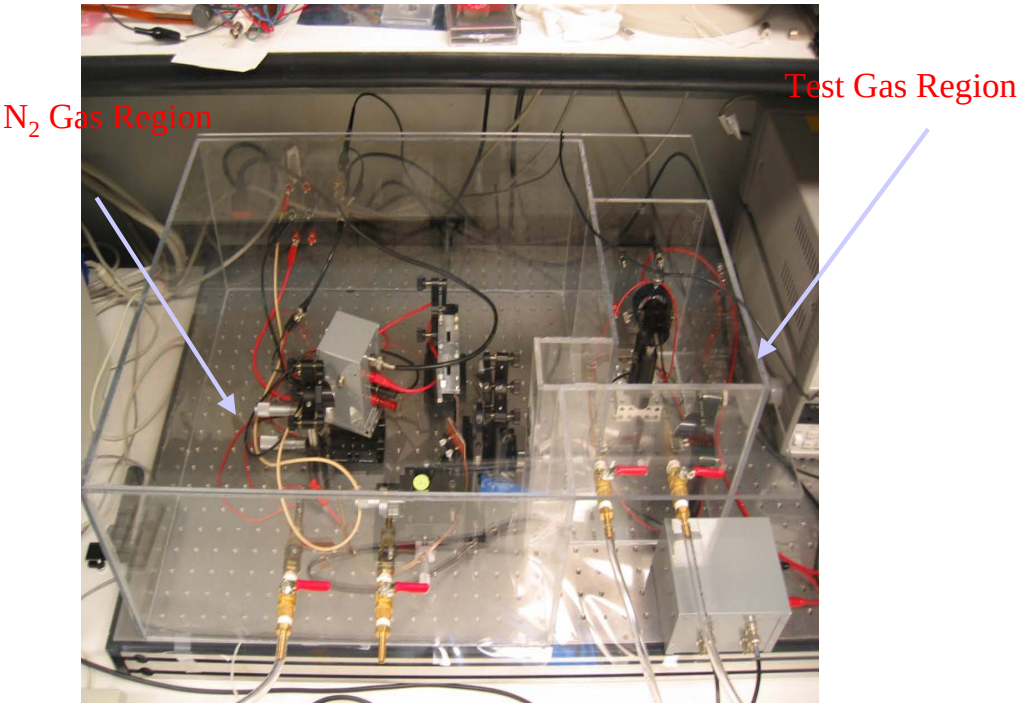

Figure 5.2: Image of testing setup with the gas containment box.

5.2.1 The Light Source

The light source is an inexpensive (< $5 each) broadband IR filament lamp. Specifically it is a Gilway MR4-188 lamp [69]. The lamp is rated up to 5W of power but was run at 500mW for these experiments. The output spectrum of the lamp is shown in Figure 5.3. Note that the transmission is monotonically decreasing as the wavelength increases.

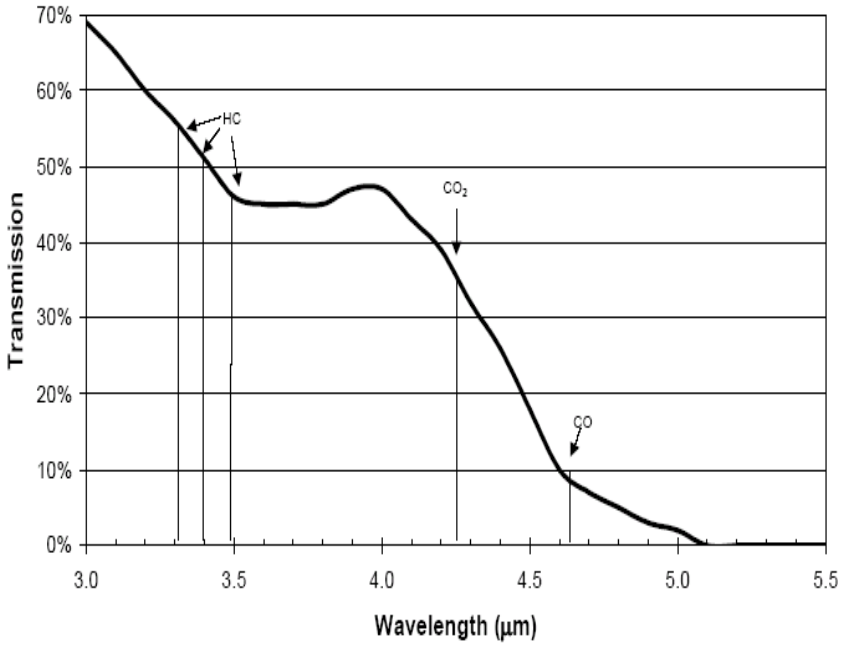

Figure 5.3: Output spectrum of the broadband source used in this experiment. Important bond absorption wavelengths are noted.

5.2.2 Parabolic Mirrors

The three focusing mirrors are all off-axis parabolic mirrors from Edmund Industrial Optics. Off-axis parabolic mirrors allow the various components to be placed close together without interrupting the beam path (Figure 5.4). The first one that

directs light from the source onto the mirror is a 90^o mirror with a 4in focal length. The other two mirrors are identical 60^o mirrors with a 1in focal length. Because of the tendency for glass to absorb mid-IR light, the mirrors have a reflective Aluminum layer as their topmost layer. Surface roughness for these mirrors is $< 175\mathring{A}$ RMS [70]. Each of these mirrors is on the order of $100.

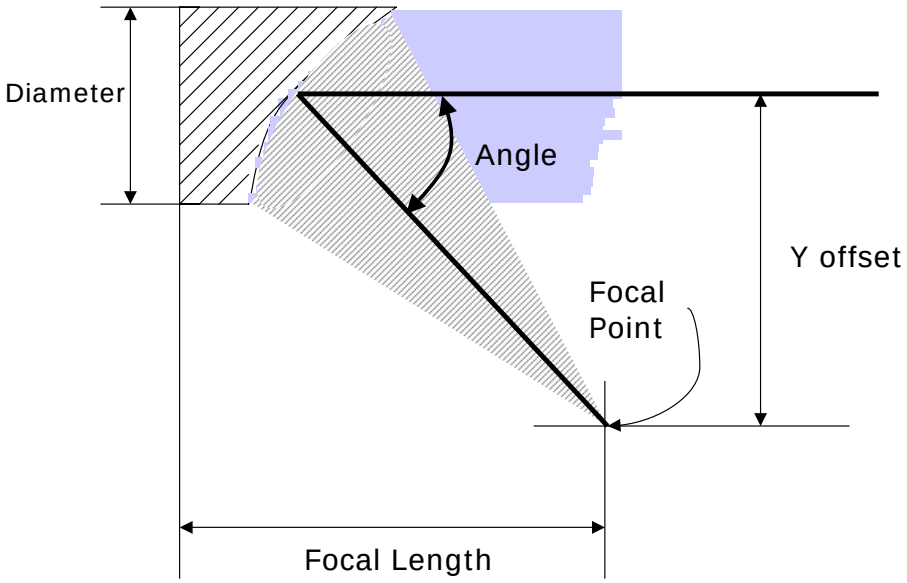

Figure 5.4: Schematic of an off-axis parabolic mirror.

5.2.3 Linear Variable Filter

The Linear Variable Filter [1] uses precisely controlled film thickness that is increased linearly along the length of the filter. For this project a narrow bandpass filter was desired. For this type of filter the thickness of thin film D is controlled by the equation

$$D = \frac{\lambda}{2n}, \tag{5.1}$$

[1] Also known as a wedge filter.

where n is the index of refraction of the film and λ is the center wavelength of the pass band.

The LVF was purchased off the shelf from Barr Associates (UK) and is the most expensive component in the system at a couple of hundred dollars. The LVF used is 15mm in length, with a wavelength range of $3.0 - 5.0\mu$m for a gradient of $.13\mu\text{m}/mm$. The pass band bandwidth is 200nm FWHM and is uniform across the LVF. Therefore, if the radiation is focused to a spot size of roughly 1.5mm or less on the LVF the wavelength selection bandwidth can be considered to be roughly 200nm. With a bandwidth of this size, most of the vibrational-rotational absorption wavelength (roughly spaced by tens of nm) will be averaged into a single absorption peak. This is not considered a fault for an NDIR detector since location of the individual rotation bands is not desired for the precision sought in this project.

5.2.4 IR Detector

The detector used is a ST60 thermopile IR detector from Dexter Research Center, Inc (MI, USA). This silicon based model was chosen for its fast response time (18ms) and the flat spectral response across the required range [71]. The active region of the detector is .61mm x .61mm, so the light needs to be focused down onto a spot within those confines. The detector has a detection range of $(10^{-6} \rightarrow .1)W/cm^2$, with a detectivity of $D* = 10^8 cm\sqrt{Hz}/W$. Since the output voltages are on the order of a few μV, a home-made amplifier with gain of 1000 was used to boost the output signal for detection with an oscilloscope. Finally, the cost of the detector is only a few tens of dollars.

5.2.5 MEMS Mirror and Control

The same STEC micro-mirror described previously in Section 3.2 was used for this system. The MEMS mirror is powered by a signal controlled by a computer program that can output a desired drive voltage pattern. A National Instruments D/A converter card turns the computer signals into an analogue control signal that is amplified by a home-made high voltage amplifier to drive the MEMS mirror. The MEMS mirror is capable of being fabricated in bulk so that the cost can be kept down to a dollar per mirror, depending on the volume of production. The HV amplifier is cheaply constructed from standard parts and has a time constant on the order of a few ms.

5.2.6 Gas Containment Box

The gas containment box was constructed from standard plexiglass and fitted with electrical through-connects (BNC and banana plug connectors) to allow control and data readout from the inclosed instrumentation. The design values for the box is shown in Figure 5.5. The large chamber holds a background of N_2 with most of the instrumentation (the MEMS, two parabolic mirrors, the LVF, and the detector). The small chamber holds the test gas, the IR source, and a right-angle parabolic mirror. The two sections are separated by a window that is IR transparent up to 10μm.

The gas containment box is not required for the system to operate but was constructed to allow controlled testing of the systems performance with various gases and concentrations. The choice of splitting the box into two chambers was necessitated by the difficulty and cost of acquiring large quantities of precisely calibrated gas concentrations. Therefore, a small (9L in volume) chamber was

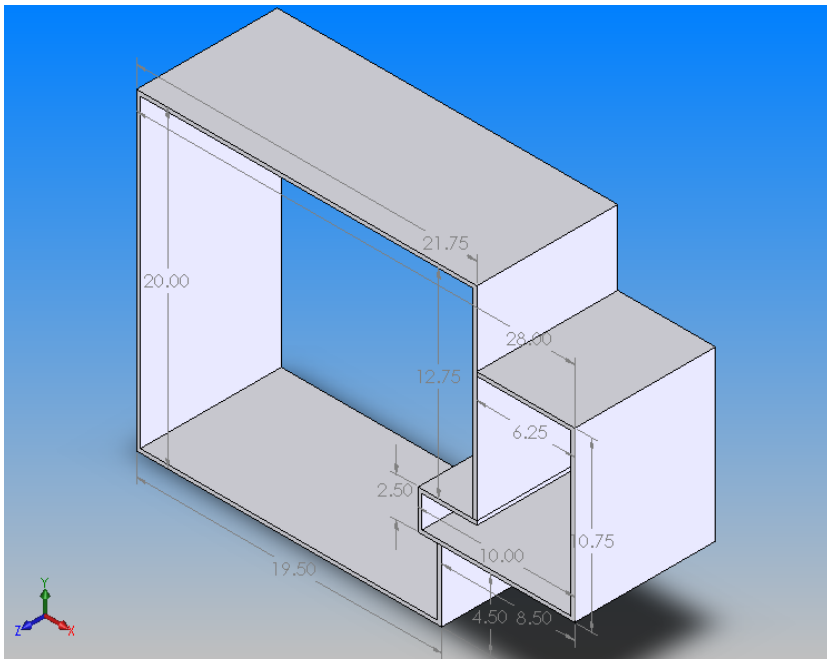

Figure 5.5: Design of the dual chamber gas containment box. The large chamber holds a background of N_2 with most of the instrumentation. The small chamber holds the test gas and the IR source and a right-angle parabolic mirror.

utilized to keep the amount of sample gas necessary controlled. The design kept the test volume small, while maintaining as long a path-length in the test gas as possible to ensure sufficient optical density (concentration multiplied by path-length) for the concentrations of interest. The large chamber could be flooded with the more inexpensive and readily available hi purity N_2. The containment box does have the added feature of blocking most IR above 10μm by the plexiglass. This solved the problem of the IR detector registering "hot-spots" in the laboratory such as researchers.

5.3 Results

5.3.1 Atmospheric

Initially tests were done to detect atmospheric elements without the gas containment box. Figure 5.6 shows the detection of atmospheric CO_2 at its known absorption wavelength centered at $\lambda = 4.26\mu$m. The signal increases with increased voltage because as the mirror scans to greater angles, the wavelength is decreasing and the source is supplying greater power. Also, the output spectrum of the broadband IR source (Figure 5.3) is plotted along with the absorptive data vs. the wavelength. Atmospheric CO_2 is typically in the range of a few hundred parts per million (ppm) and was measured in the lab to be 400ppm for this experiment.

Typical commercial application of gas detection need to be able to measure a wide range of concentrations [72] [73] [74]. For CO_2 in particular the interesting concentration regimes are in the few percent range.

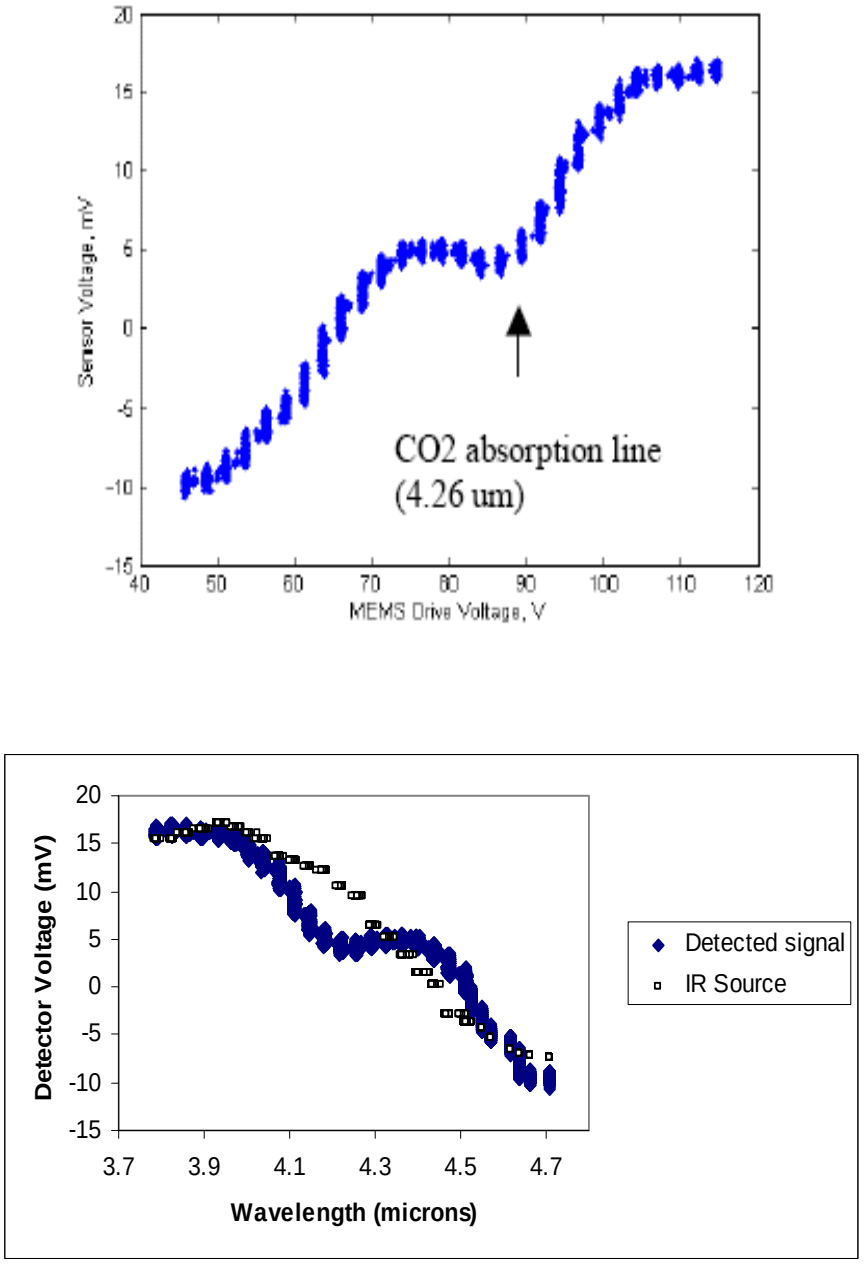

Figure 5.6: Detected spectrum of the lab atmosphere, showing a detected absorption band at the CO_2 wavelength. (top) The detected intensity in terms of detector voltage is plotted vs. the actuation voltage to the scanning mirror. For increasing actuation voltage there is decreasing radiation wavelength. (bottom) The absorption vs. wavelength is plotted along with a plot of the output power spectrum from the IR lamp (see Figure 5.3).

5.3.2 Varying concentration

The experiment was repeated with the gas containment box used to maintain control of the CO_2 concentration. Additionally, the optical alignment was adjusted to compensate for the source's output frequency dependence. This amounted to slightly defocusing the light at the detector. For a pure N_2 atmosphere the system was adjusted to achieve a roughly flat power spectrum. A region of roughly uniform power was maintained across the scan length by the MEMS mirror. It must be noted that by enclosing the system in the gas box, the path length of for the region with tested gas species decreases from roughly 30cm to 10cm.

A commercial NDIR CO_2 detector was placed in the test gas section of the gas box to monitor the precise concentration of CO_2 present. The CO_2 detector has an accuracy of 50ppm. Figure 5.7 shows the spectrum for various concentrations and Figure 5.8 shows the change in the absorption dip with gas concentration [75]. It can be seen that the system reaches saturation at roughly 1% CO_2 concentration, meaning that the all of the light at the vibrational wavelength is being absorbed.

Due to the IR beam being wider than the pass-band of the LVF, some light is leaked through in neighboring wavelengths to the detector even as all the radiation at 4.26μm is being absorbed. This is why the absorption spectra approaches a non-zero transmission power at higher concentrations.

5.4 Future Work

The system can be tested for any of the other gases with an absorbance in the range of the LVF ($2-5\mu$m). Of particular interest is methane (absorption peak at 3.4μm) and carbon monoxide (absorption peak at 4.63μm). Methane is of interest

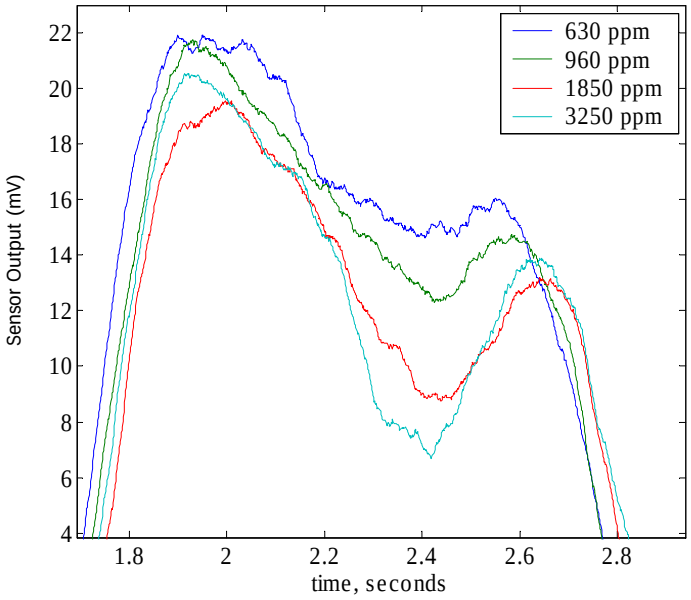

Figure 5.7: Detected spectrum of controlled concentrations of CO_2. The detected intensity in terms of detector voltage is plotted vs. the scan time from the oscilloscope. For increasing scan time there is increasing actuation voltage, which means decreasing radiation wavelength.

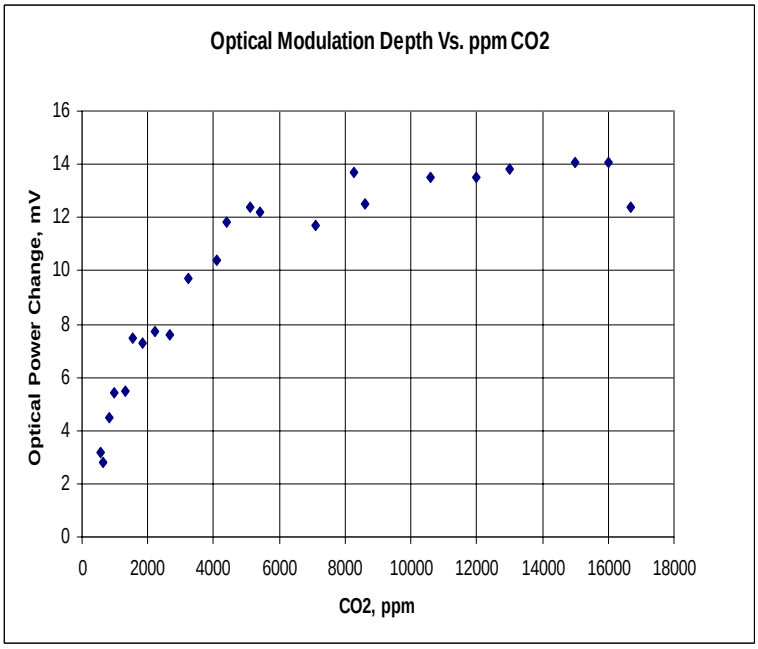

Figure 5.8: Detected spectrum of room lab, showing a detected absorption band at the CO_2 wavelength. The detected intensity in terms of detector voltage is plotted vs. the actuation voltage to the scanning mirror. For increasing actuation voltage there is decreasing radiation wavelength.

both as a greenhouse gas and as source of energy in terms of natural gas deposits. CO detection is relevant in many industrial settings and is additionally interesting because of its toxicity [76].

The system can be miniaturized significantly by updating the optics used. The parabolic mirrors focal lengths are the determining factor in the system size since the source, LVF, MEMS, and detector are all small in comparison. Of course, to maintain performance the optical path-length of the system cannot change even as its size decreases. The use of a Herriot cell or some other form of multiple pass reflection system maintain a long path-length can be used along with improved parabolic optics to miniaturize the system overall to a hand held size, without additional complexity. Herriot cells can offer dozens of optical passes, meaning the total system size could be shrunk by an order of magnitude in both lateral directions. The only trade off is total expense. The current system is an order of magnitude less in cost than commercial multi-wavelength NDIR systems, so this proposal is reasonable.

Additionally, a theoretical simulation of the various optical components in the system should be performed to compare the results measured with predictions based on empirical data from previous gas experimentation. Proper pass-band models for the LVF, the IR window, and the parabolic mirrors need to be developed and studied. The HiTran (High Resolution Transmission) molecular absorption database is the starting point for these models.

CHAPTER 6

SUMMARY

Two systems were developed to utilize optical MEMS components in larger systems. One was an optical add/drop multiplexer for telecommunication based on integration of a MEMS optical switch and an AWG. The second device was an environmental gas sensor utilizing a MEMS scanner with other optics to sweep a range of infrared radiation in search of molecular absorption patterns.

The optical add/drop multiplexer showed promise that it will be useful in next generation optical telecommunications networks as the capacity continues to increase and the optical domain of telecom continues to extend. Three different MEMS switching configurations were tested with varying degrees of success in the system. The most promising was an array of binary actuator. The array switch configuration is promising because because of its potential to integrate into a single package system with the AWG. The switching speeds are on the order of a mili-second and the MEMS system should only allow at most a few dB insertion loss to the current AWG performance, while maintaining the crosstalk performance.

The system is superior grating-based OADM systems because of potential for batch fabrication and integration. Additionally, the elegant single OADM design provides full reconfigurability with minimized complexity. By using reflective MEMS as the dynamic switching element in the OADM, the system is low power, small, integrable, and inexpensive through batch fabrication.

The non-dispersive infra-red gas detector system is capable of monitoring concentrations for IR-active gases with characteristic absorption in the $2.0 - 5.0\mu$m range. As a non-dispersive gas sensing system, the device can operate without interacting with the environment other than optically. Testing at various concen-

trations from a few hundred parts per million up to a few percent was performed with CO_2 as the test gas. Additional gases in the proscribed range of interest include CO, S_2O, CH_4, and others. The testing range is primarily set by the Linear Variable Filter and the radiation source. The other optical components of the system, including the detector, are capable of performing at wavelengths up to and beyond 10 μm.

The system is limited to its current size by only the focusing optics utilized, the parabolic mirrors. Inclusion of more precision optical elements would allow for the miniaturization of the system to hand held size without a decrease in performance.

APPENDIX A

SCREAM AT CNF

SCREAM Process at the Cornell Nanofabrication Facility

1. *Mask Oxide Deposition*

Single crystal Silicon wafers are cleaned and an oxide film is grown with the IPE PECVD 1000 Deposition System. To produce a thickness of approximately 1μm, the system is operated at a pressure of 450mT with 42sccm of N_2O and 12sccm of SiH_4 at 300^{o}C for 28 minutes.

2. *Photolithography*

Spin photoresist Shipley OCG-12i at 3000rpm for 40seconds to produce at 1.3μm thick resist coating. Prebake the resist for 90seconds at 90^{o}C. Exposure on 10X, i-line stepper, for 1.6 seconds at focus setting of 250. Postbake for 90seconds at 110^{o}C. Develop with CD-26, no agitation for 60 seconds.

It should be noted that the above recipe values worked consistently, but photolithography is very sensitive to changes in humidity and temperature and adjustments may need to be made.

3. *Pattern Transfer*

The photolithographic pattern is etched into the oxide layer on the top of the wafer by Deep Reactive Ion Etch with the Applied Materials Reactive Ion Etcher. First an oxygen plasma chamber clean is performed with 30sccm of O_2 at 90W for 20 minutes. Then the oxide etch is performed with 30sccm of CHF_3 at 110W for roughly 45 minutes. Etch selectivity is 2:1 (oxide:resist etch rate). The etch is performed for 12-15 minutes at a time and then is stopped for about 5 minutes to let the wafer cool. Continuously etching the wafer leads to resist burning.

4. *Deep Silicon Etch*

The pattern is etched deep into the silicon substrate with a PT 770 BOSCH etcher. The BOSCH process involves cycling between a polymer deposition and an etch step. The etch step utilizes SF_6 as the silicon etchant.

5. *Resist Strip*:

Oxygen plasma strip for 23minutes in the Branson Barrel Asher. Time is not critical, but all resist should be removed.

6. *Sidewall PECVD Oxide*:

The same process used for the deposition of the mask oxide, but a shorter time of 12 minutes to provide a few hundred nanometers of conformal oxide film.

7. *Floor Oxide Removal*:

With the Applied Materials Reactive Ion Etcher, the same cleaning step is performed, but an oxide etch step with 20sccm of CHF_3 at 110W for approximately 22minutes. The etch rates are lower than in step 3 due to lower gas flow rates.

8. *Extension Etch*

The PT 770 BOSCH etcher is used again as in step 4, but with higher power during the silicon etch (upto 900W, compared to 850W) to reduce loading effects.

9. *Release Etch*

The PT 770 etcher is used with a continuous SF_6 flow to obtain an isotropic silicon etch. Ar flow is increased to about 60 sccm to stabilize the plasma. The time required for release is very dependent on device layout. Typically devices such as those presented require 10minutes. The sidewall protecting polymer is not deposited in this step.

10. *"Paranoid Oxide" deposition*

The IPE PECVD 1000 Deposition System is used again with the same recipe as mentioned in Step 1. Only a few minute minutes of deposition time is required

(3-4minutes). The "paranoid oxide" is to repair any faceting of the oxide at beam edges that might have occured during the silicon etches. If their is unrepaired oxide faceting, shorting between the metal top layer and the silicon substrate can occur, rendering the device useless.

11. *Metallization*

A CVC 601 Sputter Deposition System is used to sputter a thin (200nm) film of Aluminum over the wafer. A presputter at 5A target current, 40 sccm Ar, Base pressure $< 5 \times 10^{-7}$ Torr is performed for 15 minutes. This is followed by the actual sputter at 5A current, 9mT, 40 sccm Ar, with a ramp time of 1 minute and a sputter time of 15-20 minutes.

APPENDIX B

STEC AT BERKELEY MICROLAB

STEC process flow at the Microlab at the University of California at Berkeley

1. *Thermal Oxidation*

Beginning with clean single crystal silicon wafers, a west thermal oxidation is performed in an atmospheric oxidation tube. The two types of wafers, handle and device, are have different oxide thicknesses. The handle wafer is oxidized for 25 minutes at 1000^{o}C for a thickness of .2μm. And the device wafer is oxidized for 1 hour and 5 minutes for a thickness of 1.1μm.

2. *Buried Feature Definition*

The buried features, ie the pattern on the handle wafer, is defined photolithographically using a 10x i-line GCA wafer stepper. The buried pattern is then transferred into the oxide layer by Reactive Ion Etching (RIE) in a Lam silicon dioxide etcher. The etch time is 30 seconds. The pattern oxide layer is used as a hard mask to etch the pattern into the substrate silicon by Deep RIE using the STS silicon etcher. An etch of 45 minutes is performed for a target depth of 100μm.

3. *SOI Wafer Formation*

The both the handle and device wafers are RCA cleaned with emphasis on removing all the deposited polymer from the STS DRIE on the handle wafer. The handle and device wafers are bonded by hand with visual alignment and pressing the polished surfaces together. Next the wafers are RCA cleaned again and annealed at 1100^{o}C for 1 hour in an atmospheric oxidation tube to ensure bond integrity. The bond integrity can be inspected with IR light.

The device wafer is ground and polished until the top silicon thickness is 50μm.

Now the bonded SOI wafer is oxidized again at 1100^{o}C for 25 minutes to produce a 1μm thick film.

4. *Open Alignment Dice*

Photolithography with a blank mask is performed as described in Step 2, but only two alignment dice [77] are exposed. This is to open a "window" through the device layer to the buried layer so that the two layers can be aligned properly. It causes the loss of two die per wafer. The alignment "window" pattern is etched through the upper oxide film with the Lam silicon dioxide etcher (approximately 3 minutes) and then through upper silicon layer, with the buried oxide layer as an etch stop, with the STS silicon etcher (approximately 20 minutes). Finally, the photoresist is stripped from the wafer.

5. *Frontside Feature Definition*

The frontside pattern is aligned to the buried pattern using the alignment windows and photolithographically defined as described in Step 2. The pattern is transferred through the silicon dioxide film with the Lam RIE oxide etcher, which requires 3 minutes of etching. The photoresist is stripped and the wafer is rinsed and dried.

6. *Hole Feature Definition*

On the backside of the wafer, photolithographically define the hole pattern as described in Step 2. Critical feature alignment is not necessary because of the size of the hole feature. Etch through the backside oxide film with the Lam RIE etcher (3 minutes). The wafer is then bonded to a dummy wafer using thick layers of photoresist as an adhesive. The two wafers stuck together by photoresist are hard baked for 30 minutes at 120^{o}C in vacuum to secure the bond and take care of any outgassing of the photoresist.

The backside of the wafer is undergoes DRIE of silicon in the STS for 3 hours

15 minutes to etch through the handle wafer to the buried oxide layer, which acts an etch stop.

The photoresist is stripped to separate the process wafer from the dummy wafer, then both wafers are rinsed and dried.

7. *Frontside Etch*

The process wafer is bonded by photoresist to the dummy wafer again as described in Step 6, but this time the backside of the process wafer is secured to the dummy wafer. DRIE of silicon in the STS is performed for 18 minutes to transfer the frontside pattern through the top layer of silicon.

8. *Post Processing*

While still stuck to the dummy wafer, the process wafer is diced using a Disco dicing saw. The dummy wafer should not be diced. The photoresist is stripped to separate the device dice from the dummy wafer.

The device dice are RCA cleaned and allowed to air dry. The structures are released with a timed HF etch (2-3 minutes). The dice are then rinsed in de-ionized water followed by isopropyl alcohol and allowed to air dry.

Finally, 500 Å of gold is evaporated onto the mirror surface to improve reflectivity.

APPENDIX C

SCREAM AT BERKELEY MICROLAB

SCREAM Process Modified for the Microlab at the University of California at Berkeley

1. *Mask Oxide Growth*

Single crystal silicon wafers are cleaned and oxidized in an atmospheric oxidation tube. The oxidation is a wet oxidation process and is run for 4hours 30minutes at 1000C. A 1μm thick silicon dioxide layer is grown over the entire wafer.

2. *Photolithography*

The oxidized wafer is primed for photoresist coating by introduction of vapor phase Hexamethyldisilazane (HMDS) in a heated (100C) constant pressure (1000Torr) environment for 35 minutes. HMDS allows improved photoresist adhesion to the oxide layer.

Shipley's OCG OiR 897-10i (I-line resist) is spun on to the wafer using an SVG automated photoresist coating track. The resist is dispensed while the wafer is spun at 1300RPM to provide a resist thickness of 2μm. After coating the resist is soft baked at 90C for 120seconds.

The resist is exposed on a 10x i-line GCA 6800 wafer stepper with an exposure time of 1.40seconds and a focus of 250.

Exposed wafers are developed on an automated SVG developer track using OPD 4262 developer for 60seconds with no agitation or post-bake.

It should be noted that the above recipe values worked consistently, but photolithography is very sensitive to changes in humidity and temperature and adjustments may need to be made.

3. *Pattern Transfer to Oxide*

The lithographic pattern in the photoresist is etched into the oxide layer on the top of the wafer by Deep Reactive Ion Etch in a Lam SiO_2 etcher. The selectivity of the etch for SiO_2 to photoresist is roughly 2:1 and the underlying silicon layer can be used an etch stop. The total etch time is 2minutes and is performed in 15second increments with the wafers rotated 90^o between each etch step. The incremental etching serves the dual purpose of decreasing across wafer non-uniformity and prevents the photoresist from burning during a long etch.

4. *Photoresist Strip*

Next the remaining resist is stripped from the wafer with a O_2 plasma etch in a Technics Plasma Etcher. O_2 flow is maintained at 51.1 sccm, with a pressure of 270mTorr and a plasma RF power of 300W for a total of 7minutes, which ensures that all resist is removed.

5. *Deep Silicon Etch*

The pattern is etched deep into the silicon of the wafer with a Surface Technology System (STS) Advanced Silicon Etch system. This system can perform a anisotropic (vertical) etch using the oxide film as a hard mask. The selectivity of Si etching to SiO_2 etching is roughly 100:1. Microlab maintained etch recipe HEXA100 was used for 20minutes to consistently achieve an etch depth of 35μm. There is still oxide remaining on the top of the defined structures after this etch.

6. *Sidewall Oxide Deposition*

To provide a conformal oxide film deposition a low temperature oxide (LTO) was grown in a Tystar chemical vapor deposition tube. The Microlab's standard undoped LTO process was run for 20 minutes at 450C to produce a 250nm thick conformal oxide film. At the Cornell Nanofabrication Facility, the conformal oxide was deposited by use of a plasma enhanced CVD system instead.

7. *Floor Oxide Removal*

The Lam SiO_2 is operated in short 10second bursts with high power to produce as vertical an etch as possible to remove the oxide on floor of the wafer, ie in the bottom of the trenches. While the high power vertical etch serves to protect the sidewall oxide from being etched, the left over oxide on the top of the structures is etched by this process. In particular, the oxide on top of the structures will be etched faster than the oxide in the bottom of the trenches, which is why the left-over oxide is essential and care must be taken that the oxide etch does not punch through the upper oxide layer.

8. *Extension Etch*

The STS DRIE recipe HEXA100 is used again for 2 minutes to create a $5 - 8\mu$m extension etch into the exposed substrate silicon.

9. *Release Etch*

An isotropic RIE etch is performed in the STS by use of the recipe JFRKISO developed by Jeremy Frank at the Microlab. The recipe etches Si selectively vs. SiO_2 at 100:1 and is nearly isotropic. A 5minute release etch is sufficient to release the 2μm this structures.

9a. *Optional "Paranoid Oxide" Deposition*

In order to avoid any shorting that between the metal to be deposited in the final step the process and the underlying Si, additional oxide is traditionally deposited to ensure any small fissures in the oxide will be closed. While this step was pretty essential in processing at CNF, it never was necessary in processing at the Berkeley Microlab. If desired a 5minute CVD of LTO as described above can be performed.

10. *Metallization*

Finally the system is metallized for electrical and reflective performance. The

metallization was performed with a CPA 9900 DC magnetron sputtering system. Two thousand Å of Aluminum was deposited with a target power of 4.5 kW at a system pressure of 6 mTorr.

BIBLIOGRAPHY

[1] Richard P. Feynman. There's plenty of room at the bottom. *California Institute of Technology Engineering and Science*, 1960. Available at http://www.zyvex.com/nanotech/feynman.html.

[2] Kurt E. Petersen. Silicon as a mechanical material. *Proceedings of IEEE*, 70:420–457, 1982.

[3] Gregory T.A. Kovacs. *Micromachined Transducers Sourcebook*. McGraw-Hill, Boston, 1st edition, 1998.

[4] Stephen D. Senturia. *Microsystem Design*. Kluwer Academic Publishers, Norwell, MA, 1st edition, 2001.

[5] Marc Madou. *Fundamentals of Microfabrication*. CRC Press, New York, 1st edition, 1997.

[6] Eva Oberdorster. Manufactured nanomaterials (fullerenes, c_{60}) induce oxidative stress in the brain of juvenile largemouth bass. *Environmental Health Perspectives*, 112(10), July 2004.

[7] Michael Crichton. *Prey*. HarperCollins, 2002.

[8] K. Nandakumar A.H. Heuer R.L. Mullen R. Ballarini M.A. Huff H. Kahn, S. Stemmer. Mechanical properties of thick, surface micromachined polysilicon films. *IEEE Proceedings International Workshop on MicroElectroMechanical Systems (MEMS '96)*, pages 343–348, 1996.

[9] S.J. Walker and D.J. Nagel. Optics and mems. *Technical Report NRL/MR/6336-99-7975, Naval Research Laboratory*, 1999. Available at http://mstd.nrl.navy.mil/6330/6336/moems.html.

[10] Govind P. Agrawal. *Fiber-Optic Communication Systems*. Wiley-Interscience, New York, 3rd edition, 2002.

[11] K.G. Coffman and A.M. Odlyzko. Internet growth: Is there a moore's law for data traffic? Available at http://www.research.azt.com/ amo.

[12] John Strand. *Optical Network Architecture Evolution*, chapter 3, Optical Fiber Telecommunications IVB. Academic Press, San Francisco, CA, USA, 2002.

[13] Vinod Khosla. Terabit tsunami. *Proceedings of the Optical Fiber Communications Conference (OFC 2000)*, March 2000.

[14] Hiromichi Shinohara. Ntt's deployment of ftth services. *Proceedings of the Optical Fiber Communications Conference (OFC 2004)*, March 2004.

[15] Martin Zirngibl. *Applications for Optical Switch Fabrics*, chapter 26, Optical Fiber Telecommunications IVA. Academic Press, San Francisco, CA, USA, 2002.

[16] Ivan P. Kaminow. *Photonic Local Networks*, chapter 26, Optical Fiber Telecommunications II. Academic Press, San Francisco, CA, USA, 1991.

[17] K. Habara K. Sasayama, Y. Yamada and K.-I. Yukimatsu. Frontier-net: Frequency-routing-type time-division interconnection network. *IEEE Journal of Lightwave Technology*, 15(3):417–429, March 1997.

[18] T. Kudou K. Harada and T. Ozeki. Hierarchical opticalpath cross-connect systems for large wdm networks. *Proceedings of Optical Fiber Communications Conference (OFC 1999)*, pages WM–16, 1999.

[19] S.J.B. Yoo S. Yao, B. Mukherjee and S. Dixit. A unified study of contention-resolution schemes in optical packet-switched networks. *IEEE Journal of Lightwave Technology*, March 2003.

[20] M. Vigoureux L. Noirie and E. Dotaro. Impact of intermediate traffic grouping on the dimensioning of multi-granularity optical networks. *Optical Fiber Communication Conference (OFC 2001)*, 54, TuG3, 2001.

[21] W.J. Tomlinson. Wavelength-selective switching - architecture and technology overview. *Proceedings of the Optical Fiber Communications Conference (OFC 2004)*, 2004.

[22] Christopher R. Doerr. *Planar Lightwave Devices for WDM*, chapter 9, Optical Fiber Telecommunications IVA. Academic Press, San Francisco, CA, USA, 2002.

[23] D. Hah J. C. Tsai, S. Huang and M. C. Wu. $1xn^2 wavelength - selective switch with telescope - magnified 2d input/output fiber collimator array, journal = .$

[24] M. Oguma T. Shibata H. Takahashi K. Suzuki, T. Mizuno and A. Himeno. Fully-reconfigurable wavelength-selective optical 1xn switch based on transversal filter configuration. *Proceedings of the Optical Fiber Communications Conference (OFC 2004)*, 2004.

[25] Martin Ronald Amersfoort. *Phased-array Wavelength Demultiplexers and Their Integration with Photodetectors*. Delft University Press, 1994.

[26] C. Dragone. Efficient n x n star coupler based on fourier optics. *Electronics Letters*, 24, 1988.

[27] C. Dragone. Efficient n x n star couplers using fourier optics. *Journal of Lightwave Technology*, 7, 1989.

[28] I.P. Kaminow C. Dragone, C.H. Henry and R.C. Kistler. Efficient multichannel integrated optics star coupler on silicon. *IEEE Photonics Technology Letters*, 1.

[29] S. Suzuki A. Sugita K. Okamoto, H. Takahashi and Y. Ohmori. Design and fabrication of integrated-optic 8x8 star coupler. *Electronics Letters*, 27.

[30] Katsunari Okamoto. *Fundamentals of Optical Waveguides*. Academic Press, San Diego, 1st edition, 2000.

[31] http://www.c2v.nl/software/.

[32] R. Marz. *Integrated Optics: Design and Modelling*. Artech House, Norwood, MA, USA, 1995.

[33] O. Ishida A. Himeno K. Okamoto, H. Hasegawa and Y. Ohmori. 32 x 32 arrayed-waveguide grating multiplexer with uniform loss and cyclic frequency characteristics. *Electronics Letters*, 33.

[34] I. P. Kaminow B. Glance and R. W. Wilson. Applications of integrated waveguide grating router. *Journal of Lightwave Technology*, 12, June 1994.

[35] R. März H. Michel A. Reichelt H.W. Schneider P.C. Clemens, G. Heise. Wavelength-adaptable optical phased array in sio_2–si. *IEEE Photonics Technology Letters*, 7(9):1040–1041, 1995.

[36] J. Capmany P. Muñoz, D. Pastor. Wavelength-adaptable optical phased array in sio_2–si. *Journal of Lightwave Technology*, 20(4):661–674, 2002.

[37] G.M. Morris S.M. Norton, T. Erdogan. Coupled-mode theory of resonant-grating filters. *Journal of the Optical Society of America: A*, 14(3):629–639, 1997.

[38] M.K. Smit and C. van Dam. Phasar-based wdm-devices: Principles, design, and applications. 2(2):236–249, 1996.

[39] M. Shiozaki T. Komiya K. Saitoh M. Nishimura T. Kanie, M. Katayama. A highly dense mems optical switch array integrated with planar lightwave circuit. *IEEE Proceedings International Workshop on MicroElectroMechanical Systems (MEMS 2002)*, pages 560–563, 2002.

[40] Y.-H. Cho S.-S. Lee K.-C. Song J.-U. Hu Y.-H. Jin, K.-S. Seo. An soi optical microswitch integrated with silicon waveguides and touch-down micromirror actuators. *IEEE/LEOS Proceedings International Conference on Optical MEMS (MOEMS 2000)*, pages 43–44, 2000.

[41] S. Yao and B. Mukherjee. Design of hybrid waveband-switched networks with oeo traffic grooming. *Proceedings of the Optical Fiber Communications Conference (OFC 2003)*, pages 11–12.

[42] Daniel T. McCormick and Norman C. Tien. A mems based optical fiber scanning probe. *Proceedings of IEEE/LEOS Optical MEMS*, pages 207–208, August 2002.

[43] Daniel Thomas McCormick. *Dielectric Fluid Enhancement of Radio Frequency MEMS Devices and Micromachined Scanners for Optical Coherence Tomography Imaging*. PhD thesis, Cornell University, August 2003.

[44] K. Shaw, Z. Zhang, and N. MacDonald. Scream i: A single mask, single-crystal silicon process for microelectromechanical structures. *Proceedings of IEEE Micro Electro Mechanical Systems (MEMS 1993)*, pages 155–169.

[45] Kurt E. Petersen. Silicon torsional scanning mirrors. *IBM Journal of Research and Development*, 24(5):631–637, 1980.

[46] D.T. McCormick and N.C. Tien. Multiple layer asymmetric vertical combdrive actuated trussed scanning mirrors. *Proceedings of IEEE/LEOS Optical MEMS*, August 2003.

[47] R. Carr Y.-A. Peter and O. Solgaard. Segmented deformable micro-mirror for free-space optical communication. *Proceedings of IEEE/LEOS Optical MEMS*, August 2002.

[48] T. Cheng V. Milanovic, G.A. Matus and B. Cagdaser. Monolithic high aspect ratio two-axis optical scanners in soi. *Proceedings of IEEE Sixteenth Annual Conference on Micro Electro Mechanical Systems*, 2003.

[49] U. Krishnamoorthy and O. Solgaard. Self-aligned vertical comb-drive actuators for optical scanning micromirrors. *Proceedings of IEEE/LEOS Optical MEMS*, August 2001.

[50] K.-Y. Lau R.A. Conant, J.T. Nee and R.S. Muller. A fast flat scanning micromirror. *IEEE Solid State Sensor and Actuator Workshop Technical Digest*, pages 6–9, 2000.

[51] Jui-Che Tsai Chao-Hsi Chi, Jin Yao and Ming C. Wu. Compact 1x8 mems optical switches using planar lightwave circuits. *Proceedings of the Optical Fiber Communications Conference (OFC 2004)*, 2004.

[52] Madanagopal Vinjimur Kunnavakkam. *MEM Systems Development for Positioning, Control, and Optical Applications*. PhD thesis, Cornell University, January 2001.

[53] M.-A. Grétillat N.F. de Rooij-R. Bättig O. Anthanmatten B. Walk-P. Vogel C. Marxer, C. Thio. Vertical mirrors fabricated by deep reactive ion etching for fiber-optic switching applications. *Journal of MicroElectroMechanical Systems*, 6(3):277–285, 1997.

[54] A.W. Groenveveld Rob Legtenberg and M. Elwenspoek. Comb-drive actuators for large displacements. *Journal of Micromechanical Microengineering*, 6:320–329, 1996.

[55] N.C. MacDonald. Scream micromechanical systems. *Microelectronic Engineering*, 32:49–73, 1996.

[56] M.T.A. Saif and N.C. MacDonald. Design considerations for mems. *Proceedings of North American Conference on Smart Structures and Materials*, 1995.

[57] Herman A. Szymanski. *IR, Theory and Practice of Infrared Spectroscopy*. Plenum Press, New York, 1st edition, 1964.

[58] John S. Townsend. *A Modern Approach to Quantum Mechanics*. McGraw-Hill, New York, 1st edition, 1992.

[59] David J. Griffiths. *Introduction to Quantum Mechanics*. Prentice-Hall, Englewood Cliffs, New Jersey, 1st edition, 1995.

[60] Richard M. Badger. Determination of bond force constants. *Journal of Chemical Physics*, 2(128), 1934.

[61] W. Gordy. A relation between bond force constants, bond orders, bond lengths, and the electronegativities of the bonded atoms. *Journal of Chemical Physics*, 14(304), 1946.

[62] Paul A. Tipler. *Modern Physics*. Worth Publishers, New York, 11th edition, 1996.

[63] *CRC Handbook of Chemistry and Physics*. Boca Raton, Florida, 66th edition, 1986.

[64] Daniel I. Sebacher. *Nondispersive Infrared Absorption Monitors for Trace Gases*, chapter 6, Infrared Methods for Gaseous Measurements: Theory and Practice. Marcel Dekker, Inc., New York, NY, USA, 1985.

[65] P. Bramley J.G. Crowder C.H. Wang S.D. Smith, A. Vass. Comparison of ir led gas sensors with thermal source products. *IEEE Proceedings in Optoelectronics*, 144(5):266–270, 1997.

[66] Sandra Schweizer Gerhard Lammel and Philippe Renaud. *Optical Microscanners and Microspectrometers using Thermal Bimorph Actuators*. Kluwer Academic Publishers, Norwell, MA, 1st edition, 2002.

[67] Santiago Marco Mauricio Moreno J. Samitier-Luis Fonseca I. Gracia C. Cane Carlos Calaza, E. Meca. Assessment of the final metrological characteristics of a moems-based ndir spectrometer through system modeling and data processing. *IEEE Sensors Journal*, 3(5), 2003.

[68] Michael J. Sepaniak Panos G. Datskos Thomas A. Betts, Christopher A. Tipple. Selectivity of chemical sensors based on micro-cantilevers coated with thin polymer films. *Analytica Chimica Acta*, 422:89–99, 2000.

[69] http://www.gilway.com/shortcat/ir_reflector.html.

[70] http://www.edmundoptics.com/onlinecatalog/displayproduct.cfm?productid=2307.

[71] http://www.dexterresearch.com/.

[72] C.T. Elliott J.G. Crowder, H.R. Hardaway. Mid-infrared gas detection using optically immersed, room-temperature, semiconductor devices. *Measurement Science and Technology*, 13:882–884, 2002.

[73] Andreas Dubbe. Fundamentals of solid state ionic micro gas sensors. *Sensors and Actuators B*, 88:138–148, 2003.

[74] V. Mannheim T. Ashley D.T. Dutton A.D. Johnson G.J. Pryce S.D. Smith C.H. Wang, J.G. Crowder. Detection of nitrogen dioxide using a room temperature operation mid-infrared insb light emitting diode. *Electronics Letters*, 34(3):300–301, 1998.

[75] M. Huiku K. Weckström P. Meriläinen G. Stemme E. Kalvesten, T. Corman. A silicon ir-source and co_2-chamber for co_2 measurements. *IEEE Proceedings International Workshop on MicroElectroMechanical Systems (MEMS '98)*, pages 69–74, 1998.

[76] S.L. Swartz R.R. Rao Prabir K. Dutta Christopher T. Holt, A.M. Azad. Carbon monoxide sensor for pem fuel cell systems. *Sensors and Actuators B*, 87:414–420, 2002.

[77] Robert Alan Conant. *Micromachined Mirrors*. PhD thesis, University of California, Berkeley, May 2002.